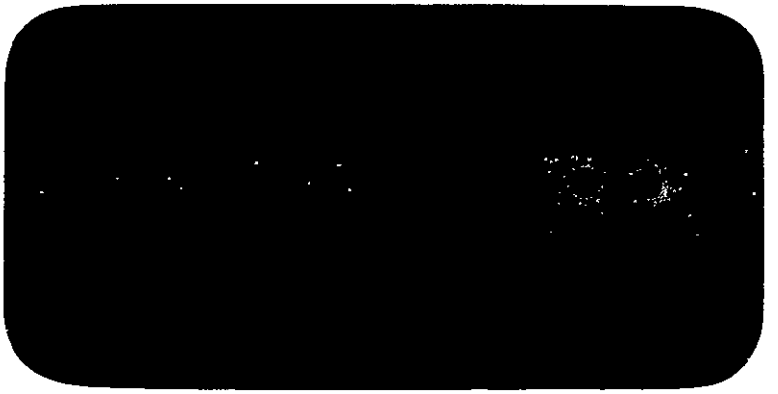

(NASA-CR-155056) GEOLOGY ORBITER COMPARISON STUDY (Science Applications, Inc., Pasadena, Calif.) 137 p HC A07/MF A01 CSCL 03B

N77-34073

Unclas
G3/91 15084

science applications inc.

Science Applications, Inc.
Schaumburg, Illinois

Geology Orbiter Comparison Study

by

James A. J. Cutts
Karl R. Blasius
Donald R. Davis
Kevin D. Pang
David C. Shreve

STAR Abstract

The purpose of this study was to examine the instrument requirements of planetary geology orbiters with the objective of determining the feasibility of applying standard instrument designs to a host of terrestrial targets. Within the basic discipline area of geochemistry, gamma-ray, x-ray fluorescence, and atomic spectroscopy remote sensing techniques are considered. Within the discipline area of geophysics, the complementary techniques of gravimetry and radar are considered. Experiments using these techniques are analyzed for comparison at the Moon, Mercury, Mars and the Galilean satellites. On the basis of these comparative assessments, the adaptability of each sensing technique is judged (1) as a basic technique for many targets, (2) as a single instrument applied to many targets, (3) as a single instrument used in different mission modes, and (4) as an instrument capability for nongeoscience objectives.

Report No. SAI 1-120-399-S1

GEOLOGY ORBITER COMPARISON STUDY

by

James A. J. Cutts
Karl R. Blasius
Donald R. Davis
Kevin D. Pang
David C. Shreve

Science Applications, Inc.
283 S. Lake Avenue, Suite 218
Pasadena, California 91101

for

Planetary Programs Division
Office of Space Science
NASA Headquarters
Washington, D. C.

Contract No. NASW-2613

August 1977

FOREWORD

This study was performed between September 1975 and February 1976 as part of the task schedule completed by Science Applications, Inc. for the Planetary Programs Division of OSS/NASA under Contract No. NASW-2613. The results are intended to assist NASA in advanced planning of remote sensing missions to terrestrial type bodies for which the objectives are largely geological, geochemical, or geophysical in nature. The specific objectives of this report are to examine experiment concepts for geoscientific exploration of various terrestrial bodies and the Galilean satellites and to assess the applicability of the lunar polar orbiter payload to exploration of these bodies in the context of the analysis. The effects of atmospheres, space environments, and orbital parameters are of great importance in the study.

The authors express their appreciation to G. A. Briggs, L. D. Friedman, and A. Metzger of Jet Propulsion Laboratory, J. Trombka of Goddard Space Flight Center, and J. C. Niehoff, T. W. Thompson, and T. W. Armstrong of Science Applications, Inc. for technical inputs and a number of stimulating conversations and suggestions.

TABLE OF CONTENTS

TABLE OF CONTENTS (con't.)

SUMMARY

In the cost-conscious mid 1970's, the concept of a single basic spacecraft design equipped with a standard instrument payload for the study of the surfaces and interiors of all the bodies in the solar system has a definite appeal. Many spacecraft systems such as those for communications exhibit commonality and can be used in a variety of missions with little adaptation. But is the same true of scientific instrument packages? Is it possible to define a set of instruments with wide application in geological exploration for the detailed study of the planets? (Could the Lunar Polar Orbiter payload, for example, be adapted with very little modification for remote sensing missions to the terrestrial planets and Jovian satellites?) If such an adaptation is possible, how do these instruments perform under these varying circumstances? How does the spacecraft design and space environment affect performance? Can new instrument designs and mission concepts be identified that minimize the negative aspects and exploit the opportunities presented by missions outside the earth-moon system? These are the primary questions we attempt to answer in this geology orbiter comparison study.

Two basic discipline areas in the general field of the crustal and interior properties of solar system bodies have been considered (Table S.1). In geochemistry, the discipline area is surface elemental composition and three remote sensing techniques have been evaluated. They are gamma-ray, x-ray fluorescence and atomic spectroscopy. In geophysics, the discipline area is gravity field and altimetry. Two techniques: range-doppler tracking and gravity gradiometry have been evaluated for the gravity field determination; radar has been evaluated for altimetry.

Among the elemental analysis experiments, gamma-ray spectroscopy (Table S.2) is the most powerful of the three techniques. It is the only one of the three remote sensing techniques considered here that will work at Mars. Very similar instrument designs based on a high resolution passively-cooled intrinsic germanium detector can be used at the Moon,

Table S.1

EXPERIMENTAL TECHNIQUES AND INSTRUMENTS FOR COMPARATIVE ANALYSIS

Prime Discipline Area	Technique	Immediate Experimental Objective	Planetological Implications
Geochemistry (surface elemental abundances)	Gamma Ray Spectroscopy	Identification and quantitative measurement of elements in terrestrial body surface materials	Provides new constraints on the distribution of elements in primordial bodies, their thermal histories, and the redistribution of materials by surface processes. Supplies new insights into the interaction of terrestrial body surfaces with radiation fields.
	X-Ray Fluorescence Spectroscopy	Identification and quantitative measurement of elements in planetary surface materials	
	Atomic Spectroscopy	Identification and quantitative measurement of elements (atomic species) emitted from the surfaces of terrestrial bodies into the space environment	
Geophysics (gravity fields and altimetry)	Radar	Determination of the figures of terrestrial bodies, center of mass location, topographic maps and scattering properties	Provides new constraints on the composition and internal mass distribution of terrestrial bodies and their isostatic states.
	Range/Doppler, Tracking	Measurement of mass and gravitational field harmonics	
	Gravimeter	Measurement of mass and gravitational field harmonics	

Table S.2

GAMMA-RAY SPECTROSCOPY

General Summary Comments

- Observations of Mercury, Mars and Moon are feasible and a range of geochemically interesting elements can be detected on each
- No gamma-ray emission from the surfaces of Titan or Venus can be detected from orbit because of atmosphere attenuation
- Radiation effects preclude useful gamma ray experiments at the Galilean satellites except at Callisto
- Given the low gamma ray emission expected from Callisto a Jupiter orbiter with close Callisto flybys could not achieve useful elemental abundance information. However, a spacecraft orbiting Callisto could obtain useful elemental information.

Instrument Design

- Identical detector and electronics practical for Mars, Moon, Mercury
- Thermal design of instrument may be different for Mercury

Effect of Atmosphere

- Atmospheric attenuation negligible at Moon and Mercury
- Atmospheric attenuation significant at Mars but does not seriously impact viability of experiment

Orbit Design Issues

- Circular orbit provides best observing conditions
- Low altitude observations do not yield 'effective' high resolution except at the poles because of high integration times required by the experiment
- Elliptical orbit with periapse at pole may be an optimal choice for a Mercury mission

Experiment Performance (at Moon, Mars and Mercury)

- Naturally occurring radioactive elements potassium, uranium and thorium measured
- Major elements iron, titanium, silicon, oxygen, aluminum determined
- Possible detection of magnesium, calcium, sodium, manganese, sulfur and chlorine depending on abundances
- At least 10 hours and preferably 100 hours of observative time required for each spatial resolution element
- Only small differences in threshold detection levels between Mercury, Mars and Moon

Common Problems

- Build-up of radioactive materials during interplanetary phase of mission introduces background and masks some elements
- Low fluxes demand very long observation times to achieve high signal-to-noise and even moderate spatial resolution

Mars, and Mercury. Roughly comparable performance capabilities exist at these three bodies. Assays can be made of the three naturally radioactive elements potassium, uranium and throium, as well as a variety of elements in which radioactivity is induced by galactic and solar cosmic ray bombardment.

Unfortunately, because of trapped radiation, the Galilean satellites, with the possible exception of Callisto, do not appear to be accessible to study by gamma-ray spectroscopy. Gamma-ray emission of the inner Galilean satellites Io and Europa is greatly enhanced by both trapped proton and trapped electron bombardment. The trapped proton bombardment induces nuclear reactions with the emission of discrete lines carrying elemental information. However, continuum radiation background originating from both the target object and the spacecraft precludes measurement of elemental abundances at either Io, Europa or Ganymede. Foreseeable developments in sensor technology will probably not change this conclusion. Background is not an insuperable problem at Callisto but the low signal strengths expected from that satellite imply that observations of long duration from an orbit around Callisto are necessary for elemental abundance measurement.

The capabilities of x-ray fluorescence fluoroscopy differ in many ways from those of gamma-ray spectroscopy (Table S.3). Mars is not accessible to study because fluorescent x-rays are heavily absorbed by the martian atmosphere. The technique works very well at Mercury and the more intense solar fluxes at Mercury may allow the detection of calcium, titanium, and iron in addition to the low Z elements, magnesium, alumina and silicon which can be detected on the Moon. The large area gas proportional counter which is a collimated device is an appropriate instrumert for studying both planets.

Elemental analysis by fluorescence spectroscopy should also be possible at the Galilean satellites (with the exception of Callisto) where characteristic x-rays are excited by both trapped electrons and protons and a much broader range of emissions can be observed.

Table S.3

X-RAY FLUORESCENCE SPECTROSCOPY

General Summary Comments

- Observations of fluorescent x-rays induced by solar x-rays are possible at the Moon and Mercury
- No x-ray emission from Mars, Venus or Titan can be detected from orbit because of atmospheric attenuation
- Observations of fluorescent x-rays induced by high energy charged particles are possible at the Galilean satellites, except Callisto, despite intense radiation background

Instrument Design

- Non-focusing collimated proportional counter detector with xenon gas mixture is suitable for Moon and Mercury
- Focusing system together with background rejection techniques are required for observation of the Galilean satellites

Orbit Design Issues

- Circular orbit provides best observing conditions at Mercury and Moon
- Low altitude observations yield effective high resolution at both the equator and poles because of the short integration times for observations of Moon and Mercury but no data obtained on the unilluminated side of these objects
- Non-focusing spectrometer can be collimated to provide useful resolution at long ranges at Mercury
- Observatory mode observations of the Galilean satellites can yield considerable improvements in signal-to-noise over close encounter observations

Experiment Performance

- Only low Z elements (magnesium, aluminum, silicon) can be determined at the Moon
- Possibility of detection of calcium and titanium at Mercury
- Relatively short integration times needed at Moon and Mercury (seconds to minutes)
- Many major elements over an extensive range in Z can be observed at the Galilean satellites, but long observing times (minutes to hours) are needed because of the long ranges of observation

Common Problems

- Charged particle interference is a problem at the Galilean satellites and even at Mercury. Sophisticated background rejection techniques are needed to mitigate this form of interference.
- Instrument only observes the chemistry of a surficial layer. This apparently was not a serious problem at the Moon where this composition appeared representative of the soil composition. It may be more of a problem at the Galilean satellites.
- Absolute accuracy and even relative accuracy of elemental abundance determination is poor for the Galilean satellites. It may be improved by using calibration targets on the spacecraft and exposed to the unshielded radiation environment.

A glancing incidence telescope or 'light bucket' would have definite advantages for observations in the Jovian system compared to a simple collimator since it can be used to concentrate the x-ray signal and thereby improve the ratio of signal to background. A small cooled germanium detector could be substituted for a proportional counter and would provide an extended spectral range, higher quantum efficiency and improved energy resolution compared to a proportional counter. The primary difficulty with the x-ray fluoroscopy experiment involves relating the observed signals to chemical abundances. Even with simply monoenergetic x-ray sources, nonlinearities in the stimulated x-ray yields abound and with two excitation sources with poorly defined energy fluxes these problems will be compounded. Differential sputtering of surface materials may also cause the x-ray emission to be unrepresentative of the crustal compositions of the satellites.

Atomic spectroscopy of the atomic clouds created by the interaction of trapped radiation with the Jovian satellites is only applicable in the Jovian system (Table S.4). Observations of solar excited resonant emission of atomic species in the vicinity of Io (J_1), Europa (J_2), and the small inner satellite Amalthea (J_5) will be possible. As with x-ray fluorescence spectroscopy it will be difficult to relate line intensities to crustal elemental abundances because of the complex mechanism of line emission. A tunable acousto-optical filter spectrometer with a spectral resolution of approximately 1 Å would be well adapted to reconnaissance of the atomic clouds in the vicinities of the Galilean satellites and would achieve elemental sensitivities a factor of ten better than those achievable from the earth. An additional advantage is the ability to map the clouds in three dimensions and with several orders of magnitude better spatial resolution. A low resolution spectrometer or photometer such as is planned for LPO would not be suited for this uniquely Jovian experiment. However, the Mariner Jupiter Saturn Polarizing spectrophotometer with performance specifications similar to those anticipated for LPO reflectometers should be able to map the sodium clouds around Io.

Table S.4

ATOMIC SPECTROSCOPY EXPERIMENT

General Summary Comments

- Observations of a range of geochemically interesting elements derived from the surfaces of the Galilean satellites and present as atomic species in the space environment are feasible
- Atomic emission also can be used to remotely probe the particle and field environment in the Jupiter system
- Atomic emission phenomenon relevant to planetary surface compositions are not detectable at Moon, Mercury, Mars, Venus or Titan; however, a rich variety of visual and ultraviolet emission phenomena do occur and provide measures of upper atmospheric composition

Instrument Design Issues

- Several instrument concepts are applicable. The performances of the Mariner Jupiter Saturn Photo Polarimeter Spectrometer and a Tunable Acousto-Optical Filter with Gallium Arsenide photomultiplier tube are evaluated
- Adopt a fairly narrow field-of-view (10°) to permit long range observations

Orbit Design Issues

- High inclination Jupiter orbit desired to provide three-dimensional resolution of atomic cloud phenomena
- Long range observations are acceptable since an extended source is observed and desirable because they move the spacecraft well away from the radiation environment

Experiment Performance

- Sensitivity of the instrument to atomic emission is about 0.1 to 0.01 Rayleighs
- Sodium potassium and sulfur from Io have been detected from the earth and can easily be observed from Jupiter orbit
- Ability to detect other elements is model dependent but there seems to be a reasonable probability of detection calcium and iron at Io and sodium and potassium at Europa
- Quantitative estimates of surface composition and highly model dependent. Mapping of distribution of elements will improve definition of models.

An important feature of the observations of atomic emission in the Jovian system is the ability not only to record elemental information but also to derive information about particle and field interactions with the surfaces and atmospheres of Jupiter and its satellites.

The geophysical experiment (gravity field and altimetry) appears to offer the most in terms of instrument commonality of all experiments studied (Table S.5). A single instrument design can perform altimetry experiments at Moon, Mercury, Mars and the Galilean satellites. The range/doppler navigation systems can be used to determine gravity fields with an accuracy that is primarily limited by orbital design. The two experiments are scientifically synergistic; at the Galilean satellites radar altimetry data may be necessary to refine encounter altitudes sufficiently to yield mass and gravity data.

In Table S.6 the adaptability of various remote sensing experimental techniques to various targets and objectives is compared. This chart necessarily oversimplifies the complex and varied issues that arise when one considers experiment adaptability and it should only be used as a very general guide to the flexibility of different experimental concepts. Remote techniques for mineralogical analysis (reflectance and emission spectroscopy) and for geology (frame and line imaging) which were not considered in the report, have been added for comparison.

Gravity field and altimetry is the most adaptable experiment to different targets (Column 1) of those considered as it works even at Venus. High resolution atomic spectroscopy is the least adaptable for geochemical study as it only works with any certainty for the Galilean satellite Io.

The second column indicates the adaptability of a single instrument design to those objects which are accessible to observation by the technique in question. A gamma-ray instrument, for example, could be designed with minimal design variations for observations of Mars, Mercury and the Moon. On the other hand, for altimetry observations of Venus, a rather different design of radar is needed than for other target objects because of the dense Venusian atmosphere.

Table S.5

GRAVITY FIELD AND ALTIMETRY EXPERIMENT

General Summary Comments

- Detailed topographic maps of Moon, Mercury and Mars can be obtained from orbiters about those planets with a 15 GHz radar altimeter; topographic data recovered from satellite flybys of a Jupiter orbiter are comparatively sparse.
- Range/doppler tracking is a better technique than gravity gradiometry for determining gravitational field harmonics from the relatively high altitudes assumed for geology orbiter missions
- Radar altimetry and gravity experiments provide an important combined data set

Instrument Design

- Identical radar altimeters possible for Mars, Mercury and Moon and Galilean satellites
- Range/doppler navigation system can be used for gravity measurements

Effect of Atmosphere

- Atmospheric attenuation on Venus precludes the use of the 15 GHz radar on that planet
- Atmospheric drag limits the performance of a Mars gravity experiment

Orbit Design Issues

- Circular polar orbits used for geochemical remote sensing are quite suitable for radar altimetry/gravity mission
- Possible conflicts with remote sensing experiments over orientation of orbital plane (at Mars, Moon and Mercury) or trajectory plane (at Galilean satellites) relative to the Earth

Experiment Performance

- Altitude resolution of 50 m with spot size of 5-10 km at Mercury, Mars and Galilean satellites
- Coverage of Mars and Mercury very extensive but sparse coverage of Jovian satellites will prevent determination of terms over third order in harmonic model of topography
- Gravitational field harmonics at Mercury and Mars and Galilean satellites determined to about 15, 12 and 3 degrees respectively

Table S.6

GEOLOGY ORBITER EXPERIMENT ADAPTABILITY

	Of Basic Techniques to Many Target Objects	Of Single Instrument Design to Many Target Objects	Of Single Instrument Design to Different Mission Modes	Of Instrument Capabilities to Nongeoscience Objectives
GEOCHEMISTRY				
Elemental Analysis				
- Gamma-Ray	Moderate	High	Low	Moderate
- X-ray Fluorescence	Moderate	Moderate	Moderate	Moderate
- Atomic Spectroscopy	Low	High	High	High
Mineral Analysis				
- Visible UV near IR Reflectance Spectroscopy	High	High	Moderate	Low
- IR Emission Spectroscopy	High	High	Moderate	High
GEOPHYSICS				
- Gravity Field and Altimetry	Very High	High	High	Low
GEOLOGY				
- Frame Imaging	High	Very High	High	Moderate
- Line Array Imaging	High	Very High	Low	Moderate

The adaptability of a single instrument design to different mission modes (Column 3) involves the effects of the choice of orbit on the geometry, resolution and duration of observation. Gamma-ray observations are degraded in highly elliptical orbits because of the reduced resolution and time of observation. Line imaging observations are degraded because of the inability to perform long-range observations with this kind of technique in a three axis stabilized spacecraft.

Geology orbiter instruments vary greatly in their adaptability to nongeoscience objectives. The radar instrument, for example, will not contribute observations useful in other disciplines. However, a high resolution spectrometer designed for the geoscience application of studying atomic emissions in the vicinity of the Galilean satellites has wide application of studies of planetary atmospheres and the physical processes in the Jovian magnetosphere. Thus, this instrument which has a low rating in its adaptability to different geoscience objectives rates very highly in adaptability as a general planetary science instrument.

1. INTRODUCTION

Exploration of planetary and satellite surfaces by remote sensing techniques has a number of advantages from the mission planning point of view when compared to exploration by means of landers. Of paramount importance is the relative ease of placing instrumented payloads into flyby or orbital trajectories in comparison to landing them on a planetary surface. The capability of exploring many different parts of a target object or even several different target objects with one payload during a given mission is also very significant. But these merits of the remote sensing approach are of little value unless it proves possible to perform meaningful measurements relevant to the nature of the surfaces being observed. This report is concerned with the application of a number of experiment concepts to the exploration of the surfaces of the terrestrial planets, outer planet satellites, and asteroids. The capabilities of these experiments are evaluated in the context of the effects of atmospheres, space environments, and orbital parameters. Candidate instruments for the lunar polar orbiter are judged in terms of their adaptability to geological missions directed at other target objects.

The scope of this study was necessarily limited to a small number of experiments. Those chosen were selected on the basis of relevance to major planetological problems and the absence of any previous detailed study. Imaging was excluded for the latter reason. There has been a great deal of analysis of imaging experiments and, although much of it is out of date, it was felt certain other experiments which had been subjected to very little detailed study deserved higher priority.

The major part of this report is devoted to geochemical experiments for which the determination of the elemental abundance in the surface materials is the major objective. Gamma-ray spectroscopy and x-ray spectroscopy have previously been successfully used in the remote observation of the moon during the missions of Apollo 15 and 16. Visual and ultraviolet spectrometers have also previously been flown on space missions, but not for the purpose envisaged here, which is to determine

surface compositions. This would be achieved not by observing light emitted from the surface of the planet but by observing the light emitted from a tenuous cloud of gas surrounding the planet or satellite, composed of atoms derived from the surface. To date, such a cloud exhibiting sodium and potassium emissions has only been observed in the vicinity of the Jovian satellite Io by means of ground-based observations. The more general applicability of this technique to other planets and satellites is considered in this report. The only geophysical experiment studied is the gravity field and altimetry experiment which is designed to determine the internal mass distribution and isostatic state of the target objects.

The set of target objects considered in the study includes Mercury, Venus, Moon, Mars, the Galilean satellites, and Titan. The asteroids were not included but they are accessible to all of the techniques discussed and we hope to apply the analytical methods developed to those bodies in the near future.

Wherever possible we have drawn upon earlier published work supplemented by informal communications with scientists who have worked directly with these various remote sensing techniques. However, earlier work is largely restricted to studies of the Moon and Mars. Moreover, we did find it necessary to update some of the earlier analyses on the basis of new information about the physical environment and to take account of new instrument capabilities. During the study additional new research results appeared in the scientific literature which affected some of the numerical results and conclusions reached from our analysis. These advances will, of course, continue and we have attempted to present our models and the physical data on which they depend with sufficient clarity that they can be easily updated as required by new information.

2. APPROACH AND BASELINE ASSUMPTIONS

In evaluating spacecraft experiments, there are a number of areas of commonality which are most usefully considered collectively before exploring the details of each particular experiment. The first area is the general approach to experiment evaluation, which is the next subject covered in this section. This is followed by information on the spacecraft design and the types of orbits that are assumed for the evaluation. Summaries are also given of what is known about the chemical and physical properties of the target objects considered in the study and what is known, or expected, of their space environments.

2.1 Approach to Experiment Evaluation

Each different geology orbiter experiment presents its own distinct problems. However, it is possible to formulate an approach to the evaluation of remote sensing experiments which allows these problems to be systematically recognized and evaluated. The overall methodology used to assess geochemical remote sensing experiments is presented in Table 2.1. Details of the application of the methodology to each experiment considered in this report appear in Sections 3, 4, and 5. This methodology is, unfortunately, not strictly applicable to the geophysical experiment since it depends on an active rather than a passive remote sensing technique. However, a basically similar systematic approach underlies our treatment of the geophysical experiment.

2.2 Baseline Spacecraft Designs

Experiments considered here are assumed to be conducted from a three-axis stabilized platform. Mariner-class spacecraft, which have served as the workhorses for planetary oriented missions for the last fifteen years, typify such a design. The steerable scan platform which is a basic feature of this spacecraft permits long-range reconnaissance-mode observations of small signal sources and a great variety of observing strategies when the target object is viewed at close range.

Table 2.1

APPROACH TO EVALUATION OF GEOCHEMICAL REMOTE SENSING

Step 1: Adopt models for the surface elemental composition and radiation environment of the target objects.

Step 2: Determine intensity of signal radiation from target body.

Step 3: Determine intensity of background (noise) radiation

(a) arising from target body

(b) arising from the spacecraft and the space environment where the observations are made.

Step 4: Conduct instrument performance calculations based on suitable instrument and orbit designs using information on the signal and background source strengths developed above.

Step 5: Assess instrument performance as a function of instrument type and mission mode to determine feasibility of obtaining useful geochemical information.

Elaborate observing sequences can be compiled on the ground and telemetered to the spacecraft where they are stored for execution later. Encounter science data acquisition is further enhanced by high rates of data transmission and extensive onboard data storage.

Two distinct design concepts have been employed in the Mariner-class spacecraft. With existing technology, the radioisotopic thermionic generator (RTG) is the favored system for interplanetary flight beyond about three astronominal units from the Sun. The neutron and gamma radiation emitted by an RTG has a significant impact on the performance of typical outer planet instrument payloads. For close encounters to the Galilean satellite, however, the effects of RTG radiation are exceeded by the electron and proton irradiation from the Jovian trapped radiation belts.

For missions to the inner planets and Mars, solar energy is the most efficient means of powering a spacecraft in terms of power subsystems mass. Although solar powered spacecraft are not hampered by radiation, instrument cooling becomes much more difficult technically. At Mercury, for example, the feasibility of passively cooling a gamma-ray spectrometer is yet to be demonstrated.

While it is understood that new spacecraft designs are presently under study for future planetary exploration, it is also quite probable (and assumed for purposes of this study) that they will retain those Mariner-class spacecraft characteristics which have been described here.

2.3 Baseline Orbit Design

The baseline orbit designs selected for the evaluation of experiment performance are summarized in Table 2.2. For the Moon the baseline orbit reflects the Lunar Polar Orbiter mission design (Ref. 2.1). For Mercury and Mars, the baseline orbits were defined in two JPL studies (Refs. 2.2 and 2.3). The eccentric orbit at Mercury results from the limited orbit insertion capability using ballistic trajectories for transfer to Mercury and does not represent the most desirable orbit from the science perspective. Missions to the Jovian system offer much more scope to the mission

Table 2.2

BASELINE ORBIT PARAMETER SELECTIONS

Test Object	Orbit Parameters				Surface Accessibility
	Type	Period	Inclination	Altitudes	
Moon	Circular	2 hours	85-95°	50-150 km	Complete
Mars	Circular	2.5 hours	96°	1000 km	Complete
Mercury	Eccentric	6 hours	70°	500-7,400 km	Nearly Complete
Galilean Satellites	Jupiter-centered	2-17 days	0-40°	500-10,000 km (min. range)	10-20 Encounters of Each Satellite Covering All Latitudes

designer with the use of gravity assist at the Galilean satellites and the consequent flower orbits. The variable baseline orbit adopted here comes from the so-called quadrature tour mission (Ref. 2.6) which was designed primarily for imaging of the satellites. This mission includes 10 to 20 passes of each Galilean satellite in the terminator plane (90° phase angle) targeted to near polar trajectories. Approach distances as close as 500 km have been assumed for the experiment performance analyses. A second type of orbit about Jupiter, considered for the geochemical experiments, was one in which the spacecraft is in a high-inclination orbit. This orbit carries the spacecraft out of the intense trapped radiation belts near the magnetic equator of the planet (Figure 2.1), and is used for long-range observations of the satellites (described below). An optimal inclination has not been rigorously determined for this type of mission in the Jovian system; for the experiments considered here it was assumed that the spacecraft orbit would be inclined about 30°-40° to the magnetic equator.

For the geochemical experiments the observing time and the spatial resolution of the observations are parameters of key importance. The fields-of-view (FOVs) of the instruments and the range of the observations control the spatial resolution. It is assumed in the analyses performed here that the instrument FOVs define the angular resolution of the remote sensing instruments, i.e., that these are spectrometers and not imaging spectrometers.

The trajectory type has a major influence on instrument response, resolution and observing time. Very different scientific opportunities occur: (1) when the spacecraft is orbiting the object which is being observed, (2) when it executes close hyperbolic encounters, and (3) when it conducts long-range observatory mode reconnaissance.

The instrument response depends on whether or not the target body fills the FOV. If it does, as is generally the case for orbiters and for flybys near periapse, then signal strengths are independent of distance to the target body. However, spatial resolution does vary with distance, and orbiters, obviously, allow much greater observing time than do flybys.

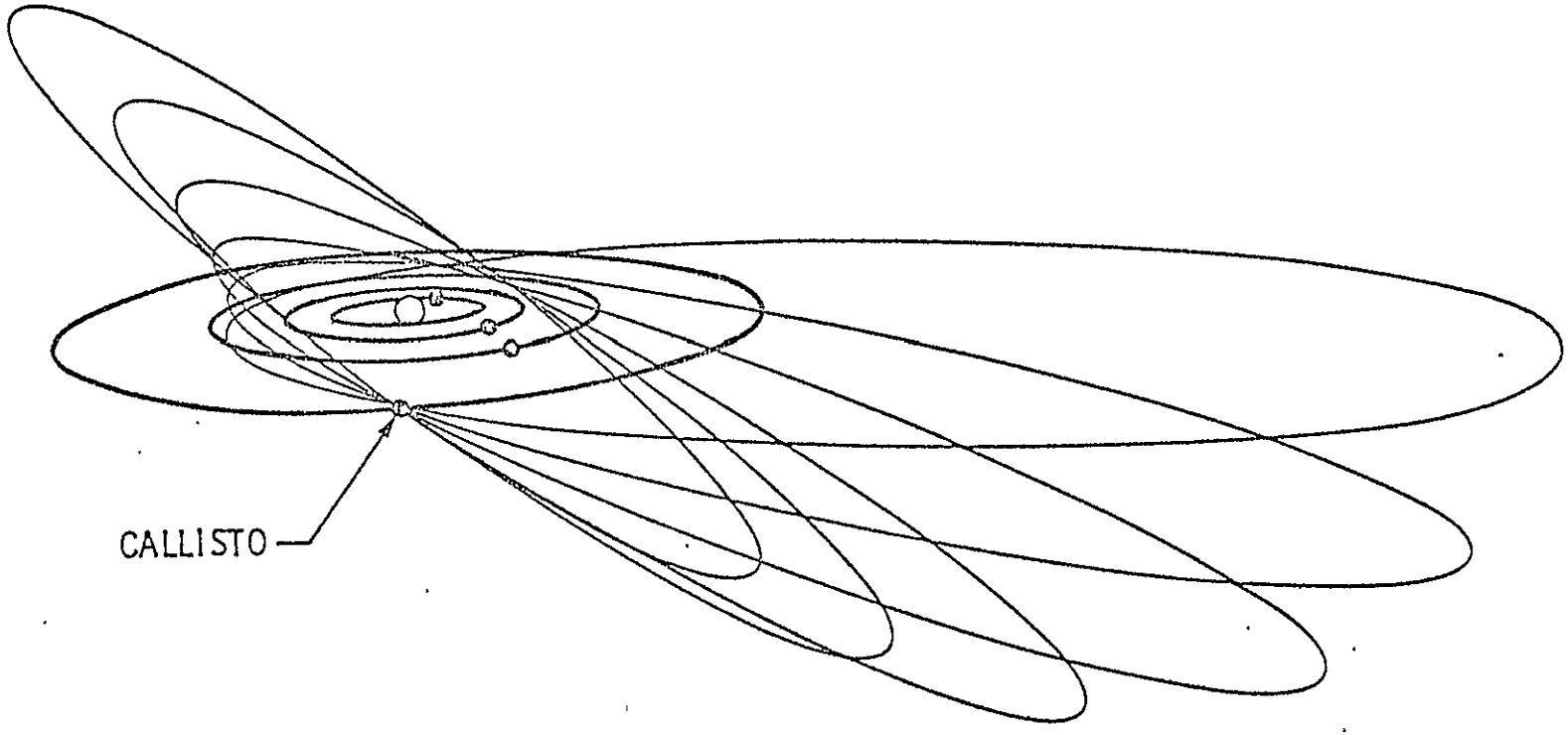

Figure 2.1 High Inclination Orbits Obtainable with Satellite Gravity Assist; in This Case, "Cranking" on Callisto.

The observatory mode of reconnaissance is quite relevant to the observations of the Galilean satellites from a Jupiter Orbiter and it is useful at this point to illustrate some typical features of this mode of data acquisition.

Beyond the range when the target object fills the instrument field of view no spatial resolution of the target is possible except for that provided by target rotation. Moreover, the number of photons received from the object begins to decline as the inverse square of the range. An effective observing time ratio (R_{EOT}) has been defined for observations during a small incremental interval of actual time ΔT_A such that the corresponding small incremental interval in effective observing time ΔT_E is given by

$$\Delta T_E = R_{EOT} \times \Delta T_A \qquad (2.1)$$

In Figure 2.2 the value of R_{EOT} is plotted as a function of time from periapsis for two approach trajectories with differing approach speeds at Ganymede. The effective observing time T_E over an interval of actual time can be obtained by integrating ΔT_E which corresponds to determining the area under some portion of the curve of Figure 2.2.

2.4 Chemical and Physical Properties of Planets and Satellites

The chemical and physical properties of the planets and satellites determine the magnitude of the various physical phenomena that are observed by remote sensing experiments. Where the mechanisms operative in these phenomena are reasonably well understood, then it is possible to predict the magnitude of the phenomena at issue given physical or chemical characteristics of the planet or satellite. Conversely, given the magnitude of the phenomena, then the physical or chemical properties of the planet or satellite can be determined and this is generally the way in which data from a remote sensing experiment is employed. To assess the feasibility of a remote sensing experiment, "reasonable" values for physical and chemical properties are usually adopted and used to determine

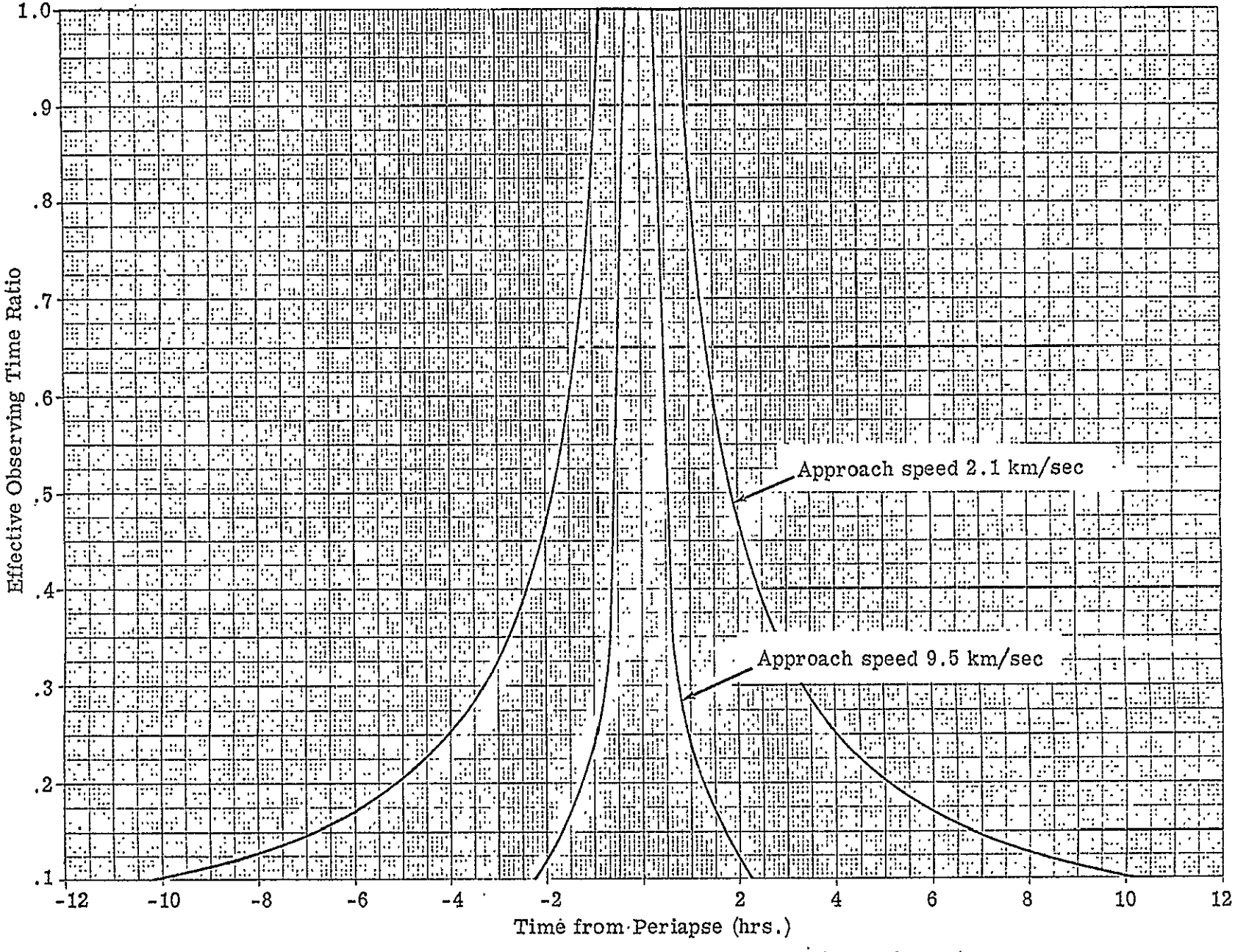

Figure 2.2 Detector Response Along Approach Trajectories to Ganymede.

whether they result in detectable phenomena and, subsequently, an assessment is made of how precisely that phenomena can be observed. If the proposed remote sensing experiment does not pass this test, then its credibility lies in serious doubt. There are, of course, other problems such as uncertainties in the mechanism of a physical phenomenon and the lack of a unique relationship to any particular physical or chemical property that will affect the merits of a remote sensing experiment.

Compositional models assumed for evaluation of the gamma-ray, x-ray, and atomic spectroscopy experiments are summarized in Tables 2.3(a) and 2.3(b). In the study of the gamma-ray experiment, we evaluate the feasibility of elemental detection on the basis of a lunar basalt composition for all objects. A lunar basalt composition is also assumed at Mercury for evaluation of the x-ray experiment. In the case of the x-ray and atomic spectroscopy experiment for the Galilean satellites, the compositions examined are based in part on recent Earth-based measurements. These data (Ref. 2.7) suggest evaporite composition for Io. Carbonaceous chondrite compositions are assumed for the other satellites.

2.5 Radiation Environment

Of the objects studied, only the Galilean satellites must be observed in a trapped radiation environment with intense fluxes of particles with energies exceeding 1 MeV. However, either structured streams or impulsive bursts of electrons and protons accelerated to several hundred keV are commonplace within a few planetary radii of Mercury.

Radiation data for the Jovian system used here is based on the work of Divine (Refs. 2.9 and 2.10) and Kloster (Ref. 2.11). Trapped radiation has a major effect on signal and background electromagnetic radiation intensities for observations of gamma-rays and soft x-rays. It also affects the instrument background for observations of these radiations and resonance emission of neutral atomic species (Refs. 2.12 to 2.16).

Table 2.3(a)

COMPOSITIONS[1] ASSUMED IN EVALUATION OF GEOCHEMICAL REMOTE SENSING EXPERIMENTS

Experiment	Target Object				
	Moon	Mars	Mercury	J_1	J_2, J_3, J_4
Gamma-Ray Spectroscopy	LB	LB	LB	LB[2]	LB[2]
X-Ray Fluorescence Spectroscopy	LB	NA	LB	CC,E	CC
Atomic Spectroscopy	NA	NA	NA	E	CC,E

Explanation of Symbols

LB	Lunar Basalt
CC	Carbonaceous Chondrite
E	Evaporite
NA	Not Applicable

[1]Compositional definitions given in Table 2.3(b).

[2]Estimates were made of consequences of different compositional assumptions, such as carbonaceous chondrite and evaporite.

Table 2.3(b)

ABUNDANCES[1] OF ELEMENTS IN CANDIDATE SURFACE MATERIALS FOR MOON, MARS, MERCURY AND GALILEAN SATELLITES[2]

Element	Lunar Basalt[2]	Carbonaceous Chondrite[2]	Evaporite[3]
Li	1.2^{1}	1.3^{0}	NA
Be	2^{0}	4^{-2}	NA
B	2^{0}	5^{0}	NA
C	1.4^{2}	3.5^{4}	NA
N	1.0^{2}	2.6^{3}	NA
O	4.0^{5}	4.5^{5}	2.3^{5}
F	1.4^{2}	1.9^{2}	NA
Na	3.3^{3}	5.5^{3}	1.1^{5}
Mg	4.5^{4}	9.6^{4}	2.5^{5}
Al	5.6^{4}	8.5^{3}	2.5^{3}
Si	1.9^{5}	1.0^{5}	3.7^{4}
P	5^{2}	1.4^{3}	NA
S	1.7^{3}	6.2^{4}	1.1^{5}
Cl	1.4^{1}	2.6^{2}	NA
K	1.4^{3}	1.4^{3}	2^{4}
Ca	8.0^{4}	1.1^{4}	6.8^{4}
Sc	7.5^{1}	5^{0}	NA
Ti	5.9^{4}	4.2^{2}	NA
V	5.0^{1}	5.7^{1}	NA
Cr	2.1^{3}	2.2^{3}	NA
Mn	1.9^{3}	1.7^{3}	7^{3}
Fe	1.4^{5}	1.8^{5}	8^{-2}
Co	2.5^{1}	4.8^{2}	NA
Ni	NA	1.0^{4}	2.9^{4}
Th	2.0^{0}	4^{-2}	NA
U	5.0^{-1}	1^{-2}	NA
Other Elements	NA	NA	$<1.4^{5}$

[1]Given in ppm, NA denotes Not Available.

[2]Data reproduced from Table 7.1 in Ref. 2.8.

[3]Data supplied by F. P. Fanale of the Jet Propulsion Laboratory.

Electron fluxes in the Jovian system as determined by Divine (Ref. 2.9) are tabulated in Table 2.4. There is considerable uncertainty in the values at high Jovian latitudes. Omnidirectional proton fluxes in the vicinities of the satellites are summarized in Table 2.5. The values in the vicinities of the satellites are quite reliable but uncertainties again exist for high magnetic latitudes.

Information on accelerated particles in the vicinity of Mercury is much less complete. Fluxes of protons with energies of $\approx$ 500 keV and electrons with energies of $\approx$ 300 keV which exceed approximately 10^4 and 10^5 cm^{-2} sec^{-1}, respectively, have been discovered in the magnetosphere of Mercury. Electron fluxes with somewhat lower intensities have also been observed in the magnetosheath. Intensity versus time profiles show sudden onsets with persistence for time periods of several tens of seconds and time periods between events of two or three times this. Fluxes decrease rapidly with energy. For a spectral form $dJ/dE \propto E^{-\gamma}$ where J is the particle intensity and E is the kinetic energy, typical values of γ are: (1) $\gamma_p = 5.5$ for protons above 500 keV and (2) $\gamma_e \geq 9$ for electrons above 170 keV (Ref. 2.17).

Table 2.4

ELECTRON FLUXES IN THE JOVIAN SYSTEM[1]

Object	Location[2]		Omnidirectional Electron Flux[3] ($cm^{-2}sec^{-1}$) with Energy Greater Than Listed Values in MeV							
	Range R_j	Latitude (degrees)	0.06	0.16	0.55	3.2	9.0	21	31	35
J_5	2.54	0	7.15^{7}	6.79^{7}	5.51^{7}	3.47^{7}	2.13^{7}	8.71^{6}	4.77^{6}	3.88^{6}
J_1	5.89	0	3.24^{8}	1.10^{8}	5.26^{7}	2.99^{7}	1.45^{7}	2.89^{6}	9.24^{5}	6.23^{5}
J_2	9.38	0	1.37^{8}	8.30^{7}	4.21^{7}	1.39^{7}	4.27^{6}	4.60^{6}	1.01^{5}	6.02^{4}
J_3	14.96	0	1.24^{8}	4.59^{7}	1.16^{7}	4.70^{5}	4.21^{4}	6.33^{3}	2.78^{3}	2.16^{3}
J_4	26.31	0	7.01^{5}	2.60^{5}	6.56^{4}	2.66^{3}	2.39^{2}	35	15	12
-	16.00	52	-	-	-	1.23^{4}	-	-	-	-
-	32.00	52	-	-	-	10	-	-	-	-
-	40.00	30	-	-	-	10	-	-	-	-

[1]Based on numerical interpolation of data in a model documented in Ref. 2.9.

[2]The first five entries are applicable to the fluxes experienced by the satellites and by spacecraft executing close encounters to the satellites. Fluxes are parameterized in terms of magnetic latitude; fluxes listed here are peak values for the satellites which undergo excursions between magnetic latitudes of +10 and -10. Charged particle sweeping is also ignored. The last three entries are applicable to fluxes experienced by the spacecraft during long-range 'observatory-mode' operations. In these cases latitudes are interpreted as subspacecraft Jovian latitudes but are close to a mean magnetic latitude for the purpose of these estimates.

[3]Throughout this report the numerical format indicating the exponent of 10 as a superscript is used, i.e., $7.15 \times 10^{7} = 7.15^{7}$.

Table 2.5

PROTON FLUXES IN THE JOVIAN SYSTEM[1]

Object	Range (R_j)	Equatorial Omnidirectional Proton Flux[1] (cm^{-2} sec^{-1}) with Energies Greater Than the Listed Values in MeV			
		1.0	5.0	E > 10	E > 30
J_1	5.89	2.5^{6}	5.7^{5}	3.1^{5}	5.9^{4}
J_2	9.38	1.7^{7}	6.9^{5}	1.8^{5}	1.0^{4}
J_3	14.96	-	-	-	-
J_4	26.31	-	-	-	-

[1]Based on numerical interpolation of data in the model described in Ref. 2.10.

REFERENCES

2.1 Lunar Polar Orbiter Interim Technical Report. Goddard Space Flight Center, Document X703-75-141, May 1975.

2.2 Planetary Mission Summary: Mariner Mercury Orbiter 1978. NASA SP43-10, Vol. 17, August 1974.

2.3 Planetary Mission Summary: Mars Polar Orbiter. NASA SP43-10, Vol. 2, August 1974.

2.4 Pioneer Venus Orbiter Scientific Instrument-Radar Mapper. Pioneer Program Document PC-417, NASA Ames Research Center, November 1974.

2.5 Planetary Mission Summary: Venus Orbital Imaging Radar. NASA SP43-10, Vol. 12, August 1974.

2.6 Planetary Mission Summary: Mariner Jupiter Orbiter. NASA SP43-10, Vol. 6, August 1974.

2.7 Fanale, F. F., T. B. Johnson and D. L. Matson, "Io: A Surface Evaporate Deposit," Science, Vol. 186, p. 922, 1974.

2.8 Mason, B. and W. G. Melson, The Lunar Rocks, Wiley Interscience, p. 176, 1970.

2.9 Divine, N., A Jupiter Electron Flux Model Based on Pioneer 10 and 11 Data (January 1976). Jet Propulsion Laboratory IOM 2947-76-04, January 1976.

2.10 Divine, N., Jupiter Radiation Models for Usage in MJS-77 Spacecraft Design. Jet Propulsion Laboratory IOM 2949-74-81, August 1974.

2.11 Kloster, R. L., "The Impact of Jupiter's Trapped Radiation on Probe Missions," in Proceedings of the AIAA/AGU Conference on the Exploration of the Outer Planets, AIAA Paper No. 73-1163, 1973.

2.12 Parker, R. H., "Radiation Effects on Science Instruments in Grand Tour Type Missions," in Proceedings of the National Symposium on Natural and Man Made Radiation in Space, March 1971.

2.13 Parkinson, J. B. and E. Gordon, "Radiation Noise in a High Sensitivity Star Sensor," in Proceedings of the National Symposium on Natural and Man Made Radiation in Space, March 1971.

2.14 Killiany, J. M., W. D. Baker, N. S. Saks and D. F. Burke, "Effects of Ionizing Radiation on Charge Coupled Imagers," in Proceedings of the Symposium on Charge Coupled Device Technology for Scientific Imaging Applications, Jet Propulsion Laboratory SP43-21, June 1975.

2.15 Carnes, J. E., A. D. Cope, L. R. Rockett and K. M. Schlesier, "Effects of Radiation on Charge Coupled Devices," in Proceedings of the Symposium on Charge Coupled Device Technology for Scientific Imaging Applications, Jet Propulsion Laboratory SP43-21, June 1975.

2.16 Detector Radiation Effects in Study of Spin Scan Imaging for Outer Planets Missions. Santa Barbara Research Center, Contract No. NA2-7096, Document CR 114745, February 1974.

2.17 Simpson, J. A., J. H. Eraker, J. E. Lamport, P. H. Walpole, "Electrons and Protons Accelerated in Mercury's Magnetic Field," Science, Vol. 185, p. 4146, 1974.

3. GAMMA-RAY SPECTROSCOPY

Gamma-ray spectrometers have been used successfully in the Apollo program (Ref. 3.1) to map key elemental abundances over a portion of the lunar surface. The improved gamma-ray spectrometer proposed for the lunar polar orbiter (a high purity Ge detector rather than the NaI(Tl) detector used on the Apollo missions) should yield improved information concerning elemental abundances over the entire surface. These studies will be important in determining the composition and geochemical history of the Moon. The purpose of this section will be to assess the potential of gamma-ray spectrometers aboard orbiter missions to Mars, Mercury and the Jovian satellites.

Briefly, gamma-rays are produced by the naturally occurring radioactive elements, K, U and Th, and by the bombardment of a planetary surface by high energy particles. The energies of the gamma-rays are, in most cases, specific to a particular nuclear isotope. With suitable gamma-ray detectors one can identify the emitting nucleus and, from the intensity of the flux of gamma-rays, determine the concentration of the particular element at the surface.

Elemental abundance measurements at Mars and Mercury are a fairly straightforward extension of the lunar experiments. Although a thin atmosphere affects both the transmission of gamma-rays from the surface to the observing spacecraft and also the production rate of cosmogenic gamma-rays (Ref. 3.2), the gamma-ray experiment is viable at Mars. But, at Venus and Titan the atmosphere is so dense that gamma-rays from the surface are completely absorbed.

In order to judge the feasibility of a gamma-ray spectrometer experiment at the Galilean satellites one must take into account the trapped radiation belts and the radiation from the on-board RTG power source. Therefore, a large part of this section is devoted to a new assessment of the signals and backgrounds that can be expected when operating a gamma-ray spectrometer in the Jovian system.

3.1 Estimated Gamma Line Intensities at the Moon, Mars and Mercury

The flux of gamma-rays from naturally occurring radioisotopes will depend on the concentration of these elements at the planetary surface. Table 3.1 lists the energies and predicted relative strengths (Ref. 3.3) for the various lines of naturally occurring radioactive decay chains of potassium, thorium, and uranium for a lunar composition. If the compositions of these radioisotopes at the surface of Mars and Mercury are similar to those at the Moon then the gamma line emission will be similar. At Mars, however, the flux emerging from the top of the atmosphere can be attenuated from as little as 15% to as much as 65% (Ref. 3.2).

For the Moon, Mars, and Mercury, the sources of high energy protons exciting gamma emission are the solar cosmic rays (SCR) and galactic cosmic rays (GCR). The SCR are emitted irregularly from the sun in a few intense solar flares around the solar maximum during the 11-year solar cycle. Only those gamma-rays that result from the decay of radionuclides produced by SCRs are measurable, since the high intensity of charged particles present during the flare itself would saturate a remote sensing gamma-ray detector precluding the detection of prompt SCR produced gamma-rays. Since very few SCR protons exceed energies of 100 MeV, the major induced activities are produced by (p,n), (p,np) and similar low energy nuclear reactions.

The estimates of average signal fluxes induced by SCRs appearing in Table 3.1 were calculated (Ref. 3.3) with a physical model in which the characteristics of an average solar flux were approximated by an exponential rigidity function with a rigidity of 100 MV. It gives a fair representation of the flux to which the Moon is exposed as verified by lunar sample studies.

The signal fluxes due to short-lived ^{48}V and ^{56}Co isotopes, giving rise to the lines at 0.983 and 1.312 MeV diagnostic of Ti, and at 0.847 and 1.238 MeV diagnostic of Fe, will vary markedly throughout the solar cycle. The fluxes due to somewhat longer-lived ^{54}MN and ^{22}Na isotopes, giving rise to lines at 0.835 MeV from Fe and 1.275 MeV from Na, Mg, Al,

Table 3.1

LUNAR GAMMA-RAY FLUX FROM NATURAL AND SCR-INDUCED RADIOISOTOPES

(Predicted for an Apollo 11 Basalt Composition)[1]

Source	Element	Energy (MeV)	Flux (photons/cm^2-sec)	Expected Flux at Mars and Mercury
Natural Radio-isotopes[1]	^{40}K	1.46	.0395	
	Th series	0.239	.0177	Comparable to Moon; depends only on composition
		0.583	.0170	
		0.91	.0153	
		0.97	.0137	
		2.614	.0402	
	U series	0.352	.0127	
		0.609	.0207	
		1.120	.0098	
		1.746	.0123	
Solar Cosmic-ray Induced Radio-isotopes[1,2]	Na, Mg, Al, Si	1.275	.0052	Smaller for Mars due to atmospheric attenuation of cosmic rays and distance. Much higher for Mercury due to proximity of the Sun.
	Al, Si	1.809	.0123	
	Ti	0.983	.0028	
		1.312	.0030	
	Fe	0.835	.0023	
		0.847	.0056	
		1.238	.0038	

[1]Assumed composition is very similar to that given in Section 2. Only the most prominent lines are listed. These data were generated prior to the Apollo orbital gamma-ray experiment and have not been updated to reflect the comparison of orbital gamma-ray data with ground truth.

[2]The fluxes listed here are predicted for a 4π integral flux above 10 MeV of 100 protons/cm^2-sec and a spectral rigidity of 100 MeV. This flux approximates the characteristics of SCR at the Moon averaged over a solar cycle.

and Si in surface materials, will display slow temporal variations. The flux due to ^{26}Al at 1.809 MeV arising from Al and Si in surface materials will show no variations over a solar cycle.

The lunar SCR-induced fluxes are typically a factor of 5-10 smaller than fluxes arising from radioisotopes. At Mars one can expect these SCR-induced fluxes to be still smaller because of the greater distance from the Sun and the atmospheric attenuation of the SCRs. However, at Mercury the SCR-induced fluxes will be much higher than at the Moon. Unfortunately, many of the SCR lines cannot be associated uniquely with a single element and this reduces their value to elemental analysis.

A most important source of gamma line emission at the Moon, Mars and Mercury is GCR bombardment. These highly energetic protons produce neutrons and mesons in planetary surfaces through nuclear interactions. Gamma radiation arises mainly from the interaction of the secondary neutrons with the surface materials (Refs. 3.3, 3.4, and 3.5). These neutrons will produce gamma-rays either through fast-neutron inelastic scattering or slow-neutron capture reactions, depending on the surface composition. Since the lunar surface contains little neutron moderating material (specifically hydrogen), inelastic scattering is the dominant gamma-ray production mechanism. Predicted fluxes from the lunar surface for galactic cosmic-ray induced gamma-rays are tabulated in Table 3.2 with the data classified into fast and slow neutron reactions. Note that the expected fluxes for abundant elements such as O, Mg, Al and Si are comparable to fluxes from natural radioisotopes.

The surface of Mercury is also expected to contain little hydrogen and the results calculated for GCR bombardment of the Moon should be directly applicable to Mercury, as GCRs do not vary significantly within the inner solar system. However, if Mars has a considerable amount of water in the surface layers, as many workers have suggested, the slow-neutron induced gamma fluxes may be enhanced by a factor of 2-5 (due to the neutron moderating properties of hydrogen) over those appearing in Table 3.2 for otherwise similar compositions. Where rare earth elements with high absorption cross sections for slow neutrons occur in abundance,

Table 3.2

LUNAR GAMMA-RAY FLUX INDUCED BY GALACTIC COSMIC RAYS

(Predicted for an Apollo 11 Basalt Composition)[1]

Source	Element	Energy (MeV)	Flux (photons/cm^2-sec)	Expected Flux at Mars and Mercury
Fast Neutron Reactions	O	6.13	.0405	Comparable; depends only on composition
		7.12	.0157	
	Mg	1.37	.0130	
	Al	2.21	.0072	
		3.00	.0047	
	Si	1.78	.0562	
	Fe	0.85	.0255	
Slow (thermal) Neutron Reactions	Al	7.72	.0015	Could be a factor of 2-5 higher at Mars if surface is water rich
	Si	3.54	.0045	
		4.94	.0057	
	Ca	1.94	.0035	
		4.94	.0057	
	Ti	1.38	.0162	
		6.42	.0178	
		6.75	.0278	
	Fe	7.64	.0250	

[1]Assumed composition is similar to that given in Section 2. Only the most prominent lines are listed. These data were generated prior to the Apollo gamma-ray experiment and have not been updated to reflect the comparison of orbital gamma-ray data with ground truth.

then slow-neutron induced gamma fluxes from other elements will be reduced. Apart from the effects of hydrogen and rare earth elements, fluxes will scale approximately with elemental abundance and certainly within a factor of 2 (Ref. 3.2) which is within the limits of accuracy that are relevant to this study. One other effect which will be important at Mars is the emission at 1.46 MeV due to cosmic-ray interactions with atmospheric argon. The observation by Viking of low argon abundance suggests that argon interference will not be a major problem.

3.2 Estimated Gamma Line Intensities at the Galilean Satellites

The compositions of the Galilean satellites are known to differ markedly from lunar composition (Section 2.3). However, we shall continue to use the Apollo 11 basalt model calculations of Reedy (Ref. 3.3) as the basis for computations of gamma flux from these objects. However, we will indicate for what modes of gamma emission the fluxes scale linearly with the abundance of the target elements and for what modes and compositions they do not. In the latter cases we will make rough estimates of the fluxes for other compositions although realistic models require detailed calculations of the transport of high energy protons in the expected composition which is beyond the scope of this study.

For the naturally occurring radioisotopes, the source gamma flux does scale with the abundance of the element and, given radioisotopic abundances, the source gamma flux can be estimated for the Galilean satellites from Table 3.1. Europa, Ganymede, and Callisto are expected to be undifferentiated bodies with very low uranium and thorium compared to the Moon. Therefore, gamma-ray fluxes from all these elements are expected to be very much lower than those for the Apollo basalt. The unique surface of Io, if it is evaporitic (Ref. 2.7), will also be low in uranium and thorium but may be higher in potassium. The consequences of these differences can be readily assessed.

The flux of high-energy GCRs should be the same at the orbit of Jupiter as it is at the Earth. The GCR-induced flux from the Galilean satellites can be scaled with composition from Table 3.2 taking into

account the effect of hydrogen as indicated previously. Much larger amounts of hydrogen (water frost) are expected on the surfaces of Europa, Ganymede, and Callisto than even on Mars and this will enhance the thermal neutron capture gamma-rays. Since the flux of SCR relative to the Moon is down by a factor of 25 at the Galilean satellites, the flux of SCR-induced gammas is considered negligible.

Intense fluxes of gamma-rays are induced by the interaction of the Jovian satellites with very high energy magnetospheric particles. The Galilean satellites Io, Europa, and Ganymede are located in the stable radiation trapping zone around Jupiter. Callisto is located in the quasi-trapping region. All of these satellites will thus be subjected to the bombardment of high energy protons and electrons. The proton bombardment will give rise to gamma radiation while the electron bombardment will produce bremsstrahlung. These will be the dominant gamma-ray stimulation and background production mechanisms for the inner-most satellites. The energy spectrum for trapped protons can be approximated over the spatial region from R = $3R_J$ to 10 R_J as a power law (Ref. 2.10) which decreases with energy as $(E/E_0)^{-5.5}$ for proton energies above 30 MeV. This distribution is somewhat similar to the 50 MV-rigidity solar cosmic-ray distribution for which Armstrong (Ref. 3.5) determined fluxes of prompt gammas for a lunar composition. The source fluxes determined by Armstrong (Figure 3.1) can be combined with data on the proton fluxes at the Galilean satellites (Table 2.5) to give the prompt gamma fluxes induced by trapped proton bombardment of the surfaces of the satellites. These estimates (Table 3.3) are necessarily very approximate. Both the prompt fluxes generated and the delayed fluxes arising from the decay of radionuclides produced under proton bombardment contribute to the emission from the satellites. Source fluxes of gamma-rays at Io, which is a more intense source of gamma-rays than the other Galilean satellites, is 2 to 3 orders of magnitude greater than expected from the Moon, Mars or Mercury.

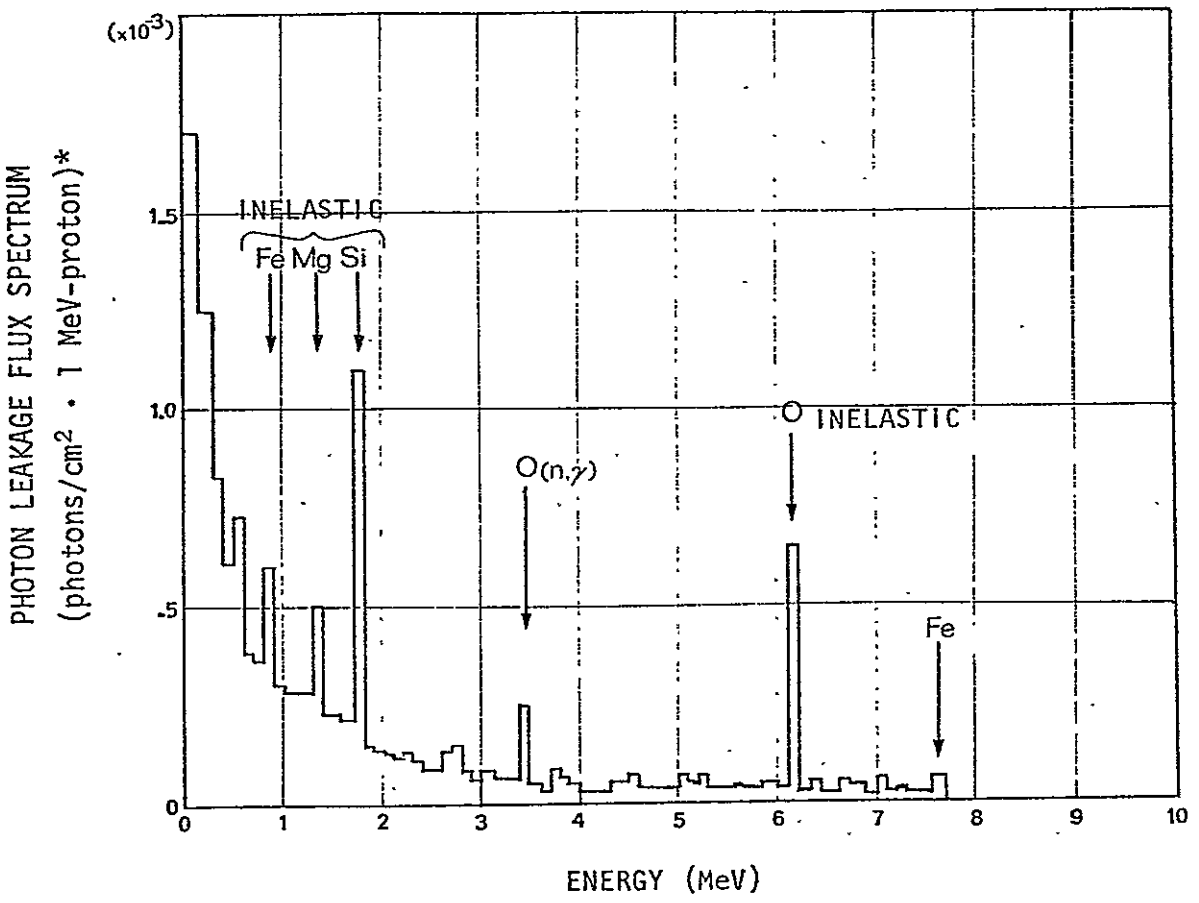

*Flux shown for 0.1 MeV energy intervals.

Figure 3.1 Predicted Spectrum of Prompt Photons from the Surface of the Moon (Apollo 11 composition under SCR bombardment).

Table 3.3

GALILEAN SATELLITE GAMMA-RAY FLUXES
INDUCED BY TRAPPED JOVIAN MAGNETOSPHERIC RADIATION

Class	Element	Energy (MeV)	Photon[3] Leakage Flux (ph/cm^2-sec-proton)	Trapped Proton Induced Flux[4] (photons/cm^2-sec)			
				Io	Europa	Ganymede	Callisto
Prompt[1] Photons	O	3.45	2.3^{-5}	0.92	0.12	-	-
		6.2	6.2^{-5}	2.5	0.31	-	-
	Mg	1.35	2.5^{-5}	1.0	0.125	-	-
	Si	1.7	9.5^{-5}	3.8	0.48	-	-
	Fe	0.9	2.0^{-5}	0.8	0.10	-	-
		7.8					
Delayed[2] Photons	Na, Mg, Al, Si	1.275	5.1^{-5}	5.1	2.5	-	-
	Al, Si	1.809	1.23^{-4}	7.3	3.6	-	-
	Ti	0.983	2.9^{-5}	2.8	1.4	-	-
		1.312	3.0^{-5}	2.8	1.4	-	-
	Fe	0.835	2.3^{-5}	2.3	1.2	-	-
		0.847	5.6^{-5}	5.6	2.8	-	-
		1.238	3.9^{-5}	3.8	1.9	-	-

[1]Information on prompt photons is derived from Figure 4 in Ref. 3.4. These data somewhat underestimate prompt photons because energies below 30 MeV are excluded from the model. Trapped proton fluxes assumed in these calculations are 4.0×10^4 for Io, 5.0×10^3 for Europa and smaller values elsewhere with energies greater than 30 MeV.

[2]Information on delayed photons is derived from Table 3 in Ref. 3.3, which gives fluxes for a 4π integral proton flux above 10 MeV of 100 protons/cm^2-sec for a 100 MeV rigidity spectrum. Trapped-proton fluxes assumed in determining corresponding emission from the Galilean satellites with the same rigidity spectrum are 1×10^5 for Io, 5×10^4 for Europa.

[3]Note that the energy range of the stimulating proton fluxes is different for the prompt and delayed photons.

[4]Photon fluxes appearing in this table will be updated on the basis of a study of proton transport in candidate Galilean surface materials which is currently in progress.

3.3 Gamma-Ray Background at the Target Objects

The gamma-ray background or continuum emission has an important effect on the viability of gamma-ray remote sensing of element composition. In this section we will attempt to give estimates of the background at the Moon, Mars, and Mercury and at the Galilean satellites.

Moon, Mars, and Mercury

The gamma radiation emitted from the surface of the Moon consists of line emission at energies characteristic of the elements that compose the surface and a continuum emission. In general, the continuum represents a background from which the line emission must be resolved for elements to be recognized and their abundances determined. For the Moon, the continuum is primarily attributed to Compton scattering of photons originating beneath the surface and is believed to be a large fraction of the total flux observed near 1 MeV based on data obtained with a sodium iodide detector on Apollo 15 and 16 (Ref. 3.1). With a higher resolution detector, it is probable that many formerly unresolved emission lines would be identified, thereby permitting much better definition of the height of the continuum. In the calculations discussed here which cover detection of those elements with the most prominent gamma-ray lines we use the continuum data determined by Reedy (Ref. 3.3). The variation of this background flux with energy is given in Table 3.4 for a 2 keV energy bin. Continuum spectra assumed for the Moon are also applicable to Mars and Mercury, although as noted earlier in this section SCR-induced photons at Mercury may significantly increase the low energy background levels. For the elements with the strongest line emissions (Tables 3.1 and 3.2) the fluxes in the line spectra exceed those in the continuum background by two or three orders of magnitude.

Background Radiation in the Jovian System

The gamma-ray spectra of the Jovian satellites will have an additional continuum component originating in the trapped electron bombardment. The trapped electron bombardment of the surface of the Jovian satellites

Table 3.4

BACKGROUND (CONTINUUM) GAMMA RADIATION ORIGINATING FROM LUNAR AND GALILEAN SATELLITE SURFACES

Energy (MeV)	Background Flux (photons/2 keV-cm^2-sec)				
	Moon[1]	Galilean Satellites[2]			
		Io	Europa	Ganymede	Callisto
0.5	9.8^{-4}	2.8^{5}	8.4^{4}	8.4^{3}	4.8^{1}
1	3.9^{-4}	3.3^{5}	9.9^{3}	9.9^{2}	0.5^{1}
1.46 (^{40}K)	2.3^{-4}	1.0^{4}	3.0^{3}	3.0^{2}	1.7^{0}
2	1.5^{-4}	3.9^{3}	1.2^{3}	1.2^{2}	-
5	4.6^{-5}	2.3^{2}	6.8^{1}	0.6^{1}	-
6.1 (O)	3.5^{-5}	0.2^{3}	3.0^{1}	0.2^{1}	-
7.8 (Fe)	2.5^{-5}	5.0^{1}	0.7^{1}	0.8^{0}	-

[1]Gamma-ray continuum fluxes for the lunar material are derived from Reedy, Ref. 3.3, Figure 6. This also applies to Mars and Mercury.

[2]The gamma-ray continuum fluxes for the Galilean satellites were computed as described in the text.

will produce bremsstrahlung. This bremsstrahlung will have a continuous energy spectrum extending from a few keV up to the maximum energy of the trapped electrons. The line radiation from the nuclear decays of interest must be observable above the continuum for gamma-ray measurements to be practical.

There is not much information concerning the bremsstrahlung produced in the backward hemisphere by an isotropic (cosine law) source of electrons impinging on one side of a piece of material. It is known that the total bremsstrahlung energy radiated in aluminum varies approximately (Ref. 3.6) as $E^{1.81}$ in the energy region between 1 and 10 MeV. The angular distribution of the bremsstrahlung becomes more forward peaked as the energy increases, thereby reducing to some extent the net flux in the backward hemisphere. Data from Refs. 3.7 and 3.8 seem to indicate that the angular distribution is decreasing faster than the total intensity increases in the energy region between 4 and 10 MeV. Figure 3.2 shows a crude estimate of the bremsstrahlung produced in the backward direction as a function of electron energy. The points at low energy are from calculations for an isotropic electron flux on Al (Ref. 3.6). The higher energy points are from the angular distributions calculated from the Schiff formula (Ref. 3.9) and the work of Hansen and Born (Ref. 3.10) for 120° bremsstrahlung production for 1 and 6 MeV photons.

The estimated bremsstrahlung production rate was integrated with the electron energy spectrum (Ref. 2.9) for the orbits of Io, Europa, and Ganymede to estimate the bremsstrahlung backgrounds. The last four columns of Table 3.4 list the bremsstrahlung background in 2 keV bins (spectral resolution of the gamma-ray spectrometer; see Section 2.3) for a number of different gamma-ray energies. Comparing the data on line spectra in Table 3.3 with the data on continuum emission it is seen that the high-energy lines ($E > 6$ MeV) have the most favorable signal-to-background ratio. However, the estimated backgrounds exceed the signal strengths by large factors for all of the lines of interest. The high continuum backgrounds are very unfavorable for a gamma-ray elemental analysis experiment.

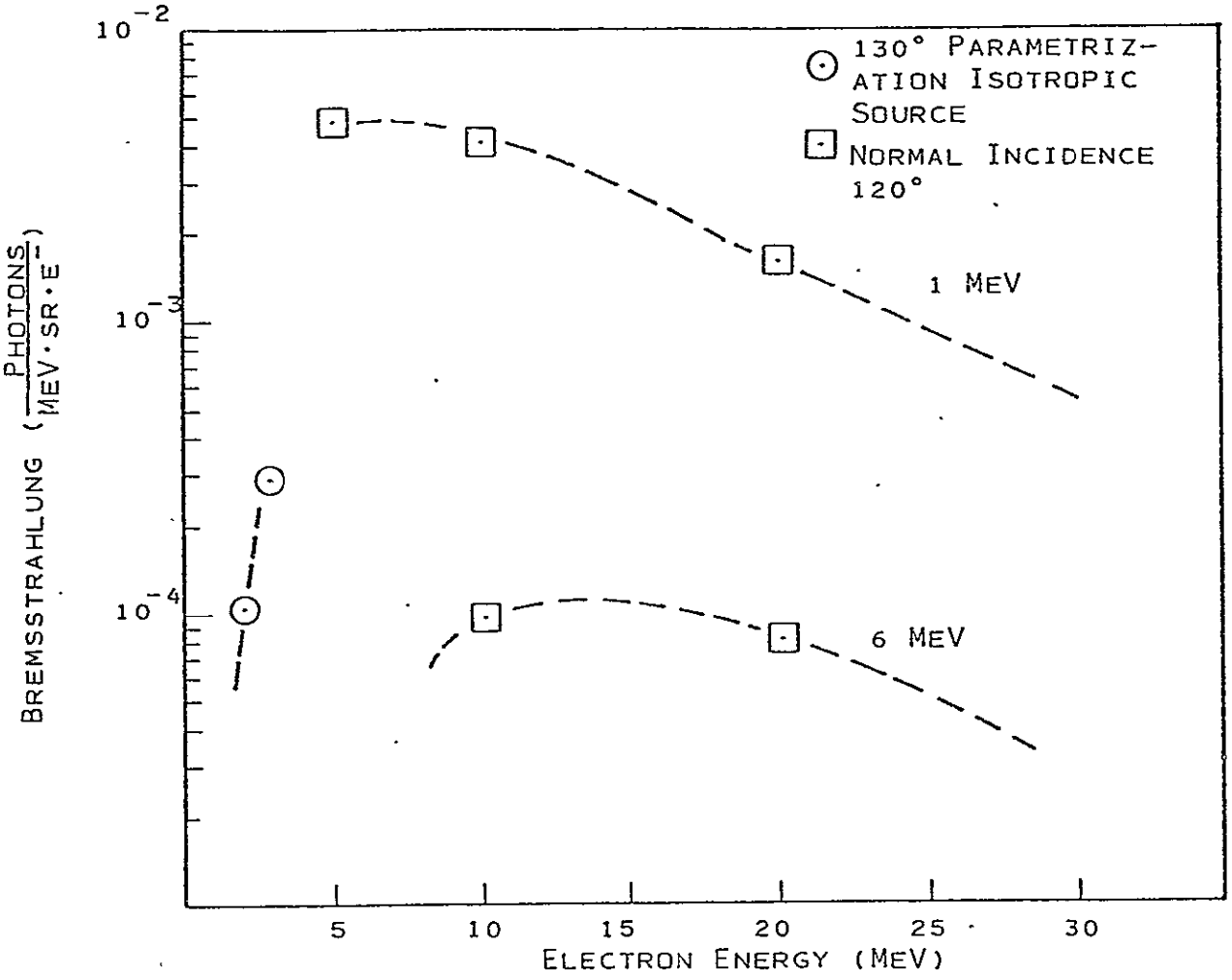

Figure 3.2 Estimated Bremsstrahlung Production Rate
Data from Refs. 3.6 and 3.9.

It should be emphasized that the uncertainties in these estimates are large and the estimates of signal-to-background may be unduly pessimistic. The lack of experimental data for high-energy electron bremsstrahlung in the backward direction is the main source of uncertainty. Experimental measurements should be made to determine if the bremsstrahlung background will pose as serious an obstacle to the detection of gamma-ray line emission from the Galilean satellites as the present estimates seem to indicate.

3.4 Instrument Background Due to the Spacecraft and Space Environment

Radiations originating within the spacecraft (such as the RTG or spacecraft materials containing radioactive elements), radiations arising from sources other than the source being actually observed, and radiations arising from the interaction of the spacecraft with its environment are additional contributions to instrument background.

Moon, Mars, and Mercury

Since these planets can be explored without RTG power sources and do not have trapped radiation belts, instrument backgrounds are low except during solar flare conditions. Charged particle bursts at Mercury will probably not be a significant problem because energies do not exceed 1 MeV. Cosmic charged particle background can be practically eliminated with coincidence counting. During the Apollo mission a significant buildup in radioactivity in the NaI detector and spacecraft component due to cosmic-ray bombardment was observed (Ref. 3.12). For missions to Mars and Mercury, which require much longer cruise periods, the buildup of longer lived isotopes is likely to be a significant source of background and interference, which must be compensated for in the data analysis phase of the experiment. However, the assessment of this effect is beyond the scope of this study.

A summary of the various sources of gamma spectrometer background for missions to the Moon, Mars, and Mercury appears in Table 3.5, Part A. The effects are minimized by locating the spectrometer on a long boom as far as possible from the main body of the spacecraft and by reducing the content of radioactivity in spacecraft materials to a minimum. By comparing detector count rates before and after boom extension during the Apollo mission, it was determined (Ref. 3.13) that the spacecraft contributed a small percentage of the detector counts. A summary of the magnitude of the components of background appears in Table 3.6.

Background Due to Trapped Jovian Radiation

In Section 3.3 the background (continuum) gamma-rays arising from the target object were computed. In the first part of this section we considered the background of gamma-rays from the spacecraft and space environment for missions to Mars, Mercury, and the Moon. For a gamma-ray spectrometer operating in the Jovian system there will be still other sources of background radiation. A summary of these additional sources is given in Table 3.5, Part B. Estimates of their magnitude appear in Table 3.6.

3.5 Experiment Performance Calculations

An assessment of the performance of remote sensing gamma-ray spectroscopy for elemental abundance determination can be made on the basis of signal and background intensities discussed previously. The procedures used for making these assessments are approximate and are intended to give order of magnitude estimates only. The purpose is to determine experiment feasibility and to provide guidance for new orbit or spacecraft design concepts.

Table 3.5

INSTRUMENT BACKGROUND FOR GAMMA-RAY EXPERIMENTS

Part A: Moon, Mars and Mercury Environments

(1) Prompt secondary gamma-rays produced by cosmic-ray interactions in satellite materials

(2) Direct charged-particle counts

(3) Radioactivity induced in the detector materials by cosmic-ray and trapped protons

(4) Radioactivity induced in detector materials by the planetary (e.g., earth or moon) albedo neutron flux

(5) Radioactivity induced in the detector materials by the interaction of secondary neutrons produced throughout the spacecraft by cosmic-ray and trapped proton interactions

(6) Radioactivity induced in spacecraft materials by the mechanisms outlined in 3, 4, and 5

(7) Natural radioactivity in spacecraft and detector materials

Part B: Galilean Satellite Environments (items plus above)

(8) Radioactivity in the spacecraft radioisotopic thermal generator (RTG)

(9) Radioactivity induced in the spacecraft by neutrons from the RTG

(10) Direct charged particle counts from the interaction of high energy magnetospheric protons and electrons

(11) Prompt secondary gamma-rays from the interaction of Jovian magnetospheric protons

(12) Radioactivity induced in spacecraft and detector by high energy Jovian magnetospheric protons

(13) Bremsstrahlung induced in the spacecraft and detector by high energy Jovian magnetospheric electrons

Table 3.6

INSTRUMENTAL BACKGROUND SOURCES FOR A GAMMA-RAY SPECTROMETER[1]

Sources	Moon[2], Mars and Mercury	Jovian System			
		Io	Europa	Ganymede	Callisto
A. DIRECT GAMMA RADIATION (counts/cm²-sec MeV)					
1. RTG					
1 MeV	Not	0.8	0.8	0.8	0.8
3 MeV	Applicable	0.5	0.5	0.5	0.5
2. Other Spacecraft Sources					
1 MeV	5.0^{-2}	5.0^{-2}	5.0^{-2}	5.0^{-2}	5.0^{-2}
10 MeV	5.0^{-4}	5.0^{-4}	5.0^{-4}	5.0^{-4}	5.0^{-4}
3. Cosmic Background					
1 MeV	2.0^{-1}	2.0^{-1}	2.0^{-1}	2.0^{-1}	2.0^{-1}
10 MeV	1.0^{-3}	1.0^{-3}	1.0^{-3}	1.0^{-3}	1.0^{-3}
B. CHARGED PARTICLES (particles/cm²-sec MeV)					
1. Solar Cosmic Rays					
Quiet Conditions	5.0^{-2}	-	-	-	-
Solar Flare Conditions	1.0	-	-	-	-
2. Galactic Cosmic Rays					
Solar Minimum	5.0^{-2}	5.0^{-2}	5.0^{-2}	5.0^{-2}	5.0^{-2}
3. Trapped Radiation-Close Encounters					
Electrons > 3 MeV	Not	3.1^{7}	1.4^{7}	5.4^{5}	3.5^{3}
Protons > 30 MeV	Applicable	1.0^{5}	7.0^{2}	> 10	< 1
4. Trapped Radiation-Observatory Mode					
Electrons > 3 MeV	Not	8.5^{6}	4.2^{6}	2.5^{5}	1.6^{3}
Protons > 30 MeV	Applicable	3.4^{3}	1.0^{3}	-	-
C. BREMSSTRAHLUNG (photons/cm²-sec MeV)					
1. Close Encounters					
3 MeV	Not	1.7^{5}	3.9^{4}	5^{3}	-
6 MeV	Applicable	6.5^{4}	7.0^{3}	6.5^{3}	-
2. Observatory Mode					
3 MeV	Not	4.7^{4}	1.2^{4}	2.3^{3}	-
6 MeV	Applicable	1.8^{4}	2.1^{3}	3.0^{3}	-

[1]The actual count rate induced in a gamma-ray detector in any given 2 keV energy bin is a function of the nature of the particle or photon and its efficiency of conversion in the detector. The gamma fluxes listed are given for a 1 MeV energy interval and are at the detector. In this form they are not directly comparable to the continuum flux from the surface (Table 3.4) which is the other major background component to an orbital gamma ray spectroscopy experiment.

[2]Instrument backgrounds for Moon, Mars and Mercury are very similar. Backgrounds are somewhat higher nearer the sun due to the enhanced SCR flux. The background will also increase with the length of the mission (see text) but this effect is not well understood.

Baseline Gamma Spectrometer

The baseline spectrometer (Table 3.7) is boom mounted and utilizes an intrinsic germanium detector. A plastic scintillator shield encloses the detector and serves to reject charged particles. Other design characteristics of the instrument are given in Table 3.7. Performance calculations are based on a 60 cm^3 germanium detector with an intrinsic detector efficiency ranging from 0.66 at 1.8 MeV to 0.016 at 7.5 MeV. The collimator is assumed to define a field of view of 36° (0.30 ster).

Observations of Moon, Mars, and Mercury

For observations for which the target more than fills the detector field of view, signal count rates (CR_S) can be related to the photon source strengths by:

$$CR_S = \emptyset \cdot Ei \cdot A \cdot Ta \cdot F_\gamma / \pi \qquad (3.1)$$

where: $\emptyset$ = detector field of view = 0.30 steradians
Ei = intrinsic photopeak efficiency
A = detector cross sectional area = 18 cm^2
F_γ = photon flux (photons/cm^2 sec) from planetary surface
Ta = atmospheric transmission.

A more exact expression for the count rate includes geometric constants; however, for these calculations these constants have been set to unity which is consistent with the order of magnitude evaluation desired.

The total background count rate (CR_B) in events/sec in the energy interval of the gamma-ray photopeak is:

$$CR_B = A \cdot \frac{\Delta E}{2.0} \cdot [B_{\gamma p} \cdot \emptyset \cdot Ei \cdot Ta + (1 - \Omega_p) \cdot B_{\gamma i} + \Omega_p B_{\gamma s}] \qquad (3.2)$$

Table 3.7

GAMMA-RAY SPECTROMETER FOR A GEOLOGY ORBITER

A. INSTRUMENT DESIGN CHARACTERISTICS[1]

Sensor

Type	High purity germanium, boom mounted
Temperature	120K (passively cooled)

Anticoincidence Shield and Collimator

Type	Hollow cesium iodide crystal

Weight

Sensor, without collimator	7 kg
Sensor, with collimator	16 kg
Electronics (inside bus)	2 kg

Power

Average	10 watts
Peak	12 watts

Data Rate

Real Time	4 kbps, 4000 energy channels

B. PERFORMANCE CHARACTERISTICS

Sensor Field of View			36 degrees
Sensor Effective Area			18 cm^2
Energy Resolution[2] @ 1.33 MeV			2 keV
Intrinsic Photopeak Efficiency			
Efficiency	@ 1	MeV	.060
	3	MeV	.040
	5	MeV	.025
	7.6	MeV	.016
	10	MeV	.015

[1]Instrument design information originally provided by A. E. Metzger is reproduced from Ref. 3.1.

[2]Energy resolution at other energies is determined assuming a square root dependence on gamma ray energy.

where: ΔE = energy increment of the photopeak (in keV)

$B_{\gamma p}$ = cosmic ray induced background flux from the planet (photons/cm^2-sec-2 keV)

$B_{\gamma i}$ = interplanetary gamma flux at the detector (photons/cm^2-sec-2 keV)

Ω_p = solid angle subtended by the planet at the spacecraft

$B_{\gamma s}$ = gamma flux at detector due to spacecraft interaction with neutrons emitted from the planetary surface,

and the remaining parameters are as defined for Equation 3.1.

Contributions to the background represented by the last two terms enclosed by brackets in Equation 3.2 are omitted in the numerical results on background presented below. The first of these terms is small because the interplanetary gamma flux is generally quite small; the second can be made small by deploying the instrument on a long boom so that Ω_p is small.

Equations 3.1 and 3.2 can be applied to the determination of signal-to-background count rates and signal-to-noise (S/N) for given values of the parameters in Equations 3.1 and 3.2.

$$\text{Signal-to-Background} = \frac{CR_S}{CR_B} \tag{3.3}$$

$$\text{Signal-to-Noise (S/N)} = \frac{CR_S \quad t^{\frac{1}{2}}}{(CR_S + CR_B)^{\frac{1}{2}}} \tag{3.4}$$

where t is the observation time in seconds.

In Table 3.8 signal-to-background and signal-to-noise have been determined at three different gamma-ray energies for a typical signal flux of 0.03 photons/cm^2 sec that is expected in these observations for several different observing times. Typical lunar background fluxes are also used. Several conclusions may be drawn from this presentation:

1) Signal-to-background is higher at the higher energies, an effect that is partly affected by gradually increasing photopeak width (decreased energy resolution);
2) Count rates for a given surface flux decline as the intrinsic photopeak efficiency of the detector decreases;
3) Observation times of hours to tens of hours are required to get good signal-to-noise ratio.

Table 3.8

GAMMA-RAY SPECTROMETER PERFORMANCE ORBITING MOON, MARS, AND MERCURY

Parameters	Gamma-Ray Energy (MeV)		
	1	3	10
a. Typical Source Flux from Radioisotopes or Major Elements (F_γ, photons/cm^2 sec)	.03	.03	.03
b. Background from Planetary Surface ($B_{\gamma s}$, photons/cm^2 sec 2 keV)	3.9^{-4}	9.0^{-5}	1.8^{-5}
c. Signal Count Rate (CR_S, counts/sec)	3.1^{-3}	2.1^{-3}	7.7^{-4}
d. Total Background in Photo Peak Observed by Detector (CR_B, counts/sec)	1.4^{-4}	1.3^{-5}	5.3^{-7}
e. Signal-to-Background	22	160	1500
f. Signal-to-Noise (S/N) as a Function of Observing Time for Each Resolution Element			
1 hour	3.3	2.7	1.7
10 hours	10	8.7	5.3
100 hours	33	27	17

The data in Table 3.9 are the result of applying the same methods using the surface fluxes which were actually predicted for major elements and which appeared in Tables 3.1 and 3.2. In addition we have determined the minimum detectable concentration of an element from the signal-flux given for lunar composition:

$$C_{min} = C_{lunar} \cdot 2 \div S/N \qquad (3.5)$$

where: C_{min} = minimum detectable concentration of elements,
C_{lun} = concentration in lunar surface (Apollo 11),
S/N = signal-to-noise computed for lunar surfaces.

The 2 in this equation denotes the significance of the measurement, i.e., 2σ. There are limitations in the applicability of this equation to situations where surface flux scales linearly with composition (discussed in Section 3.1). Furthermore, there are complications not explored further here of mutually overlapping gamma lines and uncertainties in the continuum. Nevertheless, the estimates provide a useful guide to element detection with this instrument.

The estimates of Table 3.9 include the Moon, and reflect certain differences expected at Mercury and Mars. The atmospheric attenuation at Mars will reduce the signal level. Most affected is the signal from elements with lines below 2 MeV. Enhanced solar cosmic-ray bombardment at Mercury will give rise to gamma-rays carrying very little compositional information which will interfere with observations of the galactic cosmic ray induced lines. Metzger (Ref. 3.14) has prepared a much more comprehensive evaluation of detection limits for a Mars gamma-ray spectrometer experiment. His data presented in Table 3.10 are generally consistent with the data of Table 3.9.

The final elements in determining gamma-ray spectroscopy capabilities at the Moon, Mars, and Mercury are the observing times and spatial resolution that is attainable with the baseline missions. Sensitivity will improve, in general, as the square root of the observing time. The near

Table 3.9

GAMMA-RAY ELEMENTAL ABUNDANCE DETERMINATIONS

(10 hour orbital observing time)

Element	Energy	Mode	Signal-to-Noise at Nominal Abundance			Elemental Sensitivity (C_{min})		
			Moon	Mars	Mercury	Moon	Mars	Mercury
^{40}K	1.46	Intrinsic	9.9	6.3	9.9	2.3^{-4}	3.6^{-4}	2.3^{-4}
Fe[1,2]	0.847	SCR[2]	4.6	1.2	12.	5.3^{-2}	2.0^{-1}	2.1^{-2}
	0.85	GCR_f	9.5	5.1	9.5	2.6^{-2}	4.8^{-2}	2.6^{-2}
	7.64	GCR_s[3]	5.0	6.8	5.0	4.9^{-2}	3.6^{-2}	4.9^{-2}
Ti[1,2]	1.312	SCR[2]	2.9	1.0	8.5	3.2^{-2}	9.2^{-2}	1.1^{-2}
	6.75	GCR_s[3]	5.6	7.6	5.6	1.6^{-2}	1.2^{-2}	1.6^{-2}

[1]All the signal-to-noise values and elemental sensitivities are reduced below lunar and mercurian values at Mars because of atmospheric attenuation of gamma-rays.

[2]The sensitivity data for SCR induced lines reflect the higher SCR fluxes at Mercury and the much smaller fluxes at Mars in comparison to the Moon.

[3]For Mars, those gamma fluxes induced by slow neutrons (GCR_s) are assumed to be enhanced by a factor of 3 due to water in the subsoil; fluxes induced by fast neutrons (GCR_f) are assumed to be identical to those for a lunar composition.

Table 3.10

GAMMA-RAY SPECTROMETER SENSITIVITY[1,2] FOR MARS

Element	Apollo 11 Basalt (Mean)	Uncollimated Sensitivity (3σ)		
		1 hour	10 hours	100 hours
Th PPM	2.1	1.5	0.5	0.15
U PPM	0.55	0.9	0.3	0.10
K %	0.12	0.11	0.03	0.011
Fe %	12	2.9	0.9	0.29
Ti %	5	1.2	0.4	0.12
Si %	20	11	3	1.1
O %	42	13	4	1.3
Al %	7.1	-	9	2.9
Mg %	4.6	-	4.0	1.2
Ca %	8.6	-	-	4.4
C %	(30)[3]	12	4	1.2
H %	(5)[3]	1.6	0.5	0.16
Na %	0.3	-	3	1.1
Mn %	0.2	-	0.7	0.23
Ni %	0.024	-	0.5	0.15
S %	0.10	-	3.0	1.0
Cl %	0.003	-	0.11	0.035
Lu PPM	2	-	-	17

[1]Taken from Ref. 3.12. These estimates may be rather optimistic for elements such as aluminum and magnesium where gamma emission from the spacecraft excited partly by cosmic rays and partly by the planetary neutron albedo will be received by the detector as well as emissions from these same elements on the planetary surfaces.

[2]Cr, Sr, Ba and Gd may also be detectable at the longer observing times.

[3]Projected polar cap concentrations for Mars.

polar circular orbits at the Moon and Mars are fairly simple to analyze in that the surface resolution is constant. The accumulated viewing time of a surface region, however, depends on location. While the orbit takes the instrument over the same polar regions every revolution, at the equator only certain longitudes are repeatedly observed. Consequently, better statistics and resolution can be obtained in polar regions if all other factors are equal. Table 3.11 gives the spatial resolution and observing time attainable at the equator and at the poles for the three bodies for a mission of 200 days duration. At the Moon the detector views an area about 65 km in diameter on the surface. As the spacecraft groundtrack is displaced 33 km at the equator each orbit, due to the lunar rotation, a particular longitude at the equator is observed on four passes over a lunar sidereal day. The polar regions, however, are observed each pass and accumulate about 80 times the observing time of an equatorial area per lunar sidereal day.

The situation is different at Mars in that the rapid rotation of the planet produces large offsets in the groundtrack from orbit to orbit. The baseline orbit has a period of one-tenth the rotation period of Mars and would repeat after one Mars day if there were no perturbations on the orbit. However, for the orbit selected the node shifts about 0.5°/day and consequently the swath viewed with the gamma-ray spectrometer is progressively displaced allowing the region between the initial groundtracks to be observed. If the mission lifetime is taken as one martian year, then the S/N indicated in Table 3.8(c) are found. Another orbit, without nodal motion, could have been selected permitting longer consecutive viewing, but it would suffer in total areal coverage over any specified period of time.

At Mercury, analysis of the instrument response is greatly complicated by the elliptical orbit. Near periapse of the orbit the spatial resolution is best; however, the viewing time is limited, while near apoapse the converse is true. Also, at altitudes above 5500 km the planet no longer fills the detector field of view and the instrument response begins to fall off with the inverse square of the distance from the planet. The viewing time and signal-to-noise are calculated at three points around

Table 3.11

SPATIAL RESOLUTION AND OBSERVING TIME[1] AS A FUNCTION OF LATITUDE ATTAINABLE FOR THE BASELINE ORBITERS OF MOON, MERCURY, AND MARS WITH A NOMINAL 200 DAY MISSION

Mission	Latitude			
	Equator		Pole	
	Resolution (km)	Time (hrs)	Resolution (km)	Time (hrs)
Baseline Lunar Orbit	65	.35	65	29
Baseline Mars Orbit	650	15	650	148
Baseline Mercury Orbit (periapse at pole)[2]	variable	41	600	13
Baseline Mercury Orbit (periapse at equator)	600	.28	variable	207

[1]Minimum detectable concentration of an element scales inversely as the square of the observing time. Minimum detectable concentrations for a few elements are shown for a 10-hour observation time of a resolution cell in Table 3.9 for Mars, Mercury and the Moon. Minimum detectable concentrations for a number of elements for Mars only are given in Table 3.10.

[2]Orbital perturbations could cause the viewing times of different locations to vary significantly.

the orbit--periapse, quadrature (true anomaly = 90°), and apoapse. Two orbit orientations are used, namely periapse at the pole and periapse at the equator. The resolution and observing time achievable with these two orientations are given in Table 3.11. In view of thermal problems associated with low-altitude orbiters near the equator, the polar periapse case may be most reasonable. At periapse the detector FOV covers an area about 600 km in diameter, while at apoapse the instrument sees the entire hemisphere of the planet. At the quadrature point the coverage is variable due to the changing altitude of the spacecraft, but an average value of the covered area is about 1200 km in diameter.

Low circular orbits are desirable for the gamma-ray experiment because of the greater spatial resolution they provide. Elemental detection from other orbits certainly appears feasible; however, a detailed mapping of elemental distribution over the surface is much more difficult from elliptical orbits.

Observations at the Galilean Satellites

The very unfavorable environmental conditions for operating a gamma-ray spectrometer in the Jovian system have already been referred to in Section 3.4. Although the signal fluxes from major elements are much higher at the Galilean satellites than they are at the Moon, Mars and Mercury, the background fluxes are even more increased (Table 3.12). We now examine in more detail the background fluxes which interfere with gamma-ray measurement in the Jovian system.

The prime source of background is the charged particle flux of the trapped radiation around the satellite. The typical gamma-ray spectrometer design for other missions consists of a detector with an active charged particle discriminator surrounding it. Charged particles intercepting the gamma-ray detector must also register in the shield, whereas gamma-ray events will not. Coincident events in the shield and gamma-ray detector are rejected as charged particle events. For this type of instrument at Io, the counting rates for a detector with an 18 cm^2 effective area would be 10^9 counts/sec while at Europa and Ganymede the count rates

Table 3.12

GAMMA-RAY SPECTROMETER PERFORMANCE ON GALILEAN SATELLITE NEAR-ENCOUNTER FLYBYS

Parameters	Satellites			
	Io	Europa	Ganymede	Callisto
a. Typical Source Flux from Major Elements (F_γ, photons/cm^2 sec)	2.0^{0}	2.0^{-1}	2.0^{-2}	2.0^{-2}
b. Typical Background Flux from the Satellite Surface ($B_{\gamma p}$, photons/cm^2 sec 2 keV)	4.0^{3}	1.0^{3}	1.0^{2}	1.5^{-4}
c. Total Estimated Gamma Flux from RTG and Spacecraft Bremsstrahlung at the Detectors ($B_{\gamma sp}$, photons/cm^2 sec 2 keV)	3.4^{2}	7.8^{1}	1.0^{1}	1.6^{-3}
d. Total Charged Particle[1] Count Rate (counts/sec)	1.09^{9}	5.0^{8}	5.0^{7}	3.0^{3}
e. Total Bremsstrahlung[1] Count Rate (counts/sec)	4.6^{4}	1.9^{4}	1.8^{4}	3.3^{-1}
f. Signal Count Rate[1] (counts/sec)	Note 2	Note 2	Note 2	2.0^{-3}
g. Total Background in Photopeak Observed by Detector	Note 2	Note 2	Note 2	5.0^{-5}
h. Signal-to-Background[1]	Note 2	Note 2	Note 2	1.0^{2}
i. Actual Observing Time (hours)	Note 2	Note 2	Note 2	5.0^{-1}
j. Signal-to-Noise[1]	Note 2	Note 2	Note 2	≈ 1

[1]For Io, Europa and Ganymede these count rates from both direct charged particle events and bremsstrahlung originating from the planet and the spacecraft are so high that the detector is simply unable to function quite apart from being able to discriminate between charged particles and gamma-rays. For this reason estimates of signal count rate, signal-to-background and signal-to-noise are quite meaningless for those objects. For Callisto the background problem is much less serious but the observing time from a hyperbolic encounter.

[2]These parameters are not pertinent at the charged particle count rates listed, as the detector is not operative.

would be greater than 10^7 counts/sec (Table 3.12). Electronic discrimination systems cannot tolerate these count rates. These anticoincidence techniques for charged particle rejection are limited to count rates of 10^6 c/sec in sodium iodide detectors and 10^5 c/sec in germanium detectors if those detectors are to retain high-energy resolution. With a plastic anticoincidence counter higher rise times can be established, and so the latter number may be improved to approach 10^6. The implication of this result is that the omnidirectional charged particle flux at the detector be kept below 5×10^4 c/sec with a detector area of 18 cm^2. Passive shielding is impractical for this due to the large mass requirement. These considerations alone would indicate that it is unlikely that a gamma-ray spectrometer would be useful for close flybys of Io, Europa, or Ganymede, although close flybys of Callisto would be less seriously affected by trapped radiation (Table 3.12-d).

Charged particles represent only a portion of the background to gamma-rays received from the satellite. Bremsstrahlung generated outside the detector either in the spacecraft bus or in the components of the shield are the other components. It is not possible to reject bremsstrahlung events entirely by anticoincidence methods, and attenuation by shielding is not very effective. For example, a shield of sodium iodide 5 cm thick only attenuates 3 MeV bremsstrahlung by 50%. Bremsstrahlung photons which are Compton scattered in the shield and then absorbed in the gamma detector can be rejected. Unfortunately, typical active collimator materials such as NaI and CsI have a slow decay component such that 20% of the photons produced are delayed by up to 10 μsec after the primary event.

A satisfactory shielding arrangement for a gamma-ray spectrometer involves a plastic outer passive shield instead of aluminum which yields fewer bremsstrahlung and an active inner shield for coincidence counting of electrons. The implications of these results are that near-encounter observations can only be conducted at Callisto; even the electron fluxes experienced at Ganymede are unacceptably high. However, the observing times for flybys of Callisto are far too short to permit elemental abundance determinations.

In summary, elemental abundance determinations are not possible with near-encounter gamma-ray spectroscopy from a Jupiter orbiter. For the inner satellites Io, Europa, and Ganymede, charged particle fluxes close down the detector. Even if it were possible to exclude charged particle events not possible with current technology and the only background source was the bremsstrahlung from the planet and the spacecraft the experiment would still be marginal if the estimates of bremsstrahlung are reasonable. For Callisto, the expected signals are so small that they could not be detected in a flyby.

A possible solution to the radiation background problem at the inner Jovian satellites is long range 'observatory-mode' observation. The effect of trapped radiation on the spacecraft can be minimized by conducting observations of the satellites from locations outside the regions of most intense radiation flux. High-inclination orbits are most suitable for these observations since radiation intensity decreases with increasing Jovian magnetic latitude (Refs. 2.4-2.10). However, any Jupiter orbiter has to pass through the magnetic equator with its intense charged particle fluxes for some part of its orbit and radioactivity induced during those passages will remain an important and difficult to calibrate source of background for any observations from high magnetic latitudes.

In the observatory mode (Table 3.13) the charged particle and bremsstrahlung fluxes are no longer so large that they close down the detector. However, the signal fluxes from the satellites fall to very low levels and extremely long observing times are needed to detect satellite signals. Moreover, the data in Table 3.13 do not completely reflect the problems of observing gamma-rays from the satellites. They do not show, for example, that the spacecraft will emit line spectra as well as the satellites which would seriously interfere with the recognition of elemental lines from the satellite surfaces. Nor do they properly take account of the radiation damage sustained by the detector or the effects of the time varying background of induced radiation generated within the spacecraft which must pass through the radiation belt during some part of its orbit. For all these reasons we conclude that observatory mode gamma-ray spectroscopy of the Galilean satellites is also impractical.

Table 3.13

GAMMA-RAY SPECTROMETER PERFORMANCE
OF GALILEAN SATELLITES IN OBSERVATORY MODE

	Satellites			
	Io	Europa	Ganymede	Callisto
a. Typical Source Flux from Major Elements (F_γ, photons/cm^2 sec)	2.0^{0}	2.0^{-1}	2.0^{-2}	2.0^{-2}
b. Typical Background Flux from the Satellite Surface ($B_{\gamma p}$, photons/cm^2 sec 2 keV)	4.0^{3}	1.0^{3}	1.5^{2}	1.5^{-4}
c. Total Estimated Gamma Flux from RTG and Spacecraft Bremsstrahlung at the Detectors ($B_{\gamma sp}$, photons/cm^2 sec 2 keV)	2.4^{2}	5.4^{1}	6.0^{0}	1.6^{-3}
d. Total Charged Particle Count Rate (counts/sec)	4.0^{7}	1.9^{7}	1.1^{-6}	3.0^{3}
e. Total Bremsstrahlung Count Rate[2] (counts/sec)	4.3^{3}	9.7^{2}	1.1^{2}	2.9^{-2}
f. Signal Count Rate[2] (counts/sec)	1.3^{-4}	3.6^{-6}	4.1^{-7}	1.2^{-7}

[1]The estimates of background here do not adequately reflect the severe difficulties of conducting a gamma-ray experiment in the Jovian system; see text.

[2]The extremely low signal count rates preclude any meaningful measurement at these satellites.

3.6 Gamma-Ray Experiment Summary

Gamma-ray spectroscopy appears to be an attractive approach to the remote sensing studies of the Moon, Mars, and Mercury. It may also be useful in the study of the asteroids if observations of sufficient duration can be accomplished. Instruments for observing Mars and Mercury can be rather similar to those designed for the Moon although the problems of cooling a Mercury spectrometer may involve major design changes.

A gamma-ray spectrometer designed for the Moon, Mars, and Mercury could not be effectively used for the reconnaissance of the three inner Galilean satellites because of the radiation background. It seems highly unlikely that any gamma-ray spectrometer could be designed using current technology to perform remote sensing observations in this hostile environment. More fundamentally, the flux of continuum bremsstrahlung radiation emitted by the satellite is large compared to the flux in discrete lines which carry the chemical information.

Observations of Callisto are possible with a gamma-ray spectrometer but it will be necessary to place a spacecraft in orbit around that satellite to achieve observation times adequate for elemental abundance determination.

REFERENCES

3.1 Metzger, A. E., et al., "Lunar Surface Radioactivity: Preliminary Results of the Apollo 15 and Apollo 16 Gamma-Ray Spectrometer Experiments," Science, Vol. 179, p. 800, 1973.

3.2 Metzger, A. E. and J. R. Arnold, "Gamma-Ray Spectroscopic Measurements of Mars," Applied Optics, Vol. 9, p. 1289, 1970.

3.3 Reedy, R. C., J. R. Arnold and J. I. Trombka, "Expected Gamma-Ray Emission Spectra from the Lunar Surface as a Function of Chemical Composition," J. Geophys. Res., Vol. 78, 1973.

3.4 Armstrong, T. W. and R. G. Alsmiller, Jr., "An Estimate of the Prompt Photon Spectrum Arising from Cosmic-Ray Bombardment of the Moon," Astronaut. Acta., Vol. 14, p. 143, 1969.

3.5 Armstrong, T. W., "Calculation of the Lunar Photon Albedo from Galactic and Solar Proton Bombardment," J. Geophys. Res., p. 524, 1972.

3.6 Shreve, D. C. and D. H. Rester, "Electron Transport and Space Shielding Handbook, " NASACR, Science Applications Report No. SAI-71-559-LJ, November 1971.

3.7 Dance, W. E. and D. H. Rester, "Electron Bremsstrahlung Produced Thick Targets at Incident Electron Energies of 0.2, 1.0, 2.0, and 2.8 MeV," LTV Report No. 0-7100-8R-2, February 1968.

3.8 Jupiter, C. P., J. A. Lonergan and G. Merkel, "An Experimental Study of the Transport of Electrons Through Thick Targets," in NASA SP-169, p. 249, 1967.

3.9 Schiff, L. I., Phys. Rev., Vol. 70, p. 87, 1946.

3.10 Hansen, N., et al., "Bremsstrahlung Production in Thin and Thick Targets," Lawrence Radiation Laboratory Report, March 1959.

3.11 Hall, C. F., "Pioneer 10/11 Spacecraft and Missions to Jupiter," as quoted in R. Kloster, "The Impact of Jupiter's Trapped Radiation on Probe Missions," AIAA Paper No. 75-163, presented at AIAA/AGU Conference on the Exploration of the Outer Planets, St. Louis, Missouri, September 1975.

3.12 Dyer, C. S., et al., "Radioactivity Observed in the Sodium Iodide Gamma-Ray Spectrometer Returned on the Apollo 17 Mission," Space Science Instrum., Vol. I, p. 279, 1975.

3.13 Metzger, A. E., et al., "Gamma-Ray Spectrometer Experiment, Apollo 15, Preliminary Science Report," NASA SP-289, 1971.

3.14 "Mars Polar Orbiter Study," JPL Report 760-118, October 1974.

4. X-RAY FLUORESCENCE SPECTROSCOPY

X-ray fluorescence experiments offer a powerful tool in determining the elemental composition of a substance. Under proper stimulation all elements will emit x-rays whose energies are characteristic of the particular element. Measurements of these x-rays can be used to determine the abundances of the elements in an unknown material. Under laboratory conditions parts per million can be routinely measured.

Characteristic x-rays are emitted from an atom when its innermost (K) electrons are removed by ionization. The removal of the innermost electrons can be accomplished by x-rays, electrons or protons with energies greater than the binding energy of the K electrons. The excitation mechanism and cross sections are different for these incident radiations. For missions to the Moon or Mercury the x-rays from the solar spectrum are the major excitation mechanism. For the Jovian satellites, proton and electron bombardment can be the dominant excitation mechanisms.

X-ray fluorescence experiments have been successfully carried out in the Apollo program. These experiments employed large area proportional counters to measure the characteristic x-rays from Mg, Al and Si from the lunar surface. The window thicknesses of the proportional counters limited the measurements to x-rays with energies greater than about 1 keV. The solar x-ray spectrum which stimulates x-ray emission from the Moon, falls off rapidly with increasing energy, thus limiting the measurement of higher energy x-rays.

This section will discuss the potential of x-ray fluorescence experiments in missions to Mercury and the Jovian satellites. Atmospheric attenuation renders impractical remote sensing x-ray fluorescence studies of Mars, Venus and Titan. Estimates will be made of the x-ray source strengths for excitation by solar x-rays, energetic electrons, and protons. The potential and possible limitations of the technique will be discussed.

4.1 Characteristic X-Ray Source Strengths at Moon and Mercury

The primary mechanism for characteristic x-ray emission at the Moon and Mercury is excitation by solar x-rays. The short wavelength component of the solar spectrum decreases rapidly with decreasing wavelength (increasing photon energy) and is very sensitive to solar activity. Table 4.1 gives the flux of solar x-rays at the Earth for quiet sun conditions. Variations of three orders of magnitude can occur at these wavelengths during periods of solar activity. Also listed in Table 4.1 is the range of elements that can be stimulated to emit K x-rays in each energy interval and the energies of their K absorption edges.

The cross sections for characteristic x-ray stimulation are sensitive functions of atomic number and incident photon energy. Yields of characteristic x-rays for the various elements may be calculated by integration of the solar x-ray spectrum with the appropriate energy dependent excitation cross section. If we assume that the cross section for ionization depends on the energy of the photons and Z of the target material as (Ref. 4.2), i.e.,

$$\sigma \propto \frac{Z^4}{E^3} \tag{4.1}$$

and that the solar x-ray spectrum drops approximately as a parameterization of the data of Table 4.1, then

$$I(E) \simeq 1.3 \times 10^8 \, e^{-E/0.35}, \text{ photons/keV}\cdot\text{cm}^2 \text{ sec} \tag{4.2}$$

where E is in keV, and one obtains for the x-ray production

$$Y(Z) \propto \int_{E_{K(Z)}}^{\infty} \frac{Z^4 e^{-E/0.35}}{E^3} \, dE, \text{ photons/cm}^2 \text{ sec} \tag{4.3}$$

where $E_{K(Z)}$ is the energy of the K edge for the element of interest and Y(Z) is the x-ray photon flux for element Z. This equation can be

Table 4.1

SOLAR X-RAYS, QUIET SUN CONDITIONS[1]
AND K ABSORPTION ENERGIES[2]

E (keV)	Photons/cm^2 sec	Kab (keV)
0.30 → 0.40	1.5^{8}	N (0.399)
0.40 → 0.54	5.0^{6}	O (0.531)
0.54 → 0.83	3.0^{6}	F (0.687)
0.83 → 1.24	5.0^{5}	Ne (0.874), Na (1.080)
1.24 → 2.48	1.5^{5}	Mg (1.30) to S (2.470)
2.48 → 4.14	2.0^{3}	Cl (2.819) to Ca (4.038)
4.14 → 12.4	1.0^{1}	Sc (4.496) to As (11.863)

[1]From Ref. 4.1.

[2]The solar x-ray spectrum contains considerable line structure which is not reflected in this tabulation and which affects the actual emission of characteristic radiation from planetary surfaces. Variations in the flux during periods of solar activity include increases at all energies and hardening of the spectrum.

integrated to give the yield as

$$Y(Z) \propto \frac{Z^4}{[E_K(Z)]^2} \; I_3 \; [E_K(Z)/0.35], \text{ photons/cm}^2 \text{ sec} \qquad (4.4)$$

where I_3 is the exponential integral of the third kind (Ref. 4.3). The proportionality constant may be evaluated from the thick target yield of K x-rays in Mg stimulated by K x-rays from Al as 6.9×10^{-4} photons/steradian-photon (Ref. 4.4). The x-ray flux due to different elements may be written as

$$Y(Z) = \frac{13 \; Z^4}{[E_K(Z)]^2} \; I_3 \; [E_K(Z)/0.35], \text{ photons/cm}^2 \cdot \text{sec} \cdot \text{sr} \; . \qquad (4.5)$$

The evaluation of the x-ray yield described above is only approximate in that it ignores the discontinuities in the cross section at the absorption edges and the fact that the constant of proportionality is somewhat different on different sides of the absorption edge.

The fact that the solar flux of x-rays scales with distance from the sun as R^{-2} implies that the solar flux for Mercury will, on the average, be 7 times that at the Moon. The large orbital eccentricity of Mercury causes a variation of over a factor of 2 in solar flux over the orbital period; this variation, coupled with the 3:2 synchronism of the rotational and orbital periods, implies that the stimulating flux at hot pole longitudes will be over twice that of warm pole longitudes. Table 4.2 lists the approximate yields of characteristic x-rays for several elements at the Moon and Mercury. The normalized yields listed are the yields Y(Z) calculated as described above and we have also computed predicted yields for an Apollo 11 composition (see Section 2) at the Moon and Mercury. We have compared the predictions for aluminum, magnesium and silicon at the Moon with predictions made by a much more exact method (Ref. 4.5) and with data from the Apollo 15 and 16 missions (Ref. 4.6) and we find agreement within about 50% in absolute flux and 20% in the flux ratios between elements. It is important to note here that the surface fluxes are time variable because the absolute intensity and the hardness of the solar x-ray spectrum are time variable.

Table 4.2

APPROXIMATE YIELDS OF K X-RAYS FROM VARIOUS ELEMENTS DUE TO SOLAR X-RAY STIMULATION[1]

Element	Z	E_k (keV)	X-Ray Yields (photons/cm^2-sec-sr)			
			Normalized Yields		Predicted Yields (All)	
			Moon	Mercury	Moon	Mercury
Na	11	1.080	1.4^{3}	9.6^{3}	4.8	3.2^{1}
Mg	12	1.303	8.0^{2}	5.3^{3}	3.7^{1}	2.4^{2}
Al	13	1.559	2.0^{2}	1.3^{3}	1.0^{1}	6.6^{1}
Si	14	1.838	1.0^{2}	6.6^{2}	1.6^{1}	1.1^{2}
Ca	20	4.038	3.9^{-1}	2.6^{0}	1.9^{-2}	1.3^{-1}
Ti	22	4.962	5.0^{-3}	3.3^{-2}	1.5^{-4}	1.0^{-3}
Fe	26	7.111	1.0^{-5}	6.6^{-5}	6.0^{-7}	4.0^{-6}

[1]Normalized yields and yields predicted for an Apollo 11 composition are included. These fluxes will be significantly different during periods of solar activity.

4.2 Characteristic X-Ray Source Strength of the Galilean Satellites

Due to the great distance of the Galilean satellites from the Sun, the flux of fluorescent x-rays excited by solar radiation is very much smaller than at the Moon and Mercury. However, energetic electrons and protons from the Jovian radiation belts which impact the surfaces of the Galilean satellites will excite characteristic x-rays. We now make some estimates of the electron-excited source fluxes.

The yield of K x-rays from a thick target depends on the energy of the incident electron and the atomic number of the target. Figure 4.1 shows the yields of K x-rays produced in thick targets as a function of incident electron energy (Ref. 4.7). The yield is seen to increase for increasing electron energy to a maximum at an electron energy (T) given as

$$T = 3 \times 10^{-3} Z + 9.2 \times 10^{-6} Z^3, \text{ MeV}. \qquad (4.6)$$

After the maximum the yield is seen to decrease slowly for the lighter elements. Figure 4.2 shows the thick target yield of a K x-ray as a function of Z at 3 MeV. A reasonable parameterization of this curve is

$$Y(Z) = 1.3 \times 10^{-4} \left(\frac{Z}{10}\right) 2.26, \text{ K-photons/sr}\cdot\overline{e^-} \qquad (4.7)$$

If one assumes that the yield as a function of electron energy is a constant over the incident electron energy range 0.1 to 30 MeV given by the expression above, then an approximation for the K x-ray yield from trapped electron bombardment would be:

$$J = \frac{\phi}{4} \; 1.3 \times 10^{-4} \cdot \frac{Z}{10} \cdot 2.26, \text{ K-photons/cm}^2\cdot\text{sr}\cdot\text{sec}, \qquad (4.8)$$

where ϕ is the omnidirectional flux of electrons with energies greater than 0.1 MeV. The K x-ray fluxes due to trapped electron bombardment listed in Table 4.3 are found from the above relation and the electron fluxes of Table 2.3. The values given are for a magnetic latitude of zero and can be expected to decrease as the satellites move with respect to the geomagnetic equator.

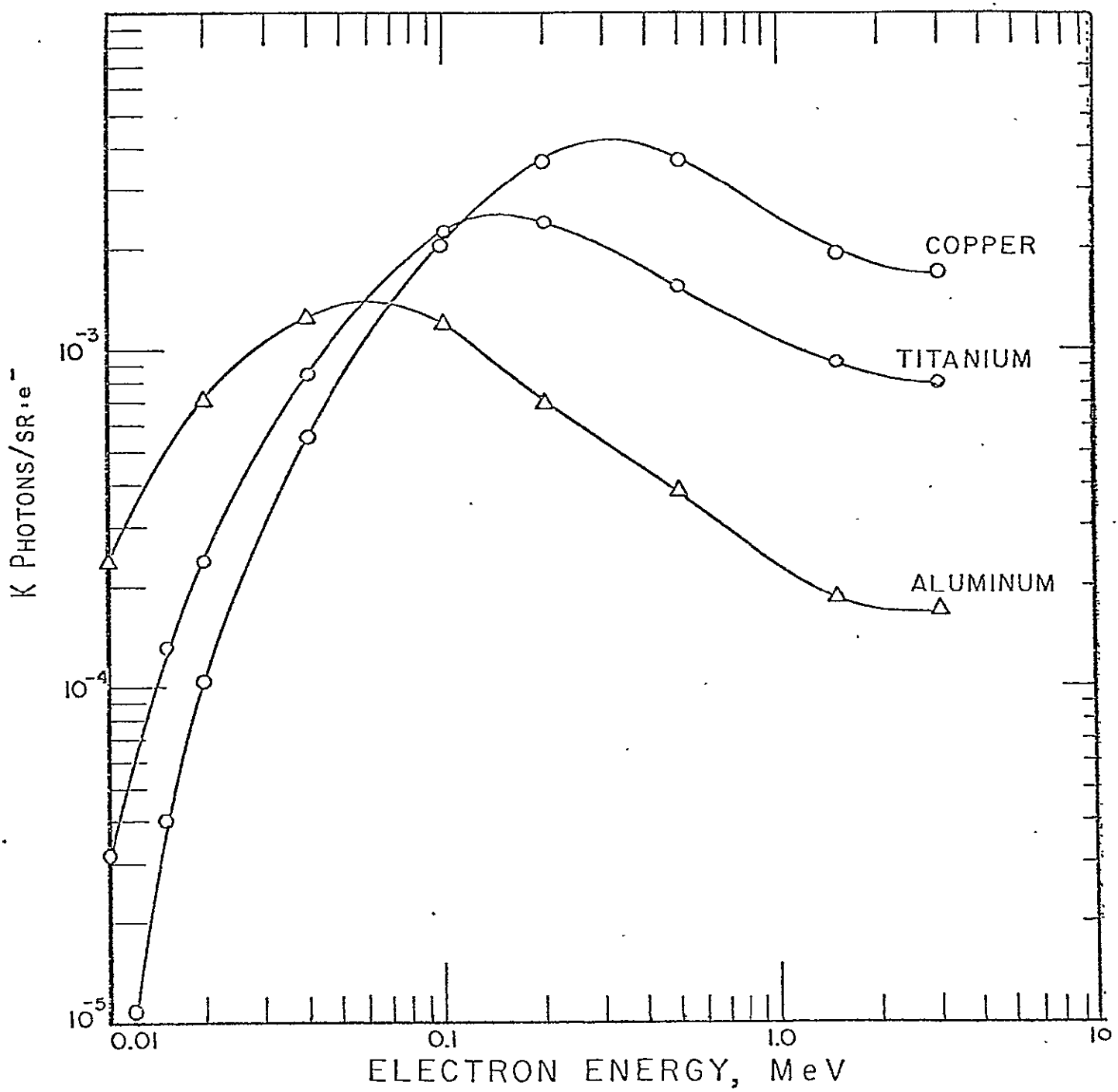

Figure 4.1 Thick Target Electron Induced K X-Ray Yields as a Function of Incident Electron Energy for Al, Ti and Cu. (From Ref. 4.5).

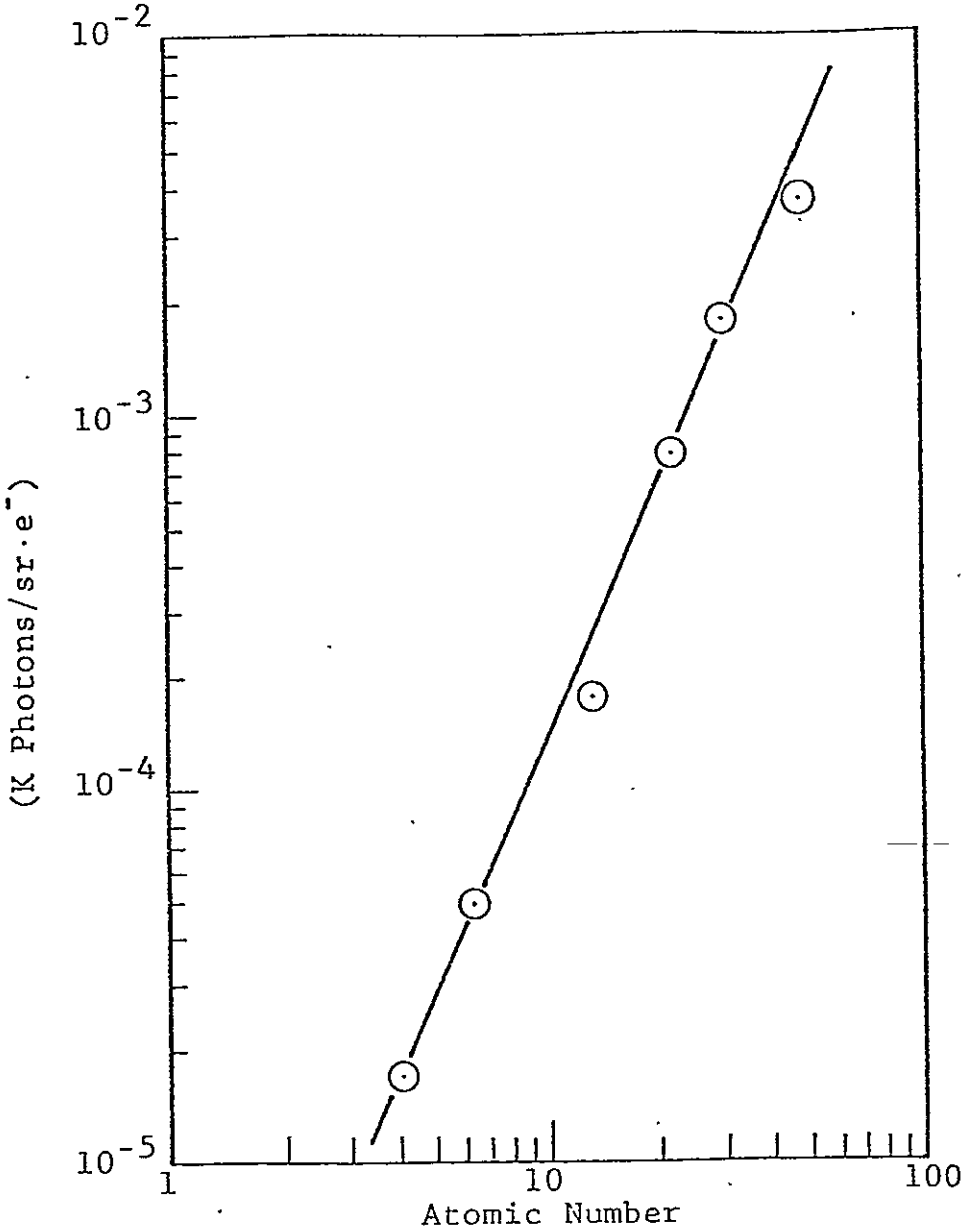

Figure 4.2 Yield of Electron Induced K X-Rays as a Function of Z for 3 MeV Incident Electrons.

Table 4.3

ESTIMATED K X-RAY YIELDS[1] AND BREMSSTRAHLUNG BACKGROUND
DUE TO TRAPPED ELECTRON AND PROTON BOMBARDMENT OF THE GALILEAN SATELLITES

Element	K Energy (keV)	Galilean Satellites											
		Io			Europa			Ganymede			Callisto		
		Electrons	Protons	Total[2]	Electrons	Protons	Total	Electrons	Protons[4]	Total	Electrons	Protons	Total
Na	1.080	8.1 ^{3}	6.9 ^{1}	8.2 ^{3}	4.0 ^{3}	4.4 ^{2}	4.4 ^{3}	3.6 ^{3}	-	3.6 ^{3}	2.0 ^{1}	-	7.3
Mg	1.303	1.0 ^{4}	5.7 ^{1}	1.0 ^{4}	4.9 ^{3}	3.0 ^{2}	5.2 ^{3}	4.4 ^{3}	-	4.4 ^{3}	2.5 ^{1}	-	5.5
Al	1.559	1.2 ^{4}	4.8 ^{1}	1.2 ^{4}	5.9 ^{3}	2.1 ^{2}	6.1 ^{3}	5.3 ^{3}	-	5.3 ^{3}	2.9 ^{1}	-	3.6
Si	1.838	1.4 ^{4}	4.1 ^{1}	1.4 ^{4}	7.0 ^{3}	1.5 ^{2}	7.2 ^{3}	6.3 ^{3}	-	6.3 ^{3}	3.5 ^{1}	-	3.9
Ca	4.038	3.1 ^{4}	2.0 ^{1}	3.1 ^{4}	1.6 ^{4}	3.1 ^{1}	1.6 ^{4}	1.4 ^{4}	-	1.4 ^{4}	7.8 ^{1}	-	7.8
Ti	4.962	3.7 ^{4}	1.8 ^{1}	3.7 ^{4}	2.0	2.7 ^{1}	2.0 ^{4}	1.7 ^{4}	-	1.7 ^{4}	9.5 ^{1}	-	9.5
Fe	7.111	5.6 ^{4}	1.2 ^{1}	5.6 ^{4}	2.8 ^{4}	1.0 ^{1}	2.8 ^{4}	2.5 ^{4}	-	2.5 ^{4}	1.4 ^{2}	-	1.4
Back-ground[3]	1.500	7.0 ^{2}	-	7.0 ^{2}	2.0 ^{2}	-	2.0 ^{2}	2.0 ^{0}	-	2.0 ^{0}	-	-	-

[1]The normalized yields must be multiplied by the relative abundance of the element to obtain absolute values.

[2]The total signal fluxes include fluorescent x-rays induced by solar x-ray excitation. The contribution is negligible except at Callisto. The totals listed here will somewhat underestimate the actual signal fluxes because characteristic x-rays excited by bremsstrahlung (see Note 3) have not been included.

[3]The background flux from the satellite surfaces is bremsstrahlung from the electron bombardment. The fluxes are given as photons/cm^2 sec sr/keV at 1.5 keV.

[4]The proton induced signal fluxes for Ganymede have not been computed as no relevant proton data are available. These fluxes are probably down by three orders of magnitude relative to Europa.

Bombardment by high-energy protons and other heavy charged particles will also cause the production of characteristic x-rays. Unlike x-ray and electron stimulation, protons have much larger K x-ray yields for low Z elements than high Z elements. Figure 4.3 shows the thick target yields of K x-rays from Fe to Ta as functions of the incident proton energy (Ref. 4.8). The yields are seen to be rapidly increasing functions of incident proton energy and decreasing atomic number.

Cross section data obtained using thin targets and high-energy protons are shown in Figure 4.4 for Ca (Z = 20) and Ti (Z = 22). The cross sections are seen to increase with increasing energy up to a maximum at between 10 and 20 MeV for these elements. The cross section decreases slightly past these maxima. The peak yield of K x-rays, which depends on both the ionization cross section (decreasing function of Z) and the K-shell fluorescence efficiency (increasing function of Z), are fairly constant over the range of Z between 20 and 29 (Ref. 4.10). We will approximate the proton induced K x-ray yield above the peak as being independent of proton energy with a peak value of 1.4×10^{-3} photons/proton (extrapolated from the data of Figures 4.3 and 4.4). We will also assume that only protons with energies greater than one-half the energy of the peak will contribute to the x-ray production. Parameterizing the peak energies of Figure 4.4 gives a peak energy of

$$E_p \simeq 7.8 \left[\frac{Z}{20}\right] 2.25, \text{ MeV.} \qquad (4.9)$$

In this approximation, the production rate of K x-rays due to proton bombardment is

$$Y_p(Z) \simeq \frac{1.4 \times 10^{-3}}{4\pi} \frac{\phi_p}{4}, \text{ photons/proton·sr,} \qquad (4.10)$$

where ϕ_p is the omnidirectional flux of protons with energies greater than $12/E_p$. There are a few data for the flux of protons with low energies in the radiation belts of Jupiter. The data listed in Table 4.3 were combined with data of Ref. 4.9 to give a rough estimate of the integral omnidirectional proton flux spectrum (Figure 4.5). The data reported for the

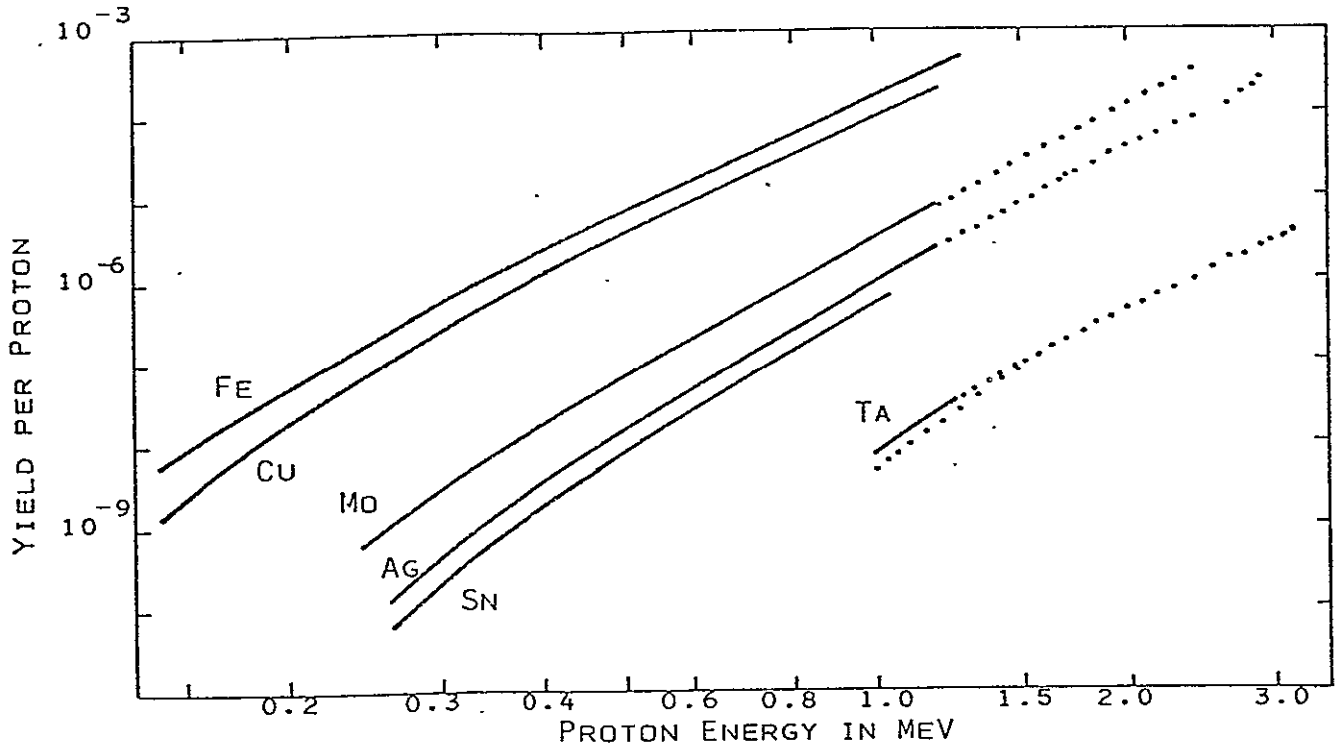

Figure 4.3 Thick Target Yield of K-Shell X-Rays as a Function of Initial Proton Energy. (From Ref. 4.6).

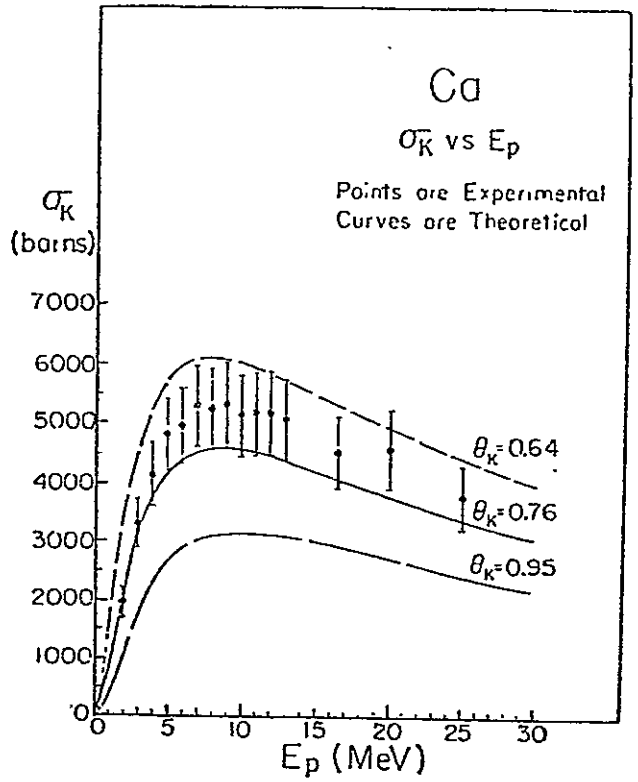

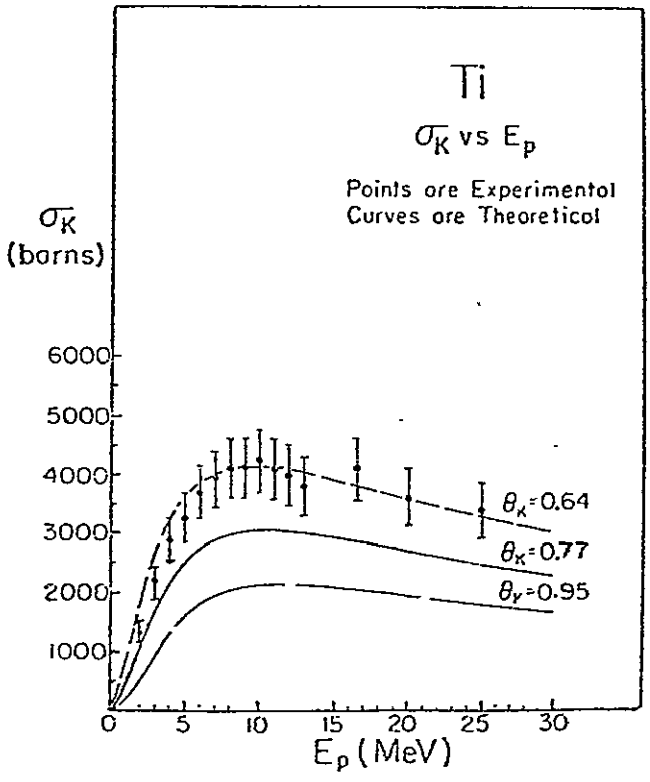

Figure 4.4 Absolute K-Shell Ionization Cross Section (σ_K) for Protons on Ca and Ti Compared to Theory. (From Ref. 4.7).

Pioneer 10 flight had many of the low-energy proton sensors in saturation over the region of the satellites while the trajectory for Pioneer 11 was out of the geomagnetic equatorial plane (Refs. 4.11 and 4.12). Table 4.3 also lists the estimated proton induced x-ray fluorescence rates for the satellites based on the above model. It should be emphasized that these are order of magnitude estimates only. The electron and proton data in Table 4.3 indicate that for all of the Jovian satellites the electron induced x-ray production should dominate. The tables also indicate that the source strengths will be large compared with that observed on the Moon by Apollos 15 and 16.

The preceding discussion of the characteristic x-ray sources made no mention of the angular distribution of the incident radiation. For the solar x-ray case this will be a factor since the irradiance of x-rays of the surface will change with latitude. For the electron and proton bombardments the angle of incidence should not be an important factor although the observation angles will be due to absorption of the outgoing x-rays.

4.3 Background Sources for Observations of Moon and Mercury

Background levels measured on the dark side of the Moon during the Apollo 15 and 16 x-ray fluorescence experiment were quite low and constant. The data could be corrected by simply subtracting the background levels. Charged particle and gamma-ray events may be effectively suppressed through pulse shape discrimination. Coherent scattering of solar x-rays provides another source of background. At the Moon, scattering was significant only for relatively low energies (< 1.4 keV); even at the low energies the scattered background was only ≈ 10% of the source signal. At higher energies, with the high Al and Si concentrations in the lunar surface, most of the solar x-rays produce photoionization.

Background levels at Mercury are assumed to be similar to those at the Moon; however, Mercury does have a background environment not found near the Moon, namely sporadic bursts of protons and electrons. These particle fluxes, measured by Mariner 10 to be greater than 10^4 cm^{-2} sec^{-1}

for protons with energies ≈ 300 keV, are apparently impulsively accelerated solar wind particles with the acceleration source within some 6.5 Mercury radii of the planet (Ref. 4.13). The proportional counters saturate at fluxes somewhat less than 10^5 counts/sec; which typically last for a few seconds; hence, the large electron fluxes could saturate the detectors during these periods. The Mariner 10 first encounter measured two such events in about 30 minutes. This was during the quiet phase of solar activity; conceivably the particle flux would be substantially higher during active sun periods.

4.4 Background Sources for Observations in the Jovian System

At the Jovian satellites the background sources will be due to both low energy bremsstrahlung produced at the satellite surface by trapped electrons, and charged particles entering the detector through apertures. The first source of background will be independent of detector shielding or configurations. The second will depend strongly on the detector design and shielding.

The bremsstrahlung background for x-rays is calculated in the same manner as was used to find the gamma-ray bremsstrahlung background flux (Section 3.4). Figure 4.5 shows an estimate of the low-energy bremsstrahlung intensity (photon number times energy) as a function of incident electron energy. The data sources used for Figure 3.3 were also used to generate the above figure. Attenuation of the bremsstrahlung photons was approximated by assuming that the low energy photons are created uniformly throughout the surface region and that attenuation coefficients for 10 keV photons in Al could be used.

To obtain an estimate of the background one must know the resolution of the detection system since the characteristic x-rays are line sources and the bremsstrahlung background is continuous. Proportional counters typically have energy resolutions that vary as the inverse square root of the energy with a resolution of 12 to 15% at Fe x-ray energies (Ref. 4.14). Because of the poor energy resolution of the proportional counter at low

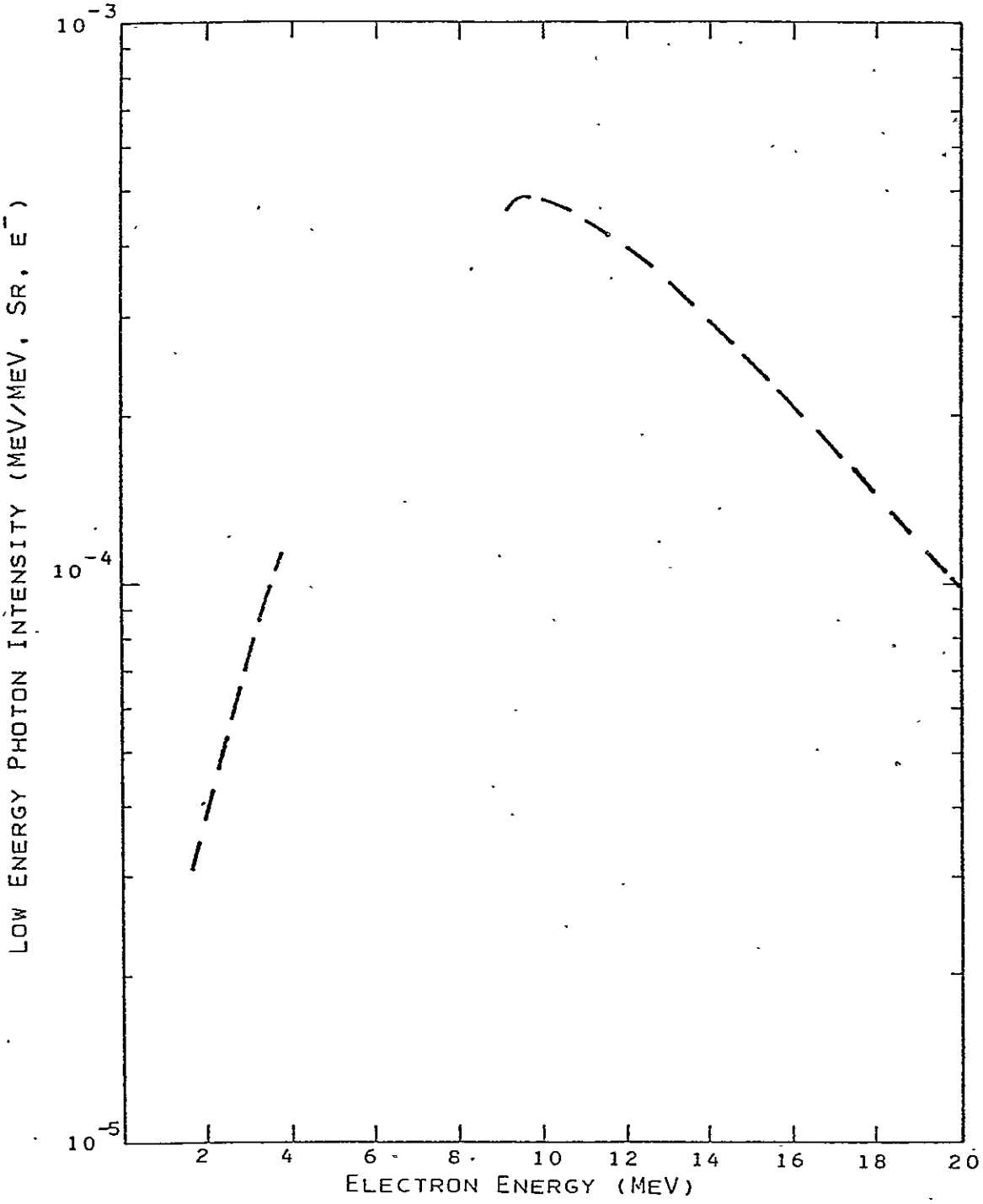

Figure 4.5 Estimated Low Energy Bremsstrahlung Intensity in the Backward Hemisphere as a Function of Incident Electron Energy.

energies Al and Mg filters are planned for the LPO instrument to discriminate between the elements Mg, Al and Si although pulse height analysis will be used at the higher energies. Recent developments in gas scintillation proportional counters have achieved resolutions of 8.5% (Ref. 4.15). Solid state detectors (Refs. 4.16 and 4.17) have achieved resolutions of better than 200 eV (5% at 4 keV) while dispersive crystal spectrographs achieve resolutions of about 1% although their absolute efficiencies are very low.

We will assume for a space system that an energy resolution of 10% at Fe is obtainable. The intensity curve of Figure 4.5 (photon number × energy/energy/sr/electron) can immediately be converted to photons per energy increment per steradian per incoming electron by multiplying by the relative detector resolution. Integrating this production rate with the differential electron energy spectrum gives the total background under the peak. The integrations were estimated using the parameterized electron flux spectrum. The results of this calculation of bremsstrahlung background are tabulated in Table 4.3 with the total K x-ray yields for the Galilean satellites.

While the estimated results presented above are fairly crude and the models on which they are based are extrapolations which in many cases could be subject to large errors, the results do indicate that the x-ray signals for the main surface components should be larger than the bremsstrahlung background. The observation of minor surface elements might even be possible but more rigorous calculations should be performed to confirm this. For the electron and proton induced x-ray stimulation there are theoretical models. For the bremsstrahlung background there are a number of computer codes which could be employed.

4.5 Experiment Performance Calculations

An assessment of the performance of remote sensing x-ray spectroscopy for elemental abundance determination can be made on the basis of signal and background intensities discussed above. The procedures used for making these assessments are approximate and are intended to give order of magnitude estimates only. The purpose is to determine experiment feasibility and to provide guidance for new orbit or spacecraft design concepts. A solar x-ray monitor to measure the intensity and shape of the incident solar flux is assumed to be an integral part of the measurements for the Moon and Mercury. A calibration sample excited into emission by x-rays from the Sun would also be desirable. Calibration for Galilean satellite observations presents some special problems discussed further below.

For the Moon and Mercury the performance estimates are made for continuous observation from spacecraft in the 'baseline' orbits. For the Galilean satellites, calculations are made for satellite encounters and for long-range 'observatory-mode' observations conducted from outside the trapped radiation belts.

Baseline X-Ray Fluorescence Spectrometers

Two instrument configurations can be contemplated for a planetary fluorescence x-ray spectrometer. They are a large area collimated proportional counter (Table 4.4) and an x-ray glancing incidence telescope (Table 4.5).

For orbital or near-encounter observations and for far-encounter observations where trapped radiation background is insignificant, then a large area proportional counter is the simplest approach to x-ray fluoroscopy. For observations in a trapped radiation environment, a focusing x-ray telescope has some definite advantages, i.e., it allows operation at much longer ranges and permits operation with smaller detectors which offer a smaller cross section to trapped radiation. With a fairly compact telescope design (Table 4.5) collection areas of 15 cm^2 can be achieved concentrating the radiation onto a few square millimeters.

Table 4.4

CHARACTERISTICS OF A LARGE AREA FLUORESCENCE X-RAY DETECTOR

Fore-Optics:	Single mechanical collimator assembly
Field-of-View:	60°
Filters:	Metal foils
Detector:	Proportional counters, each having an effective window area of approximately 25 cm^2. The window consists of 0.0025 cm thick beryllium. The counters are filled with standard P-10 gas at 1 atm.
Energy Range:	1 to 10 keV
Energy Resolution:	12 to 15% at Fe
Background Suppression:	10^{-3}, using anticoincidence (guard) counting and pulse height discrimination
Data Handling:	Preamplifier outputs are sorted into 256 levels for transfer to spacecraft telemetry
Data Rate:	High rate -- 300 bps when spectrum read every 10 sec Low rate -- 1 bps when spectrum read every hour
Mass:	10 kg
Power:	4 w

Table 4.5

CHARACTERISTICS OF AN X-RAY TELESCOPE
FOR DETECTING FLUORESCENCE EMISSION

Telescope[1]:	Paraboloid-hyperboloid in Wolder Type 1 configuration
	Diameter 10 cm
	Focal Length 70 cm
	Collecting Area 15 cm^2
Field of View:	One degree
Mirror:	Gold coated replica
Detector[2]:	Surface barrier silicon device, passively cooled to 80°K
Energy Range:	1/2 to 10 keV
Energy Resolution:	3% FWHM at 6 keV
Spatial Resolution:	2 mrad
Noise per Resolution Element:	10^{-3} count/sec
Data Handling and Rate:	Same as in Table 4.6
Mass:	TBD
Power:	TBD

[1]The design adopted here is a one-third scale model of S-054 x-ray telescope flown on NASA Apollo Telescope Mount. As discussed further in the text, a conical focusing crystal spectrometer (Ref. 4.20) may be a better choice of instrument for observations of the Galilean satellites.

[2]Solid state detectors of this type are described in Refs. 4.16 and 4.17.

Performance Estimates for the Moon and Mercury

Predicted x-ray fluorescence fluxes for observation of aluminum, silicon and magnesium with the large area proportional counter are presented in Table 4.6. At the Moon, significant statistics for determining abundance ratios to reasonable accuracy can be obtained in ten seconds. For Mercury, because of the more intense solar flux, even shorter times are required. Furthermore, it may be possible to extend sensitivity to detect higher Z elements such as titanium and calcium. The charged particle flux at Mercury (Ref. 4.13) would produce K x-rays in the surface layer. Preliminary calculations of the x-ray flux based on Mariner 10 charged particle flux measurements indicate that the yield is quite small compared with the solar x-ray induced flux. Further studies of the effect of the charged particle flux on both the source signal and bremsstrahlung background should be included in detailed assessments of the Mercury orbital x-ray fluorescence experiment.

Performance Estimates for Galilean Satellites

Predicted performance x-ray fluorescence fluxes for aluminum have been computed for an Apollo 11 composition at the locations of the Galilean satellites. Signal-to-noise ratios for observations of these abundances, given the satellite bremsstrahlung background, trapped radiation interference, and RTG background, are given in Table 4.7 for the collimated instrument and in Table 4.8 for the focusing instrument for the observatory mode. Proportional counter detectors are adopted in both cases.

Aluminum occurs in larger abundances in basalts such as Apollo 11 than it does in either carbonaceous chondrites or evaporite which are the nominal compositions for the Galilean satellites assumed here. The performance estimates suggest that aluminum can be detected with a focusing instrument quite easily but that the determinations with a collimated instrument are quite marginal due to the high background. Furthermore, the background charged particle count rates for the collimated instrument

Table 4.6

PERFORMANCE[1] OF NON-FOCUSING X-RAY FLUORESCENT PROPORTIONAL COUNTERS AT THE MOON AND MERCURY

Element	E_{Ka} (keV)	Signal-to-Noise at Nominal Abundances		Elemental Sensitivity (cm in %)	
		Moon	Mercury	Moon	Mercury
Na	1.080	7.9	20	8.3^{-2}	3.4^{-4}
Mg	1.303	22	56	4.2^{-1}	1.6^{-3}
Al	1.559	11	29	9.1^{-3}	3.4^{-3}
Si	1.838	14	38	2.3^{-2}	8.4^{-3}
Ca	4.038	0.5	1.3	-	7.4^{-2}
Ti	4.962	-	-	-	-
Fe	2.111	-	-	-	-

[1]10 sec observation time.

Table 4.7

PERFORMANCE OF A NON-FOCUSING X-RAY SPECTROMETER
FOR OBSERVATORY MODE OBSERVATIONS OF THE GALILEAN SATELLITES

Parameters	Satellites			
	Io	Europa	Ganymede	Callisto
a. Typical Source Flux from Major Elements (F_X, photons/cm^2 sec)	1.2^{4}	6.1^{3}	5.3^{3}	2.9^{1}
b. Typical Background Flux from the Surface (B_{xp}, photons/cm^2 sec keV)	7.0^{2}	2.0^{2}	2.0^{0}	-
c. Total X-ray Flux from RTG γ-rays and Bremsstrahlung at Detectors (B_{xsp}, photons/cm^2 sec keV)	10^{-3}	10^{-3}	10^{-3}	10^{-3}
d. Total Charged Particle Count Rate[1] (counts/sec)	3.0^{4}	3.0^{4}	3.0^{4}	3.0^{4}
e. Total Bremsstrahlung Count Rate (counts/sec)	6.0^{-2}	6.0^{-2}	6.0^{-2}	6.0^{-2}
f. Signal Count Rate[2] (counts/sec)	1.4^{-2}	7.0^{-3}	6.0^{-3}	3.3^{-6}
g. Signal-to-Background	2.3^{-1}	1.2^{-1}	1.0^{-1}	-
h. Signal-to-Noise for 1 Hour Observing Time	3.0^{0}	1.5^{0}	1.3^{0}	-
i. Elemental Sensitivity for Aluminum (2σ)%	3.7^{0}	7.5^{0}	8.6^{0}	-

[1]The high energy particle events can be discriminated against as long as they do not saturate the detector.

[2]Assumes a collecting area of 15 cm^2 and an angular diameter of = 0.1° for the satellites.

Table 4.8

PERFORMANCE OF A FOCUSING X-RAY SPECTROMETER
FOR OBSERVATORY MODE OBSERVATIONS OF THE GALILEAN SATELLITES

Parameters	Satellites			
	Io	Europa	Ganymede	Callisto
a. Typical Source Flux from Major Elements (F_x, photons/cm^2 sec)	1.2^{4}	6.1^{3}	5.3^{3}	2.9^{1}
b. Typical Background Flux from the Surface (B_{xp}, photons/cm^2 sec keV)	7.0^{2}	2.0^{2}	2.0^{2}	-
c. Total X-ray Flux from RTG γ-rays and Bremsstrahlung at Detectors (B_{xsp}, photons/cm^2 sec keV)	1.0^{-3}	1.0^{-3}	1.0^{-3}	1.0^{-3}
d. Total Charged Particle Count Rate[1] (counts/sec)	1.0^{3}	1.0^{3}	1.0^{3}	1.0^{3}
e. Total Bremsstrahlung Count Rate[2] (counts/sec)	2.0^{-3}	2.0^{-3}	2.0^{-3}	2.0^{-3}
f. Signal Count Rate[3] (counts/sec)	1.4^{-2}	7.0^{-3}	6.0^{-3}	3.0^{-6}
g. Signal-to-Background	7.0^{0}	3.6^{0}	3.0^{0}	-
h. Signal-to-Noise for 1 Hour Observing Time	7.1^{0}	4.4^{0}	4.0^{0}	-
i. Elemental Sensitivity for Aluminum (2σ)	1.6^{0}	2.5^{0}	2.8^{0}	-

[1]High energy charged particle events can be discriminated against.

[2]Assumes a detector area of 0.5 cm^2.

[3]Assumes a collecting area of 15 cm^2 and an angular diameter of 0.1° for the satellites.

are quite marginal for detector operation. Electron fluxes near the satellites are so high that neither collimated nor focusing approaches to background rejection would be practical.

Observatory mode observations of higher Z elements such as Ti and Fe also look attractive although we have not estimated the expected signal-to-noise. Detector sensitivities fall at the higher energies but background fluxes fall also. A more complete analysis of the performance of an x-ray fluorescence experiment in the Jovian system is clearly implied and warranted by our preliminary calculations. In particular there is a need to establish the optimum orbital inclination for making x-ray observations.

4.6 X-Ray Fluorescence Experiment Summary

X-ray fluorescence observations of light elements at the Moon and Mercury are practical using fairly simple proportional counter detectors. Observations of calcium, iron, and titanium may be possible at Mercury under active Sun conditions. A more thorough evaluation of the effect of charged particle bursts on x-ray observations is needed.

For the Galilean satellite observations in observatory mode with a focusing detector the computed sensitivities are quite encouraging and the possibility of measuring the abundances of many elements makes the method very attractive. There are a number of other factors which should be considered, however. First, x-ray fluorescence measurements only examine the outermost layer of the surface. Especially on the satellites of Jupiter the outer surface may not characterize even the layers immediately below them. For example, sputtering (the removal of surface atoms by the impact of energetic ions) is element dependent. Certain species can be preferentially sputtered off a surface which could make x-ray fluorescence measurements meaningless for a determination of the true crustal composition.

Second, determination of absolute elemental abundances is difficult for orbital x-ray fluorescence. The magnitude and shape of the solar x-ray flux is less well known than are laboratory x-ray sources. Furthermore, matrix effects cause variations in the x-ray flux from a given concentration of an element depending on the chemical and mineralogical nature of the surrounding material. Determination of elemental abundance ratios minimizes many of these difficulties; however, this is not as desirable a result as the magnitude of elemental abundances.

Third, since proton and electron bombardment preferentially excite x-ray fluorescence differently as a function of Z it may be difficult to predict the results of x-ray fluorescence measurements even on a relative basis until the differential proton and electron fluxes impinging on the satellite(s) are known from MJS measurements in the flux tube(s).

Finally, a more extensive investigation of the operation should be made to assess the effects of long-lived radioisotopes formed around the detector due to energetic proton bombardment during repeated passages through the radiation belts.

REFERENCES

4.1 Gast, P. R., et al., "Solar Electromagnetic Radiation," Chap. 16 in Handbook of Geophysics and Space Environments, S. L. Valley (ed.), McGraw-Hill Book Co., Inc., New York, 1965.

4.2 Leighton, R. E., Principles of Modern Physics, McGraw-Hill Book Co., Inc., New York, p. 423, 1959.

4.3 Reactor Physics Constants, ANL-5800, USAEC, p. 679, 1963.

4.4 Dick, C. W. and A. C. Lucas, "K-Shell Fluorescence Yields for Light Elements," preprint.

4.5 Adler, I., et al., X-Ray Fluorescence Experiment in Apollo 15, Preliminary Science Report, NASA SP-289, 1972.

4.6 Adler, I., et al., "Apollo 16 Geochemical X-Ray Fluorescence Experiment: Preliminary Report," Science, Vol. 177, p. 256, 1972.

4.7 Motz, J. W., First Progress Report, December 15, 1968 to December 15, 1969, DASA Order No. EO-852-69 and EO-850-70, National Bureau of Standards, Applied Radiation Division, Washington, D.C. 20234.

4.8 Messelt, S., "K-Shell Ionization by Protons," Nucl. Phys., Vol. 5, p. 435, 1958.

4.9 Bissinger, G. A., et al., "Study of the Production of K X-Rays in Ca, Ti and Ni by 2-28-MeV Protons," Phys. Rev. A1, p. 841, 1970.

4.10 Fink, R. W., "Atomic Fluorescence Yields," Rev. Mod. Phys., Vol. 38, p. 513, 1966.

4.11 "Pioneer 10 Reports," Science, Vol. 183, p. 301, 1974.

4.12 "Pioneer 11 Reports," Science, Vol. 188, p. 445, 1975.

4.13 Simpson, J. A., J. H. Eroker, J. E. Lamport, P. H. Walpole, "Electrons and Protons Accelerated in Mercury's Magnetic Field," Science, Vol. 185, p. 160, 12 July 1974.

4.14 See for example, S. C. Curran and Wilson,"Proportional Centers and Pulse Ion Chambers," in Alpha-Beta-Gamma-Ray Spectroscopy, Vol. I, K. Siegbahn (ed.), North Holland Publishing Co., 1968.

4.15 Palmer, H. F. and L. A. Braby, "A Parallel Plate Gas Scintillation Proportional Counter for Improved Resolution of Low-Energy Photons," Nucl. Ins. & Meth., Vol. 116, p. 587, 1974.

4.16 Herman, A. W., et al., "Target Backings for Charged Particle Induced X-Ray Fluorescence Analysis," Nucl. Ins. & Meth., Vol. 109, p. 429, 1973.

4.17 Musket, R. G., "Detection of Proton-Induced Boron X-Rays with a Si (li) Detector," Nucl. Ins. & Meth., Vol. 117, p. 385, 1974.

4.18 Gunthar Reigler, private communication.

4.19 Giacconi, R. and H. Gursky, X-Ray Astronomy, D. Reidel, Boston, Massachusetts, 1974.

4.20 Woodgate, B. E., T. Lowinger and M. Schneider, "Conical Focusing Crystal Spectrometers for Cosmic X-Ray Astronomy," Applied Optics, Vol. 12, No. 11, p. 2759, November 1973.

5. ATOMIC SPECTROSCOPY

Recent astronomical discoveries have opened up the rather unexpected possibility of determining the relative abundance of elements on the surface of a planet or satellite from observations of the resonant emission of atoms in the space environment near the object in question. Earth-based observations of sodium-D emission in the vicinity of the Jovian satellite Io were the first indication of a possible new geochemical remote sensing technique (Ref. 2.7). Subsequent detailed mapping of the intensity and distribution of the sodium cloud around Io and supporting theoretical analysis have led to a plausible quantitative model for the intensity of sodium emission (Ref. 5.1). Furthermore, emissions from other elements have also been predicted and some have already been observed.

According to Carlson et al. (Ref. 5.1), the source of fluorescing atoms such as sodium and potassium is sputtering of neutral atoms from the surface of Io by proton bombardment. These neutral atoms have a prolonged lifetime in the space environment near Io specifically in a toroidal zone corresponding to Io's orbit before they are ionized by electrons in the hot plasma of the radiation belts. Prior to ionization, radiation excites resonant emission in the neutral atoms which is diagnostic of the nature and column abundance along the line of sight of the neutral atom species.

Observations of resonant emission from a spacecraft in Jupiter orbit can potentially offer an enormous gain in the spatial resolution for mapping the sodium cloud and the threshold sensitivity for determining other atomic species. In the remainder of this section the subject of this threshold sensitivity for other atomic species is considered in the context of compositions that are expected for the Jovian satellites.

5.1 Estimated Intensity of Emission from Jovian Magnetospheric Atomic Species Originating from Satellite Surfaces

Emission from atomic species in the Jovian magnetosphere is a consequence of a complex set of physical processes which are still poorly understood. The estimates of emission presented in this section are based on the physical mechanisms that were accepted in early 1976. If it were repeated today it would need refinement. Nevertheless, most of the factors affecting the intensities of emission are reflected in the treatment that follows with the exception that the effect of possible satellite atmospheres on sputtering rates are not adequately allowed for.

Assumed Surface Composition

The composition of the satellite surfaces determines the concentration of different elements that is available for transfer to magnetospheric space. The possible composition of the Jovian satellites has already been discussed in Section 2 and has been used in assessments of the ability to detect elements by gamma-ray and x-ray spectroscopy of the satellites in Sections 3 and 4. Inasmuch as sodium emission from the vicinity of Io has been detected and measured as having a brightness of 30 kilo-Rayleighs (kR), it is convenient to discuss abundances, signal-to-noise ratios and sensitivities for other elements in relation to the values for sodium. In Table 5.1, the abundances of elements relative to sodium for the different satellites are given for an evaporite model of Io surface composition and for carbonaceous chondritic models of the compositions of the other satellites. All abundances are listed relative to the abundance of sodium in evaporite (Ref. 5.2).

Sputtering Rates

The intensity of resonant emission from the vicinity of a particular satellite depends on the excitation efficiency defined below and the rate at which atoms are supplied to the cloud. The supply rate depends on the intensity of proton bombardment, the sputtering efficiency and the size of the satellite. For the purpose of this analysis the simplifying

Table 5.1

ASSUMED SATELLITE SURFACE COMPOSITIONS

(Relative to Na Abundance in Evaporite on Io)

Element	Evaporite	Carbonaceous Chondrite
	J_1	J_1 to J_5
Na	1.0000	0.056
Ca	0.62	0.088
K	0.018	0.0051
Mg	2.3	0.97
Si	0.34	1.1

C-2

assumptions have been made that sputtering efficiency is independent of proton energy beyond 30 MeV and is equally efficient for all elements. Sputtering rate factor(s) relative to Io are computed with the following equation:

$$P_{J_X} = \frac{F_{J_X}}{F_{J_1}} \cdot \frac{r^2 J_X}{r^2 J_1} \qquad (5.1)$$

where: F_{J_X} = proton flux at the satellite with energy in excess of 30 MeV

r_{J_X} = radius of satellite J_X

and are listed in Table 5.2. These rate factors (Table 5.2), when multiplied by the surface atomic abundances given in Table 5.1, can be used to compute the relative rates of supply of atoms to the resonantly emitting clouds around the different satellites.

$$Q_e = P_{J_X} C_e \qquad (5.2)$$

where: Q_e = sputtering rate of atomic species e relative to sodium at Io

P_{J_X} = sputtering rate factor for a particular satellite J_X

C_e = abundance of element e on satellite surface J_X relative to abundance of sodium in evaporite on J_1.

Excitation Efficiencies Relative to Sodium

Since the brightness of the sodium emission from Io is known, emission from elements other than sodium can be computed and sensitivity thresholds can be defined from the excitation efficiencies relative to sodium. As defined here the excitation efficiency of an element relative to sodium is the ratio of the number of resonantly emitted photons for each atom of that element sputtered from the surface to the number of resonantly emitted photons for each atom of sodium that is sputtered.

Table 5.2

GALILEAN SATELLITE TO CLOUD TRANSFER (SPUTTERING)

Parameter	Galilean Satellites				
	J_1	J_2	J_3	J_4	J_5
Proton Flux (> 30 MeV)	1^{5}	7^{2}	1^{1}	1^{0}	6^{6}
Satellite Radius (km)	1.83^{3}	1.55^{3}	2.64^{3}	2.5^{3}	1.2^{2}
Sputtering Factor	1^{0}	5^{-3}	2^{-4}	2^{-5}	2.6^{-1}

For an element e it can be expressed as:

$$E_e = \frac{S_{\lambda e} \times (gf)_e \times \tau_e}{S_{\lambda Na\text{-}D} \times (gf)_{Na} \times \tau_{Na}} \qquad (5.3)$$

where: $S_{\lambda e}$ = solar intensity at the emission line wavelength (appropriately doppler shifted)

gf = line strength

τ_e = lifetime of neutral atom before ionization.

Values of the excitation efficiency are tabulated in Table 5.3.

Lifetimes of the elements are taken to be independent of satellite position; preliminary data on the plasma density about Jupiter indicate this to be a reasonable approximation for the order of magnitude required here.

Resonant Emission Intensities Relative to Sodium at Io

The resonance intensity of the emission from an element e at a satellite J_x in which its surface atomic abundance is C_e can be determined relative to sodium by the equation

$$B_e = B_o \cdot Q_e \cdot E_e \qquad (5.4)$$

since the brightness of sodium atoms at Io is 30 kR, then

$$B_o = 30 \text{ kilorayleighs.}$$

Predicted maximum emission cloud brightness for the different elements appears in Table 5.4.

Table 5.3

GALILEAN SATELLITE ATOMIC SPECIES' EXCITATION EFFICIENCIES

Element	J_1 to J_5
Na	1.00
Ca	0.097
K	0.56
Mg	0.017
Si	0.00026

Table 5.4

PREDICTED ATOMIC CLOUD BRIGHTNESS AT RESONANCE WAVELENGTHS

(Galilean Satellites and Amalthea)

Element	Line (Å)	Brightness (Rayleighs)					
		Evaporite	Carbonaceous Chondrite				
		J_1	J_1	J_2	J_3	J_4	J_5
Na	5896	3^{4}	2000	8	0.4	0.03	400
Ca	4227	2^{3}	300	1	0.05	0.005	70
K	7665	3^{2}	100	0.4	0.02	0.002	20
Mg	2852	1^{3}	600	2	0.1	0.001	100
Si	2516	3^{0}	10	0.04	0.003	0.0004	2

5.2 Experiment Performance Calculations

Given the extended source emission line intensities in Table 5.4, information on the effects of sky background, Rayleigh scattering, and gamma-ray and charged particle interference, the signal-to-noise can be predicted for observations of different elements at the different satellites once the characteristics of a particular instrument are known.

Alternatively, given a threshold signal-to-noise ratio, detection thresholds relative to sodium at Io can be determined. The characteristics of two instruments which are used in the design evaluation are given in Tables 5.5 and 5.6. The first is a photopolarimeter (PPS) being developed for spectral mapping from the Mariner Jupiter/Saturn (MJS). It is emphasized that this instrument was not optimized for the type of atomic spectroscopy considered here. The other instrument is a new type of spectrometer with an acoustically-tuned optical filter recommended by Space Science Board Summer Study (1974) for a Jupiter orbiter mission (Ref. 2.6). Both are nominally operated in a photon counting mode.

In Table 5.7 the sensitivity (defined in the first footnote under Table 5.7) of the MJS PPS instrument is determined allowing for the sky background and gamma-ray background due to the onboard Radio-Isotope Thermal Generator (RTG). Rayleigh scattering from the atomic clouds around the satellites is assumed negligible and the zodiacal light contribution to sky background which is significant for observations of the Jupiter system from the Earth is less at Jupiter (see second footnote, Table 5.7). The sensitivity is computed taking account of counting statistics for short duration observations but assuming that even very long duration observations will not improve the sensitivity below about 3% of background. Count rate background due to gamma-rays from the onboard RTG is estimated from experience with the design of the photopolarimeter experiment for the Mariner Jupiter/Saturn Mission (Ref. 5.4).

Table 5.5

DESIGN CHARACTERISTICS OF THE MARINER JUPITER/SATURN PHOTOPOLARIMETER (MJS-PPS)

a.	Spectral Range	2350 Å - 7500 Å
b.	Spectral Resolution (filter widths)	Visual 100 or 200 Å UV and IR 300 Å
c.	Field of View	1/16, 1/4, 1 or 4° (for a 15 cm aperture, 21 cm focal length telescope)
d.	Throughput	5% at 2516 Å, 20% at 5896 Å, 25% at 7665 Å
e.	Detector	Tri-alkali photomultiplier tube with quartz windows
f.	Dynamic Range	0 to 5×10^9 counts/sec equivalent intensity
g.	Radiation Tolerance*	Flux 5×10^8 cm^{-2} sec^{-1} Fluence 1×10^{13} cm^{-2}
h.	Sizing	2.5 kg, ≈ 3 w, up to 3 kbps

*3 MeV electron equivalence.

Table 5.6

DESIGN CHARACTERISTICS OF A HIGH RESOLUTION PLANETARY SPECTROMETER*

a.	Spectral Range	2500 Å - 8000 Å
b.	Resolution	0.5-6 Å
c.	Field of View	0.3° (for a 8 cm aperture, 100 mm focal length telescope)
d.	Throughput	25 to 35%
e.	Detector	GaAs photomultiplier tube
f.	Sizing	≈ 4 kg, ≈ 3 w, ≈ 1.6 kbps

*With acoustically-tuned optical filter.

Table 5.7

MJS PPS SENSITIVITY[1] FOR RESONANT EMISSION LINE BRIGHTNESS OVER SKY BACKGROUND[2] AND RTG NOISE[3]

Element	Line (Å)	Integration Time (sec)		
		0.4	4	40
Na	5896	2.7	0.82	0.26
Ca	4227	1.2	0.38	0.12
K	7665	11	3.4	1.1
Mg	2852	3.0	0.92	0.29
Si	2516	3.3	1.0	0.32

[1]The sensitivity in Rayleighs is determined as the brightness at which signal-to-noise equals 3, i.e.,

$$S/N = \frac{CRt^{\frac{1}{2}}}{(CR + B)^{\frac{1}{2}}} = 3,$$

where CR is count rate due to signal (Cf. Eq. 7j of Ref. 5.4 and 5.5), and

B is count rate due to background,
t is integration time.

[2]From Ref. (5.3) the sky background at high galactic latitudes in interplanetary space near Jupiter is 0.18 Rayleigh/Å at visual wavelengths (assumed to be the same for UV). At low galactic latitudes the background is a factor of 3.5 higher. Only sensitivities for high galactic latitude observations are given here. By comparison the sky background in the vicinity of the Earth is about 1.3 Rayleigh. All values are for elongations greater than 90° and at mid-galactic latitudes. Rayleigh scattering from the atoms is several orders of magnitude less than resonance scattering. A field of view of 1° is assumed.

[3]Assuming 100 noise pulses/sec from RTG γ's penetrating 7 gm/cm^2 of shielding.

In Table 5.8, the sensitivity of MJS PPS is redetermined taking trapped radiation at 16 R_J in the plane of Jupiter's magnetic equator into account. Radiation belt interference is again based on experience gained with the design of the photopolarimeter experiment for the Mariner Jupiter/Saturn Mission (Ref. 5.4).

In Table 5.9 the sensitivity of the tunable acousto-optical filter (TAOF) instrument to resonant emission by atomic species is determined assuming that skylight is the only source of background. The data apply to emissions by any species in the wavelength range 2300 to 8000 Å. This serves to illustrate maximum capabilities of this instrument, presuming future technological developments will result in a reduction in RTG radiation output.

In Table 5.10 the sensitivity of the TAOF instrument is recomputed, taking account of count rate background due to gamma-rays from the on-board RTG. RTG background and radiation belt interference are estimated from experience with the design of the photopolarimeter experiment for the Mariner Jupiter/Saturn Mission (Ref. 5.4). In Table 5.11, the sensitivity of the TAOF is redetermined taking trapped radiation into account. Since long-range observatory-mode observations are the norm for this atomic spectroscopy experiment, the highly reduced sensitivities determined for the 16 R_J location in Table 5.11 are of no serious consequence to the experiment.

It is readily seen that the sensitivities with the MJS PPS (Table 5.8) are not as high as the capabilities of the TAOF device (Table 5.11). The performance of the MJS PPS in its normal role as a geochemical reconnaissance device for satellite surfaces is not evaluated in this report.

Table 5.8

MJS PPS SENSITIVITY[1] FOR RESONANT EMISSION LINE BRIGHTNESS OVER SKY BACKGROUND, RTG NOISE AND RADIATION BELT INTERFERENCE AT 16 R_J[2]

Element	Line (Å)	Integration Time (sec)		
		0.4	4	40
Na	5896	3.8	1.2	0.37
Ca	4227	1.7	0.52	0.17
K	7665	29	8.9	2.8
Mg	2852	3.7	1.2	0.36
Si	2516	4.3	1.0	0.42

[1]See Note 1 under Table 5.7.

[2]Electron flux (No. of electrons with energy greater than 3.2 MeV/cm^2) = $10^{5.46}$, after Ref. (2.7). Penetration rate computed from JPL SIGMA I code.

Table 5.9

TAOF SENSITIVITY[1] (RAYLEIGHS) FOR RESONANT EMISSION LINE BRIGHTNESS[2] OVER SKY BACKGROUND

Sky Background (Rayleighs)[3]	Integration Time (seconds)		
	1	10	100
High Galactic Latitudes (< 0.2)	0.18	0.045	0.013
Low Galactic Latitudes (< 0.7)	0.30	0.085	0.026

[1]See Note 1 below Table 5.7.

[2]Assuming a 1 Å resolution instrument.

[3]See values in Note 2 below Table 5.7.

Table 5.10

TAOF SENSITIVITY[1] (RAYLEIGHS) FOR RESONANT EMISSION LINE BRIGHTNESS OVER SKY BACKGROUND AND RTG NOISE[2]

Sky Background (Rayleighs)	Integration Time (seconds)		
	1	10	100
High Galactic Latitudes (< 0.2)	0.37	0.11	0.033
Low Galactic Latitudes (< 0.7)	0.44	0.13	0.040

[1]See Note 1 below Table 5.7.

[2]See Note 3 below Table 5.7.

Table 5.11

TAOF SENSITIVITY[1] (RAYLEIGHS) FOR RESONANT EMISSION LINE BRIGHTNESS OVER SKY BACKGROUND, RTG NOISE AND RADIATION BELT INTERFERENCE

Range (R_J)	Magnetic Latitude (deg)	Flux No. of Electrons per cm^2 with Energy > 3.2 MeV	Integration Time (sec)		
			1	10	100
16	52	12.3 [3]	0.59	0.17	0.054
32	52	1.0 [1]	0.37	0.11	0.033
40	30	1.0 [1]	0.37	0.11	0.033

[1]See Note 1 below Table 5.7.

[2]Sky backgrounds assumed are those for high galactic latitudes.

5.3 Atomic Spectroscopy Experiment Summary

The analysis above shows that a tunable acousto-optical filter spectrometer can be used to conduct observatory mode observations of resonant emission of a number of different atomic species expected to occur in the vicinity of Io, Europa, Ganymede and Amalthea. Because of the lower background light levels, sensitivities should be considerably improved over those possible from Earth orbit which in turn would be an improvement over sensitivities for Earth-based observations, particularly of course for emissions in the ultraviolet. Gamma-ray background from the onboard RTG is a significant factor in the sensitivity thresholds but trapped radiation is not a serious problem because observations can be conducted at high magnetic latitudes and very long ranges from Jupiter. Dose accumulation during equatorial crossings will degrade the instrument but should not be serious with periapsis near Ganymede. The elements magnesium, calcium, and silicon (in addition to sodium and potassium) should all be observed by a Jupiter orbiter if they occur in the presently expected concentrations.

As well as improved sensitivity, the other advantages of observations of resonant emission from Jupiter orbit are the improved spatial resolution and three-dimensional mapping of the more intense clouds such as that of sodium. These observations could result in a much improved model for the formation of atomic clouds in the orbit of the satellites of Jupiter. Observations over a range of phase angles may yield the optical thickness of the clouds. Observations of the dark sides of the satellites particularly during Jupiter eclipse of the Sun may show emission stimulated by proton and electron bombardment (aurorae).

Spectrometers or photometers with spectral resolution of 100-300 Å such as the MJS PPS or LPO visible and near-infrared reflectometer would also be capable of mapping Na and K concentrations around J_1 and J_5. This assumes that spectral filter passbands are selected to specifically examine the intensity in the emission lines of sodium and potassium relative to the continuum. Reconnaissance (but not identification) of other

emissions may also be made for J_1, J_2, and J_5. We reiterate here that the MJS PPS and LPO visible and near-infrared reflectometers are not designed for the type of atomic spectroscopy experiment discussed in this section. A corollary of this statement is that the LPO payload does not include certain instruments, such as the TAOF, which are probably preferred for remote sensing geochemical studies of the Galilean satellites.

REFERENCES

5.1 Carlson, R. W., D. L. Matson and T. V. Johnson, "Electron Impact Ionization of Io's Sodium Emission Cloud," Geophysical Res. Lett., Vol. 2, No. 10, p. 469-472, 1975.

5.2 Fanale, F. P., T. V. Johnson and D. L. Matson, "Io's Surface and the History of the Galilean Satellites," Proceedings, IAU Colloquium No. 28, "Planetary Satellites," Ithaca, New York, 1974.

5.3 Weinberg, J. L., M. S. Hanner, D. E. Beeson, L. M. DeShields II, and B. A. Green, "Background Starlight Observed from Pioneer 10," Journal of Geophysical Research, Vol. 79, p. 3665-3670, 1974.

5.4 Charles F. Lillie, private communication, 1974.

5.5 Jenkins, F. A. and H. E. White, Fundamentals of Optics, McGraw-Hill, New York, 1957.

6. GRAVITY FIELD AND ALTIMETRY EXPERIMENT

6.1 Experiment Concept

The goal of the radar altimeter/gravity experiment is to acquire data on planetary topography and local gravity field which can be interpreted in terms of surface constructional and degradational processes and the distribution of mass within a planet. The relationship of topography to shallow mass distribution defines the isostatic state of a planet's crust from which we may infer its level and type of tectonic activity and internal strength/viscosity. Deep-seated mass distribution asymmetries may reflect events of planetary accretion, differentiation, or present internal dynamics.

Two instruments are required for this experiment--a radar and a radio (spacecraft-to-Earth) transmitter. The latter can be the usual communications link for returning data to Earth. The radar transmits a pulse to illuminate the surface beneath the spacecraft, and then measures the time delay to reception of the reflected pulse, a direct indication of spacecraft altitude. The radio signal from the spacecraft is tracked in doppler frequency to model the orbit followed. The structure in the planet's gravity field due to rotational flattening, mascons, etc., will be reflected in deviations of the doppler signal from that expected for a spherically symmetric mass. As a possible alternate approach to gravity field mapping a gravity gradiometer, which senses the components of the local gravity field gradient, is also considered.

The following two subsections consider separately radar altimetry and gravity field mapping techniques for the baseline geology orbiter missions. A candidate radar instrument is described along with its performance evaluation. The sensitivities of gravity mapping techniques for baseline missions are also discussed. The final section of this chapter discusses the geophysical importance of the combined results of the altimetry and gravity phases of this experiment.

6.2 Radar Altimetry

A simple radar altimeter, envisioned here for a geology orbiter, will gather two types of data:

1. A record of spacecraft altitude during orbit or flyby from the time delay between transmission and reception of pulses.
2. A record of reflected power versus time for some or all of the received pulses.

The first data set should allow the compilation of topographic maps and profiles, once the effect of the spacecraft trajectory has been removed. The second data set may allow detection of regional differences in radar scattering cross section and variations in slope within the area of a single reflected pulse.

Types of Radar Altimeters

Two types of radar altimeters, each with distinct advantages, are suitable for a geology orbiter spacecraft. A beam-width-limited radar transmits a pulse confined to a small solid angle in the direction of the subspacecraft point. The entire returned pulse originates from within a small sample of surface, so determinations of range and scattering properties can be uniquely referred to a geographic location. Because the transmitted beam is narrow, antenna gain is high, and the transmitted power can be relatively small. Two disadvantages of a beam-width-limited radar are that it requires a steerable antenna be pointed at the subspacecraft point at all times, and the antenna radius must be large compared to the radar wavelength to focus the narrow illuminating beam. Also, this large antenna surface must be free of imperfections. Given the typical size of planetary spacecraft, the radar wavelength could be no longer than a few millimeters.

The second type of radar, termed pulse-length-limited, transmits a broad beam, then performs time delay processing on the reflected signal to separate out the return from the vicinity of the subspacecraft point. Antenna pointing is less critical for this type of radar, but more transmitted power is necessary and signal processing is more complex.

An additional criticism of a pulse-length-limited radar is the ambiguity from rough terrain, where the earliest echo may originate from a topographic high away from the subspacecraft point. Thus both the horizontal and vertical resolution of the radar may vary as a function of the topography being measured.

The geology orbiter is envisioned to be a relatively large and sophisticated spacecraft, perhaps of Mariner or Viking class, either three axis stabilized or with a despun platform, and probably nadir pointing. Thus, incorporation of a steerable antenna for the radar should pose fewer problems. Because of this fact and the disadvantages of the pulse-length-limited radar cited above, a radar instrument of the beam-width-limited type has been chosen for evaluation in this study. The basic characteristics of this radar, proposed for the Lunar Polar Orbiter, LPO, (Ref. 6.1), are shown in Table 6.1. The radar wavelength is 2 cm, the antenna diameter is 61 cm, and the resultant beam width is 2.3°. The spacecraft ground-track is sampled at a rate of 1.6 pulses/sec, requiring a data rate of 625 bps. Pulses are paired, first a narrow bandwidth pulse determines the approximate range to adjust high resolution range gates, then a compressed pulse is transmitted. The radar uses the technique of pulse compression to increase the effective peak power of the transmitted pulse 27 db above the actual 50 watts. A db budget for the radar system is shown in Table 6.2. This is based on the equation for received power, P_r, noise power, P_n, and signal-to-noise ratio, SNR:

$$P_r = \frac{P_t G_a}{4\pi h^2} \cdot \sigma_o(\alpha) \cdot A_s(\alpha) \cdot \frac{A_a}{4\pi h^2} \cdot G_c \cdot L \qquad (6.1)$$

$$P_n = kTB \qquad (6.2)$$

$$SNR = P_r/P_n \qquad (6.3)$$

Table 6.1

SIMPLE BEAM-WIDTH-LIMITED RADAR ALTIMETER[1]

Weight	7 kg[2]
Power Consumption	17.5 w continuous
Data Rate	625 bps (1.6 pulses/sec)
Antenna Diameter	0.61 m
Frequency	15 GHz
Peak Transmitted Power	50 w
Bandwidth	100 kHz, 7.5 MHz
Compression Gain	1, 512
Beam Width	2.3°

[1]Ref. 6.1.

[2]Weight includes antenna, but there is no allowance for instrument-to-antenna waveguide.

Table 6.2

PROPOSED LPO RADAR ALTIMETER DECIBEL BUDGET

Term	Factor	Gain (db)	Loss (db)
P_t = 50 w	P_t	17	-
$G_a = 9.2 \times 10^3$, $\lambda = 2$	$\frac{(G_{a\lambda})^2}{4\pi}$	34	-
G_c = 512	G_c	27	-
L, System + Filter Losses	L	-	12
h = 100 km	$\left(\frac{1}{4\pi h^2}\right)^2$	-	222
$\sigma_o = (\alpha = 0°, 20°)\ A_s$	$\sigma_o A_s$	68, 41	-
T = 775°K	$\frac{1}{kT}$	-	-200
B = 7.5 MHz	$\frac{1}{B}$	-	69
TOTAL		146,119	103

RESULTANT SNR = 43 db ($\alpha = 0°$), 16 db ($\alpha = 20°$)

where: P_t = transmitted power
G_a = antenna gain
h = spacecraft altitude
$\sigma_o(\alpha)$ = scattering cross section per unit area
α = mean topographic slope
$A_s(\alpha)$ = reflecting area of surface resolution element
A_a = antenna area
G_c = pulse compression gain
L = all losses
P_n = noise power
k = Boltzman's Constant = 1.38×10^{-23} watt/K° Hz
T = receiver temperature
B = receiver bandwidth
SNR = signal-to-noise ratio.

The nominal altitude of the LPO is a constant 100 km. The radar backscatter cross section, σ_o, of the lunar surface is a function of slope, α. Backscatter signal gain ranges from 40 to 68 db for mean slopes of 20° to 0°, respectively, within the footprint illuminated by the radar. The proposed LPO radar has a range resolution of 10 m and returns data with a SNR of 16 to 43 db, depending upon the slope of the terrain.

Geology Orbiter Radar

The baseline geology orbiter missions differ significantly from the nominal LPO mission, so the candidate geology orbiter radar system has been altered from the LPO system just described. In general, a geology orbiter will operate at much higher altitudes above its target planet. In order to recover the corresponding signal loss the radar antenna has been enlarged by a factor of two, and range resolution has been degraded by a factor of 5. The larger antenna is 1.2 m in diameter, which should present no special design problems. The new range resolution of 50 m should be adequate for topographic and geophysical studies of features 5 to 10 km across, the size of the radar footprint expected for baseline orbiter missions. An elliptical Mercury orbiter and the Jovian satellite

tour mission differ from the LPO and Mars missions in that the returned radar signal will be shifted in frequency due to large variations in the spacecraft radial velocity. The radar receiver for these missions must incorporate frequency tuning to track the doppler shift of the reflected pulse. Table 6.3 compares radar specifications and performance for the baseline geology orbiter missions and LPO. A lunar backscatter cross section has been assumed for all target objects and a useful SNR lower limit of 15 db is assumed.

The highly elliptical orbit of the baseline Mercury mission will allow the taking of useful data in rough terrain (slopes ≈ 20°) only in the vicinity of periapsis, up to an altitude of 1000 km. Depending on the latitude chosen for orbit periapsis, up to 76% of the planet can be seen by the altimeter. The sampling rate of 0.8 high resolution radar pulses per second translates into a ≈ 4 km spacing of 5 km radius radar footprints. Ground tracks of successive orbits will be offset approximately 1.5° or 63 km at the equator.

The baseline Mars mission calls for a circular nearly polar orbit. The radar footprints, with a constant radius of 10 km, will be spaced about 3 km apart. Successive orbits will be rotated approximately 36° in longitude. It is anticipated that the orbital period will be varied to allow the spacecraft ground track to walk at other rates in longitude. Over one Mars year mission about 6000 orbits could be completed, so adjacent tracks of altimeter data might be separated by as little as 0.02° in longitude or 1.2 km at the equator.

Radar altimeter performance at the Jovian satellites can be bracketed by two extreme Ganymede encounter trajectories which are compared in Table 6.4. If a mission encompasses 20 Ganymede flybys at varying latitudes then about 1% of the surface will be observed by radar. More significantly, flybys from satellite resonant orbits can be directed to the inside or the outside of a satellite orbit, so it should be possible to obtain 10 altitude profiles, 70° long, spaced 20° in latitude on each hemisphere. Locally, two or more adjacent tracks of altimetry will provide a real spatial resolution approaching 20 km.

Table 6.3

COMPARATIVE PERFORMANCE OF RADAR ALTIMETERS FOR BASELINE MISSIONS

Parameters	Moon	Mercury	Mars	Jovian Satellites
INSTRUMENT				
Antenna Size	0.6 m	1.2 m	1.2 m	1.2 m
Range Resolution	10 m	50 m	50 m	50 m
Doppler Tuning Required?	no	yes	no	yes
PERFORMANCE				
Beam Footprint Radius	1 to 3 km	5 to 10 km	10 km	5 to 10 km
SNR db (altitude)				
Slopes 0°	43 db (100 km)	41 db (500 km)	35 db (1000 km)	41 db (500 km)
		35 db (1000 km)		35 db (1000 km)
Slopes 20°	16 db (100 km)	21 db (500 km)	15 db (1000 km)	21 db (500 km)
		15 db (1000 km)		15 db (1000 km)
Percent Coverage at SNR at Least 15 db	100	up to 76	100	1 to 2 (20 passes each)

Table 6.4

RADAR DATA CHARACTERISTICS FOR A JUPITER ORBITER AT GANYMEDE

Hyperbolic Approach Velocity V_∞ (km/sec)	Penapsis Altitude (km)	Time Spent Below 1000 km Altitude (min)	Length of Reduced Swath (km)	Average Spacing of Elevation Samples (km)
2.1	500	20	3500	2.4
9.5	500	6	3000	10.4

To convey any information on the figures of Jovian satellites the individual altimetry profiles must be tied together by accurately removing the individual flyby orbits. Radio and optical tracking alone are inadequate for this task; positional errors are now estimated to be tens of kilometers (Ref. 6.2). Two strategies should markedly improve this situation:

1. Use the radar altimeter data as an additional input to orbit determination calculations.

2. Constrain each track of altimetry data (the surface projection of a flyby trajectory) to cross at least one other track of data. Each flyby trajectory can thus be linked to at least one other such trajectory.

The impact of these uses of radar data to improve orbit determination precision must be evaluated quantitatively, but the 50 m range resolution of the radar suggests the reduction of positional errors to less than a kilometer may be possible.

Radar Altimetry Summary

A radar altimeter instrument, similar to that proposed for the Lunar Polar Orbiter, can return topographic data of significant geological interest from planetary orbiters of Mercury, Mars, and the Jovian satellites. Radar scattering cross section and range, determined with a resolution of 50 m, are measured in 5 to 10 km radius circles about the subspacecraft point. Coverage of Mercury and Mars is not only extensive (75 to 100%) but may also achieve areal resolution of a few tens of kilometers. Topography data returned from Jovian satellites will be sparse. The limited number ($\simeq$ 20) of flybys will prevent the determination of terms above about third degree in a harmonic model of topography, but spatial resolution along individual profiles should be approximately 20 km.

6.3 Gravimetry

Determination of the external gravity field of a body, particularly the higher order gravitational coefficients, provides important information on the internal structure of the body. For example, measurement of the odd order gravitational harmonics, i.e., J_3, tells whether or not the body is in hydrostatic equilibrium or whether it has sufficient interval strength to support non-equilibrium figures over long intervals of time. The gravitational harmonics are proportional only to the differences in the moments of inertia of a body as they arise from angular variations in the mass distribution. By themselves the gravitational harmonics are not sufficient to calculate the planetary moments of inertia, but must be combined with other dynamical parameters, such as precession constants, in order to uniquely calculate the planetary moments.

For this study it is assumed that planetary masses have been accurately determined from earlier flyby missions (Ref. 6.3), hence the emphasis here is on the higher order gravitational coefficients. Doppler tracking and gravity gradiometers are the primary data sources considered. The purpose here is to ascertain the feasibility of determining planetary gravity fields for the baseline geology orbiter missions.

Gravity Gradiometers

Gravity gradiometers are designed to measure the gradient of a gravitational field and, as a data source for investigating the gravity fields of bodies, offer certain advantages over doppler tracking. Gradiometers can determine the gravity gradients in three orthogonal directions rather than just along the line of sight to the Earth as is characteristic of doppler tracking. Gradiometer data can be stored onboard for later relay to Earth, thus avoiding data loss when the spacecraft is occulted. Also, the gradiometer responds to gravity gradients, not accelerations, and consequently is not directly affected by perturbations such as control jet leaks. Offsetting these advantages is the fact that part of the science payload consists of the gradiometer (doppler tracking requires no additional instrumentation) and the requirement to develop a new instrument.

Gravity gradiometers have been considered by Forward (Ref. 6.4) for determination of the gravity field of planets, satellites, and asteroids and are currently being studied at JPL for Earth orbital applications. This study considers gravity gradiometers as a data source for determining the gravity field of the Galilean satellites from hyperbolic trajectories and of Mars and Mercury from baseline orbiter missions.

A wide variety of satellite encounter trajectories are possible from Jupiter orbit. In this study the trajectories described by Beckman and Miner (1975, Ref. 6.5) and by Friedlander and Davis (1976, Ref. 6.6) were used. To derive quantitative estimates of the sensitivity of the flyby gravity experiment, estimates of the magnitudes of the gravitational coefficients for the Galilean satellites are necessary. As these bodies are comparable in size (and perhaps in structure) to the Moon and Mercury, we assume that gravitational harmonics of the Moon and Mercury indicate the order of magnitude of the gravitational harmonics of the satellites. J_2 of the Moon is 2.07×10^{-4} and preliminary reduction of the first and third Mariner 10 Mercury encounters indicates that J_2 of Mercury is of the order of 10^{-4}; however, further analysis is necessary before this result is firm. For purposes of calculating the sensitivity of various data sources to gravitational harmonics a value of 1×10^{-4} was adopted for all satellite harmonics. The sensitivities are linear in the harmonic coefficients, hence results for other values are easily obtained.

The magnitudes of gravity gradients are given by:

$$\Gamma_{xx} = \frac{-\mu}{r^3}\left(1 - 3\frac{x^2}{r^2}\right) - \left(\frac{R_e}{r}\right)^2 \cdot \frac{3}{2} J_2 \cdot$$

$$\left[\left(1 - \frac{5x^2}{r^2}\right) - 5 \sin^2 L\left(1 - 7\frac{x^2}{r^2}\right)\right] + \ldots \qquad (6.4)$$

Similar expressions for Γ_{yy} and Γ_{zz} are obtained by replacing x by y and z, respectively. In the above expression, r is the distance from the center of mass, x, y, and z are the location with respect to Cartesian body fixed coordinates whose origin is at the mass center of the body, L is the latitude with sin L = z/r, and R_e is the equatorial radius of the body. Figure 6.1 shows the magnitude of the gravity gradient due to J_2 evaluated along trajectories that are hyperbolic relative to Ganymede and assuming $J_2 = 1 \times 10^{-4}$ for Ganymede. Periapse of the trajectory was in the satellite equatorial plane with the x axis pointed toward periapse and the z is along the rotation axis of the satellite. For the types of gradiometers proposed for spacecraft missions sensitivities of the order of 1 E.U. (1 E.U. = 10^{-9} sec^{-2}) for short (10 sec) integration times to 0.3 E.U. for 30 sec integration times are feasible. Future developments might lead to sensitivities of 0.01 E.U. For an instrument sensitivity of 0.3 E.U. the gravity gradient at Ganymede could not be detected unless J_2 was substantially greater than 1×10^{-4}.

Even reducing the periapse altitude to 100 km (which assumes improved orbit determination capability) does not result in a detectable gravity gradient. Consequently the gravity gradiometer does not appear promising as a data source for mapping satellite gravity field without a major increase in the sensitivity.

Figure 6.2 compares doppler tracking and gravity gradiometer for mass determination to an accuracy of 1% along hyperbolic encounters. For large bodies such as the Galilean satellites doppler tracking is far more sensitive; gradiometers are preferable for small bodies of 100 km diameter.

The conclusion reached here, that gravity gradiometers are not particularly suitable for the first order investigations of gravity fields from hyperbolic trajectories, is in agreement with preliminary results from Lorell (Ref. 6.7) comparing doppler tracking and gravity gradiometers for Earth and lunar orbital applications. For high altitude orbital measurements, as from the baseline Mercury and Mars geology orbiter missions, doppler tracking also appears superior for measuring gravity harmonics.

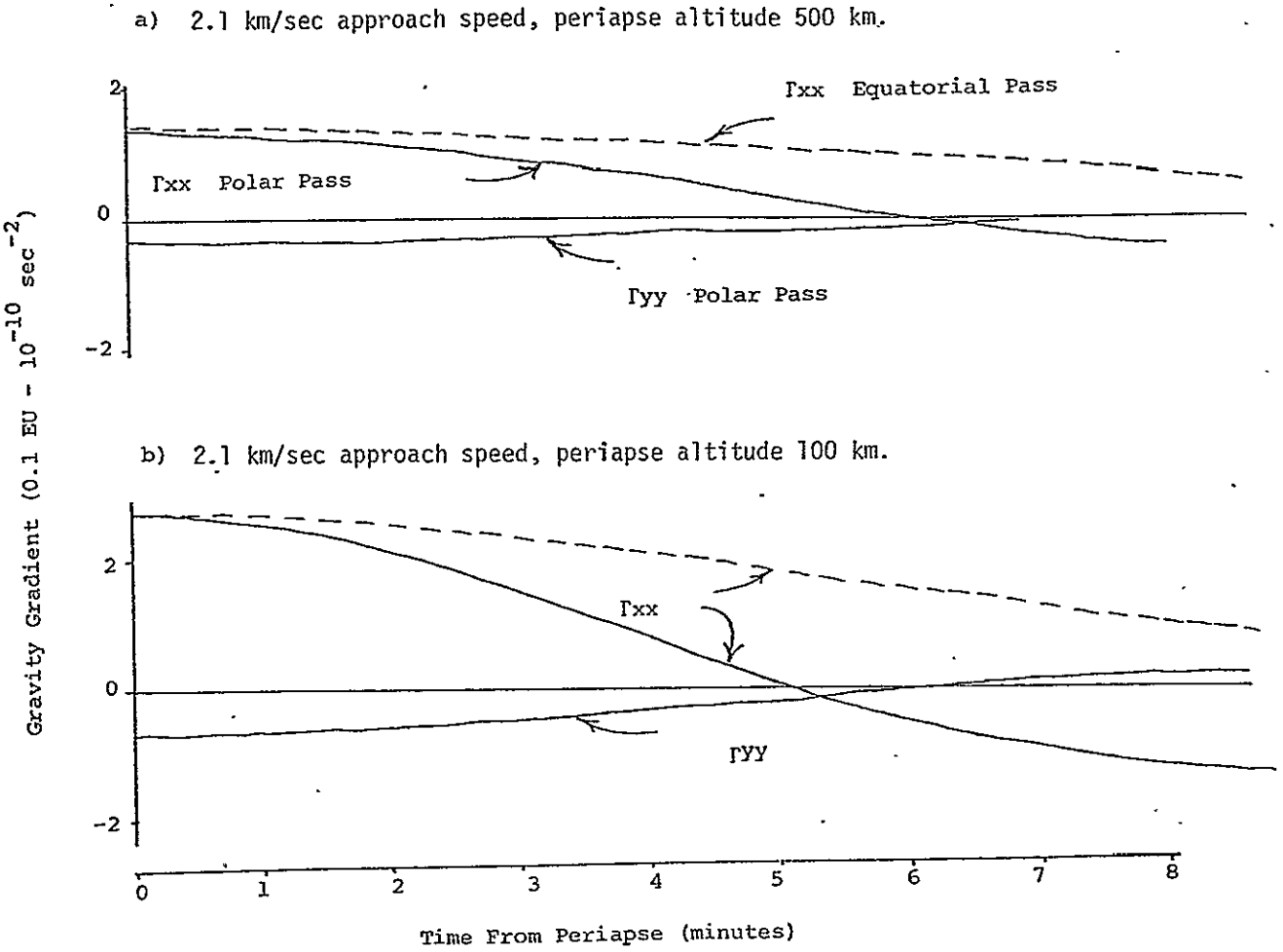

Figure 6.1 J_2 Gravity Gradient Signatures Along Ganymede Encounter Trajectories.

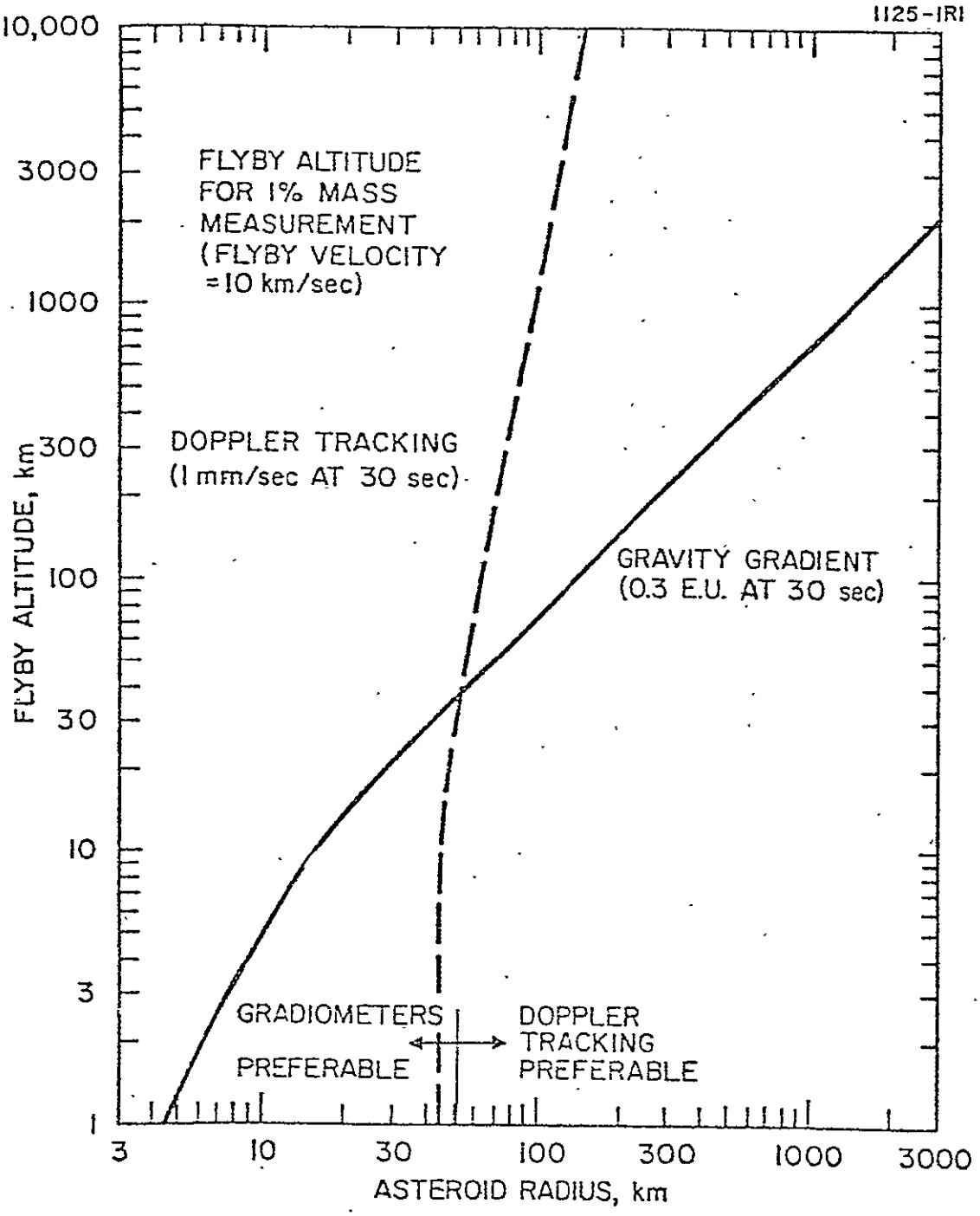

Figure 6.2 One Percent Measurement Altitude for Asteroids of Various Radii at 10 km/sec Flyby Velocity.

Doppler Tracking

The primary data source for gravity field determinations from spacecraft missions has been Deep Space Network (DSN) tracking, particularly doppler range rate measurements. Current tracking accuracy for range rate is less than 1 mm/sec; a value of 0.5 mm/sec is used here.

Mercury

The baseline Mercury orbiter mission involves an eccentric high inclination orbit with periapsis at an altitude of 500 km. The Mariner 9 Mars orbiter had a similar orbit so gravimetry results from that mission (Ref. 6.3) should indicate what might be expected from Mercury. The Mariner 9 spacecraft took data for 694 orbits of Mars. The periapsis altitude of 1600 km limited doppler tracking sensitivity to gravity field harmonics of ninth degree. A one-year Mercury orbiter mission would return about twice this volume of doppler tracking data distributed evenly over equatorial and mid-latitudes. The lower periapsis of the Mercury orbiter would perhaps permit resolution of higher order harmonics than of Mars; however, the physical validity of the high-order harmonics from a single orbiter is questionable. Some terms and uncertainties from a Mars gravity field model are shown in Table 6.5.

Mars

The baseline Mars geology orbiter mission is ideal for sensing structure in the gravity field down to the scale of the spacecraft altitude. Essentially the entire surface of Mars will be overflown at 100 km altitude many times. A one-Mars-year mission would yield almost 8000 orbits of data. Existing ninth degree harmonic models of Mar's gravity field could be refined and extended to approximately twelfth degree.

Table 6.5

NORMALIZED SPHERICAL HARMONIC COEFFICIENTS OF A GRAVITY FIELD MODEL* FOR MARS

Harmonic Coefficient	Value × 10^5
J_2	87.78 ± 0.92
C_{22}	-8.27 ± 0.33
S_{22}	5.06 ± 0.35
J_3	1.30 ± 0.67
J_4	-0.42 ± 0.54
J_5	0.22 ± 0.45
J_6	0.01 ± 0.04
J_7	-0.30 ± 0.36
J_8	0.16 ± 0.35
J_9	-0.14 ± 0.35

*Ref. 6.7.

Jovian Satellites

A Jupiter Orbiter mission with repeated satellite encounters provides a novel situation for investigating satellite gravity fields; a situation which is intermediate between the type of flybys previously flown, which involved one to three encounters with the target body, and a planetary orbiter mission. For the Quadrature Tour described by Beckman and Miner (Ref. 6.5) each satellite is encountered from 10-22 times over the 31-month life of the mission. Previous planetary flyby missions have yielded little data on the gravitational harmonics of target bodies. However, the Mariner 10 Mercury encounters (only two of which were useful for obtaining gravity data) may yield values of the second order harmonics, although the final precision of these results is uncertain at this time. The degree to which multiple flybys of the same body permit improved gravity field determination depends on the specific encounter trajectories, particularly on the periapse altitude and the geometry of the encounter. Both the doppler and gravity gradient signatures vary strongly with periapse altitude. The minimum allowable periapse altitude is primarily determined by the navigation accuracy which can be achieved; Beckman and Miner (Ref. 6.5) constrained the periapse altitude to be greater than 1000 km. Friedlander and Davis (Ref. 6.3) consider periapse altitudes of 500 km to be feasible with improvement to 100-200 km possible for some encounter trajectories. The satellite relative orbit determination accuracies play a very important role in the feasibility of gravity field mapping and interpretation of the satellites, a role which requires further investigation, particularly for low encounter speed trajectories. Also, satellite relative altitude information derived from radar altimetry could improve knowledge of the satellite relative orbit.

As is generally the case in mission design, tradeoffs will be required to maximize the overall science return. For example, the satellite approach conditions for the Quadrature Tour, designed with imaging requirements in mind, approach the satellite at right angles to the satellite-Sun line and fly over one of the satellite poles. As the satellite-Earth line

is within 11° of the satellite-Sun direction, the trajectory plane is nearly perpendicular to the direction to the Earth, resulting in very unfavorable doppler tracking geometry during the encounter. Better tracking geometry will require some compromise with the imaging requirements.

The sensitivity of the speed along hyperbolic encounter trajectories to several gravitational harmonics is given in Figures 6.3 and 6.4. Two trajectories are considered: first, a low encounter speed, 500 km periapse encounter which is representative of trajectories designed for deployment of and communication with penetrators at the satellites, and second, a high approach speed, 1000 km periapse trajectory more typical of encounter conditions for satellite tour trajectories. The velocity perturbations shown represent the maximum possible range rate signal; in general the range rate will be smaller due to the geometry of the encounter relative to the Earth-satellite line. The important result from these figures is that there is a detectable doppler signal for typical satellite encounters given harmonics of 1×10^{-4}. Close encounters should provide measurable signals even if the coefficients are smaller by two orders of magnitude. Also, as expected, the higher order harmonics are quite sensitive to periapse altitude. For the trajectories considered here it appears that the fourth order harmonics are about the limit that would generate detectable signals.

To ascertain the accuracy with which the gravitational harmonics could actually be measured, the results of an approximate linearized covariance analysis for hyperbolic encounters (Anderson, 1971, Ref. 6.8, Dixon, 1976, Ref. 6.9) may be utilized. Figure 6.5 shows the 1σ error in estimating J_2 as a function of periapse distance for Io encounters. For a periapse altitude of 1000 km the standard deviation in the estimate is $\simeq 5 \times 10^{-5}$, which if J_2 is 1×10^{-4}, gives an error of 50%. Multiple encounters will enable the uncertainty to be reduced; treating the estimates as statistically independent and using ten high quality, equal weight estimates of J_2 would reduce the error to $\simeq$ 15% of the assumed value of J_2. Results at other satellites may be somewhat more

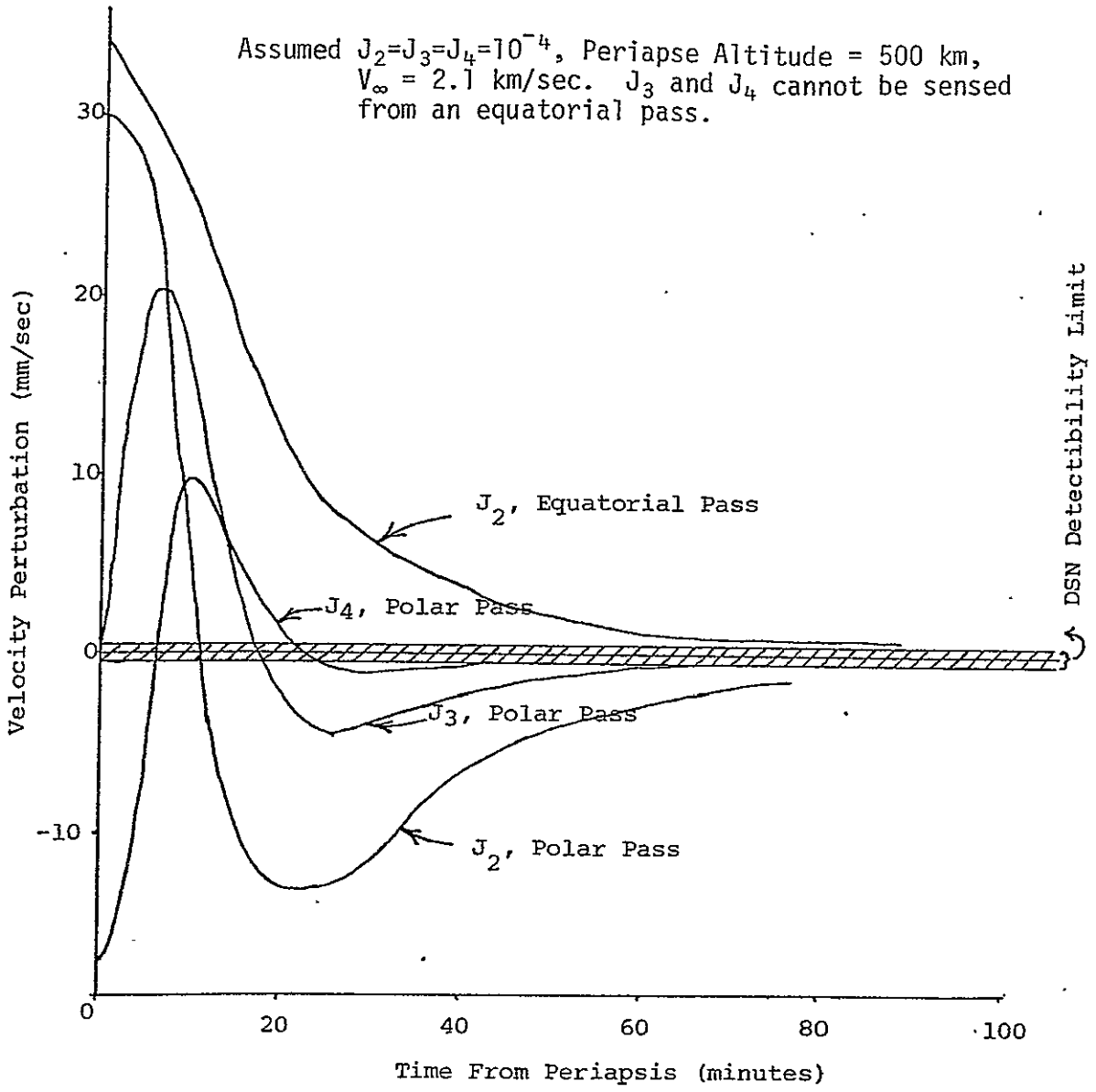

Figure 6.3 Velocity Perturbation During Flyby Caused by Low Order Gravitational Coefficients of Ganymede.

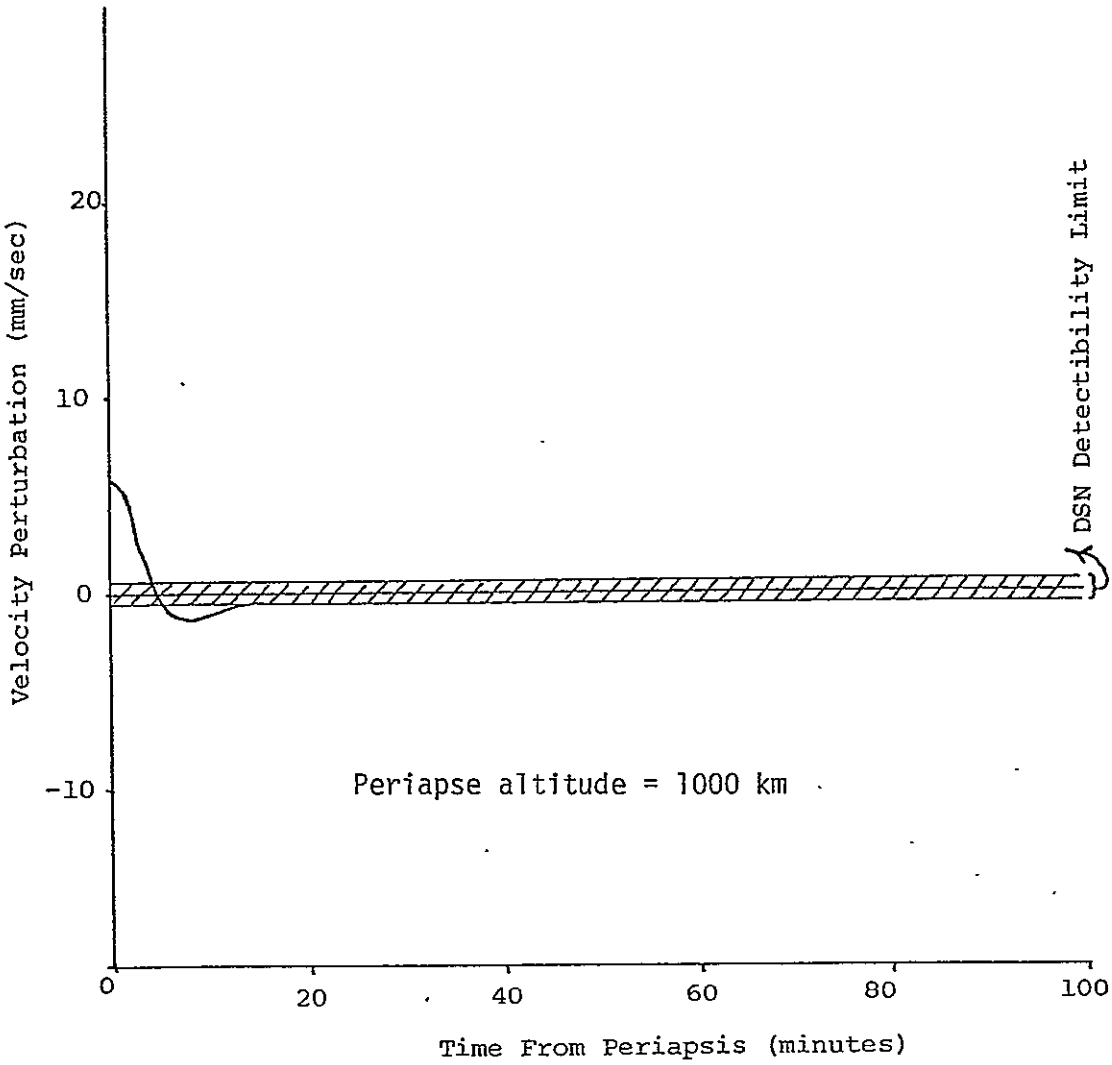

Figure 6.4 Velocity Perturbation During Polar Flyby Caused by J_2 Gravitational Coefficient of Io.

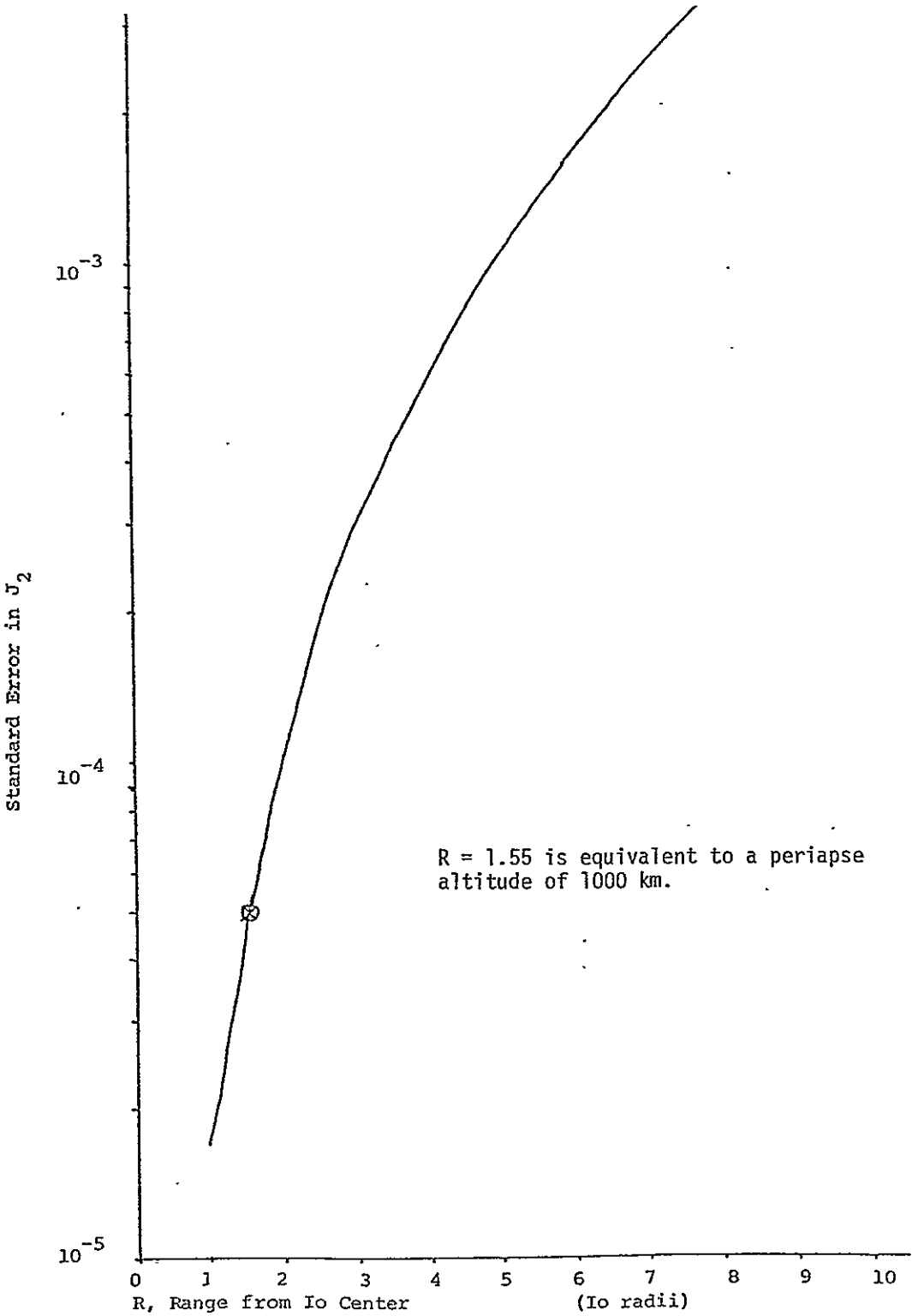

Figure 6.5 Error in Determination of J_2 ($\simeq 10^{-4}$) for Io from Flybys of Varying Periapse Altitude.

favorable if lower encounter speeds can be achieved. This discussion has neglected the effects of noise on the data which tends to reduce the measurement accuracies; nor does it include the effects of unmodeled harmonics. Also the multiple encounter mode could allow varying trajectory geometries which would enhance separation of gravitational harmonics of the same order. It appears that DSN tracking would provide good estimates of the second and perhaps third degree harmonics; however, measurement of fourth degree and certainly higher order harmonics does not appear feasible by this technique.

Summary - Gravimetry

DSN doppler tracking appears to be the best technique available to measure gravitational field harmonics from the relatively high altitudes, 500 to 1000 km, assumed for geology orbiter missions. Hundreds or orbits of data from the Mercury and Mars missions should allow the measurement of field harmonics up to about 15th and 12th degrees, respectively. These missions should return data similar to that gathered by Mariner 9, and data reduction should profit directly from experience gained from that earlier mission.

Sensing the gravity field harmonics of the Jovian satellites from a geology orbiter mission is subject to greater uncertainties. The limited number of satellite encounters (≤ 20), the relatively high altitude (500 to 1000 km), and the possibly unfavorable tracking geometry (inherent in a "quadrature tour") appear to limit sensitivity to harmonics of third degree or less. This circumstance may possibly be alleviated by improving satellite relative orbit determination accuracy and thereby allowing the encounter periapse to be lowered to 100 to 200 km. The incorporation of radar altimetry in the orbit determination calculations should be explored. Also, the impact of quadrature tour geometry on doppler tracking, necessary for navigation of any satellite tour mission, should receive further evaluation.

6.4 Geophysical Analysis of Combined Radar-Gravimetry Data Set

Taken together, data on topography and gravity field of a planet allow inferences to be drawn about the interior mass distribution and level and type of tectonic activity. The results in this regard from the Mariner 9 Mars mission represent the kind of rich return which might be expected from a Mercury or Mars geology orbiter. Our present knowledge of the topography of Mars, derived in part from Earth-based radar but mostly due to Mariner 9 investigations, has been compiled into a planet-wide topographic map (Figure 6.6, Ref. 6.10). Doppler tracking of Mariner 9 has similarly produced a nearly planet-wide gravity map (Figure 6.7, Ref. 6.10). With appropriate smoothing, the topographic data can be used to correct the free air gravity data measured by the spacecraft to a Bouguer gravity map. Such a map directly reflects the total column density of material beneath some chosen datum and so can reveal mass anomalies such as those due to the presence of low density roots beneath mountains and mascons within lunar basins. Study of Mars based on Mariner 9 data has revealed both isostatically compensated and uncompensated terrains. The ancient cratered terrain including the Hellas basin appears generally compensated, while the Tharsis plateau with its younger volcanic terrains is partially uncompensated (Figure 6.8, Ref. 6.11). There has apparently been considerable subsurface horizontal transport of material to beneath the Tharsis plateau. The Mars geology orbiter could provide data for a higher resolution planet-wide Bouguer gravity map which would allow further modeling of Martian tectonics. The Mercury orbiter would provide similar quality data for most of that planet and allow direct comparison of the tectonic and volcanic response to basic formation on the Moon, Mars, and Mercury.

The degree to which Bouguer gravity analysis can be carried out from flyby data of Jovian satellites is in doubt. The limited number of flybys will probably confine harmonic analysis of gravity fields to terms below third or fourth degree. Sensitivity to terms in a harmonic expansion of topography will be limited to about third degree or less depending on the distribution of the swaths of altimetry data. Both the Moon and

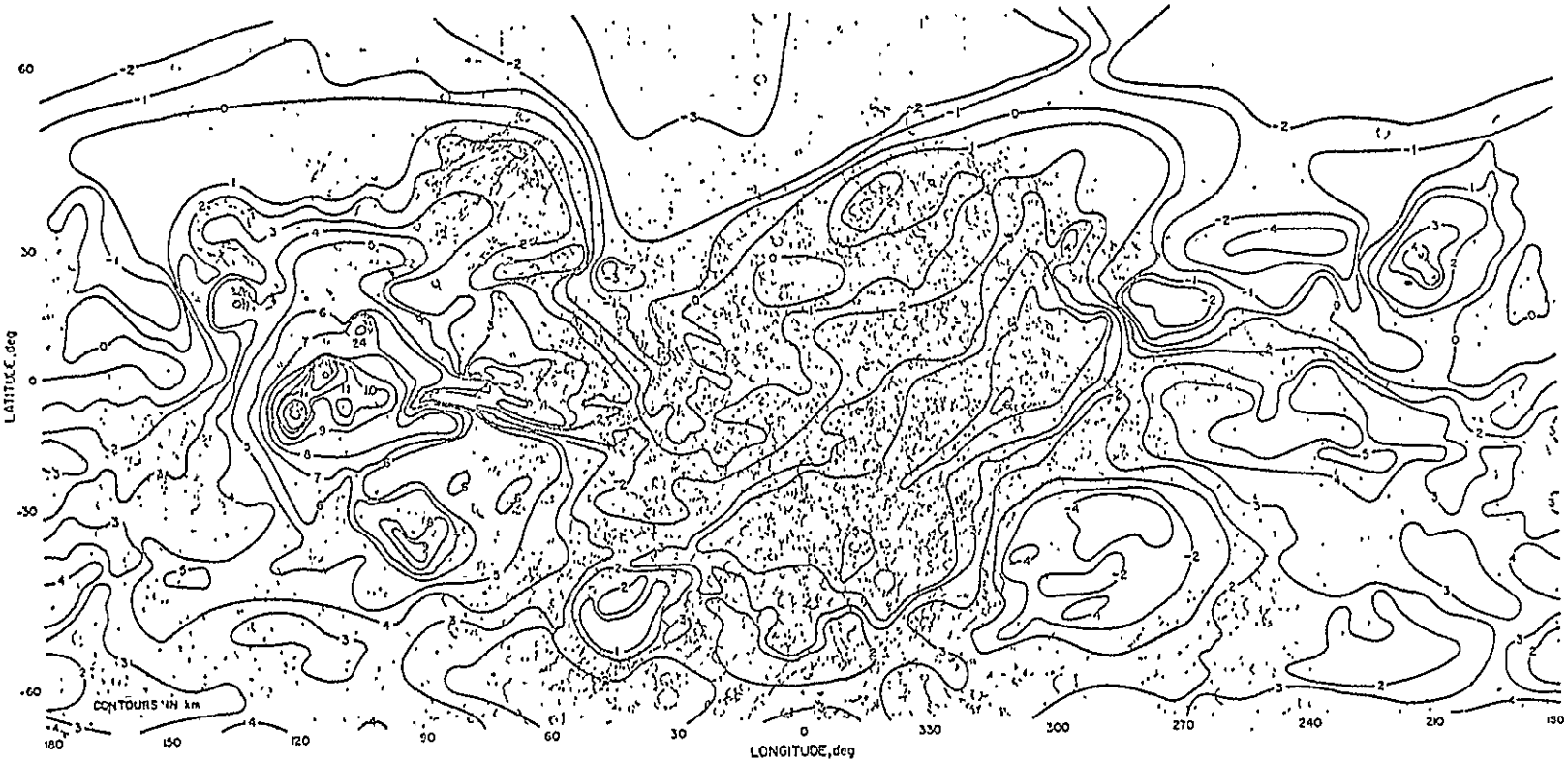

Figure 6.6 Topographic Heights Off the 6.1 mb Areoid of Mars (Ref. 6.10).

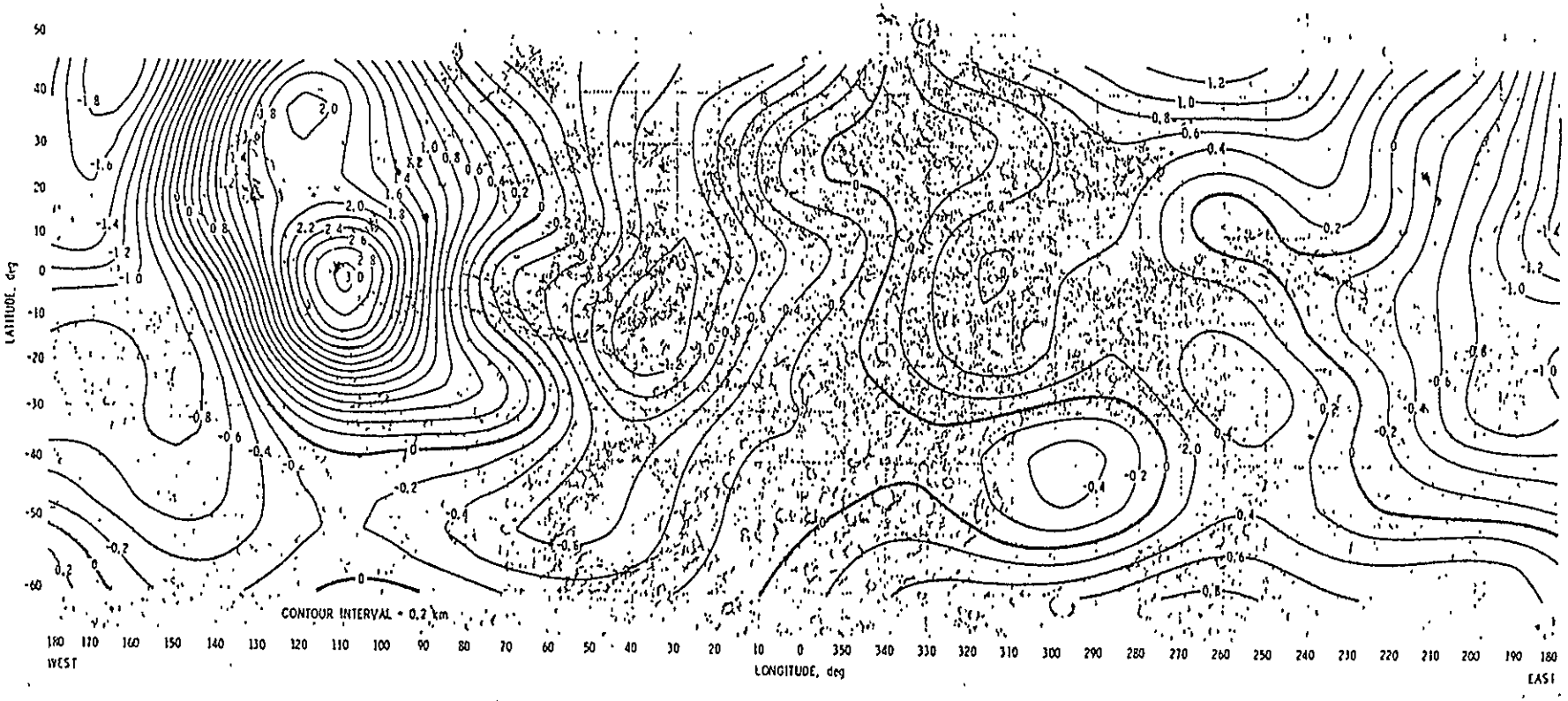

Figure 6.7 Model of Mar's Gravity Field by Height Contours of Equivalent Surface Mass of a Ninth-Degree and Ninth-Order Harmonic Expansion (Ref. 6.3).

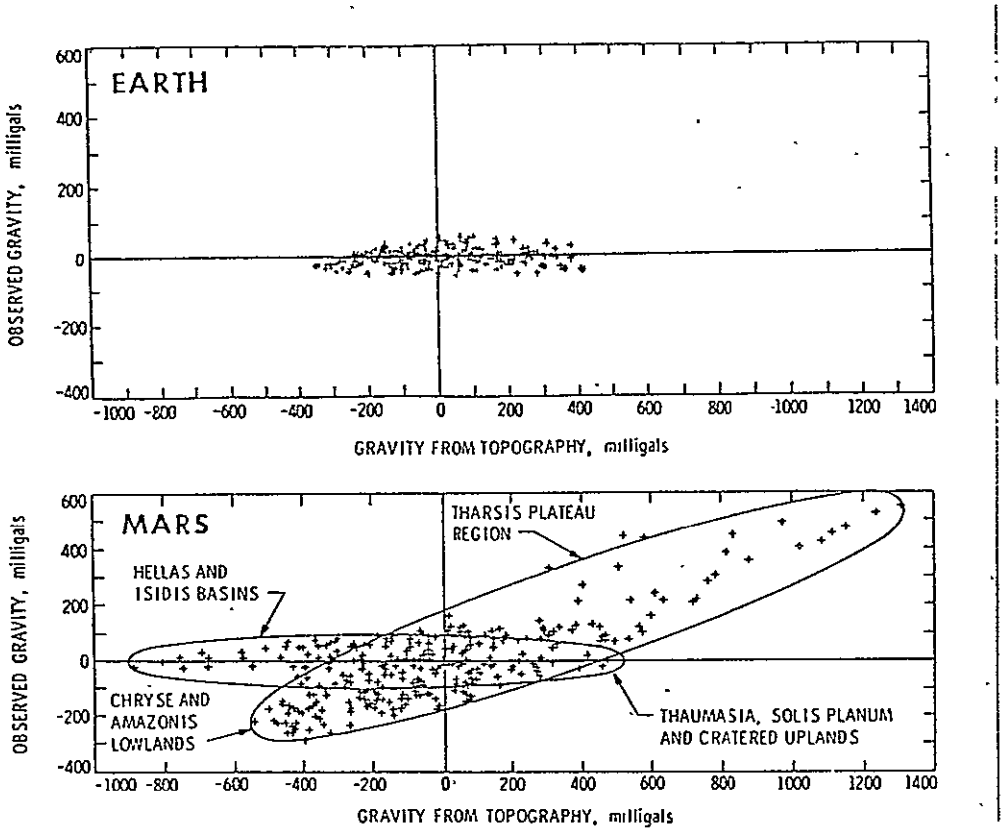

Figure 6.8 Scatter Diagram of Free Air Gravity vs. Gravitational Equivalent of Topography.

A population inclined at 45° would represent an entirely uncompensated mass excess or deficiency while a population close to the 0 observed gravity axis (as all Earth data) represents generally compensated topography.

Mars have been found to have hemispheric scale asymmetries in gravity and topography, so the ability to detect even the lowest degree terms in Bouguer Gravity could reveal the presence of a low density crust of variable thickness or broad continental scale mass excesses such as lie beneath the Imbrium Basin or Tharsis.

REFERENCES

6.1 Phillips, R. J. and W. L. Sjogren, "Geophysics Altimetry Gravity Experiment (GAGE)," (experiment proposal for the Lunar Polar Orbiter), Jet Propulsion Laboratory, California Institute of Technology; p. 128, 1975.

6.2 Russell, R. K. and J. Ellis, "Orbit Determination for a Jupiter Orbiter Tour of the Galilean Satellites," paper 74-847 of the AIAA Mechanics and Control of Flight Conference, August 1974.

6.3 Jordon, J. F. and J. Lorrell, "Mariner 9: An Instrument of Dynamical Science," Icarus, Vol. 25, pp. 146-165, 1975.

6.4 Forward, R. L., "Gravitational Field Measurements of Planetary Bodies with Gravity Gradient Instrumentation," Hughes Research Laboratories Report 448, August 1971.

6.5 Beckman, J. C. and E. C. Miner, "Jovian System Science Issues and Implications for a Mariner Jupiter Orbiter Mission," AIAA Paper No. 75-1141, September 1975.

6.6 Friedlander, A. L. and D. R. Davis, "Penetrator Mission Concepts for Mercury and the Galilean Satellites," SAI Report 1-120-339, February 1976.

6.7 Lorell, J., "Comparison of Spacecraft Gravity Measurement Techniques," JPL EM-391-720, January 1976.

6.8 Anderson, J. D., "Feasibility of Determining the Mass of an Asteroid from a Spacecraft Flyby," in Physical Studies of Minor Planets, NASA SP-267, 1971.

6.9 Dixon, J. F., private communication, 1976.

6.10 Christensen, E. G., 1975.

6.11 Phillips, R. J. and Saunders, A. S., 1975.